DEPOSITION AND CHARACTERIZATION OF TWO-DIMENSIONAL MATERIALS FOR AVIONIC AND OPTOELECTRONIC APPLICATIONS

Master Thesis

Elif Sevgi SİCİM

Eskişehir, 2023

DEPOSITION AND CHARACTERIZATION OF TWO-DIMENSIONAL MATERIALS FOR AVIONIC AND OPTOELECTRONIC APPLICATIONS

Elif Sevgi SİCİM

Master's Thesis

Department of Electrical Electronics Engineering

Programme in Electronic

Supervisor: Prof. Dr. Nihan KOSKU PERKGÖZ

Eskişehir

Eskişehir Technical University

Institute of Graduate Programs

May 2023

FINAL APPROVAL FOR THESIS

This thesis titled DEPOSITION AND CHARACTERIZATION OF TWO-DIMENSIONAL MATERIALS FOR AVIONIC AND OPTOELECTRONIC APPLICATIONS has been prepared and submitted by Elif Sevgi SİCİM in partial fulfillment of the requirements in "Eskişehir Technical University Directive on Graduate Education and Examination" for the Degree of Master's in Electrical Electronics Engineering Department has been examined and approved on 29/05/2023.

Committee Members		**Title, Name and Surname**	**Signature**
Member	:	Prof. Dr. Nihan KOSKU PERKGÖZ	
Member	:	Prof. Dr. Feridun AY	
Member	:	Prof. Dr. Gökhan ÇINAR	

Prof. Dr. Semra KURAMA
Director of the Institute of Graduate Programs

29/05/2023

SUPERVISOR APPROVAL

Master's student Elif Sevgi SİCİM, whom I supervise, has completed this thesis titled DEPOSITION AND CHARACTERIZATION OF TWO-DIMENSIONAL MATERIALS FOR AVIONIC AND OPTOELECTRONIC APPLICATIONS. According to my inspections, the work is scientifically and ethically appropriate for the student to the thesis defense exam.

Supervisor
Prof. Dr. Nihan KOSKU PERKGÖZ

ABSTRACT

DEPOSITION AND CHARACTERIZATION OF TWO-DIMENSIONAL MATERIALS FOR AVIONIC AND OPTOELECTRONIC APPLICATIONS

Elif Sevgi SİCİM

Department of Electrical Electronics Engineering

Programme in Electronic

Eskişehir Technical University, Institute of Graduate Programs, May 2023

Supervisor: Prof. Dr. Nihan KOSKU PERKGÖZ

The investigation of 2D materials has gained significant interest due to their unique properties that differentiate them from 3D forms. Research aims to better understand the characteristics of 2D materials and explore their potential applications in various fields. This thesis provides a detailed investigation on the deposition, transfer, characterization of graphene, MXene, and MoS_2. The aim is to contribute to future applications. The mentioned 2D materials were obtained using CVD, and their properties were characterized using Raman spectroscopy and AFM. The transfer processes have been carefully examined to ensure their efficient utilization in electronic devices. The primary focus of the thesis is on a new 2D material called MXene. Special attention has been given to the parameters involved in the deposition experiments of MXene, and the results of each experiment have been characterized to obtain insights into its structural properties. These studies reveal the possibility of achieving full coverage Mo_2C deposition and Mo_2C deposition without graphene. The thesis also presents a study on the conductivity measurements of carbon fibers using graphene as a nano-additive, aiming to develop graphene-based materials for avionic applications. The findings demonstrate an approximate doubling of conductivity when graphene is used in carbon fibers, highlighting its promising potential for applications. Furthermore, the thesis introduces a new 2D structure obtained through the direct growth of semiconducting MoS_2 on metallic Mo_2C via CVD, which is a novel achievement. This study emphasizes the synergistic effect created by stacking different materials, which is crucial for adjusting optical transitions in optoelectronic applications.

Keywords: MXene, MoS2, Graphene, Carbon fiber, Optoelectronic.

ÖZET

İKİ BOYUTLU MALZEMELERİN AVİYONİK VE OPTOELEKTRONİK UYGULAMALAR İÇİN BÜYÜTÜLMESİ VE KARAKTERİZASYONU

Elif Sevgi SİCİM

Elektrik Elektronik Mühendisliği Anabilim Dalı

Elektronik Bilim Dalı

Eskişehir Teknik Üniversitesi, Lisansüstü Eğitim Enstitüsü, Mayıs 2023

Danışman: Prof. Dr. Nihan KOSKU PERKGÖZ

2B malzemelerin araştırılması, 3B formlarından farklı olan benzersiz özellikleri nedeniyle büyük ilgi görmüştür. Araştırmalar, 2B malzemelerin özelliklerini daha iyi anlamayı ve potansiyellerini çeşitli uygulamalarda kullanmayı amaçlamaktadır. Bu tez, grafen, MXene ve MoS_2'nin biriktirilmesi, transferi ve karakterizasyonu hakkında ayrıntılı bir araştırma sunmaktadır. Böylece gelecekteki uygulamalara katkıda bulunulması amaçlanmaktadır. 2B malzemeler CVD kullanılarak elde edilmiş ve özellikleri Raman spektroskopisi ve AFM kullanılarak karakterize edilmiştir. Elektronik cihazlarda verimli kullanımlarını sağlamak için transfer süreçleri dikkatlice incelenmiştir. Bu tezin birincil odak noktası yeni bir 2B malzeme olan MXenedir.MXene'in biriktirme deneylerinde yer alan parametrelerine özel olarak odaklanılmış ve yapısının özelliklerineilişkin kavrayışlar elde etmek için her deneyin sonucu karakterize edilmiştir. . Bu çalışmalar, tam kaplama Mo_2C birikiminin ve grafensiz Mo_2C birikiminin mümkün olduğunu ortaya koymaktadır. Tez ayrıca, aviyonik uygulamalar için nano katkılı malzemelerin geliştirilmesi amacıyla, grafenin kullanıldığı karbon fiberlerin iletkenlik ölçümleri üzerine bir çalışma da sunmaktadır. Bulgular, karbon fiberde grafen kullanıldığında iletkenlikte yaklaşık iki kat artış olduğunu ortaya koymaktadır ve bu da uygulamalar için umut vaat eden potansiyelivurgulamaktadır. Dahası tezde, ilk kez, yarı iletken MoS_2'nin metalik Mo_2C üzerine CVD ile doğrudan büyütülmesi ile elde edilen yeni bir 2B yapı tanıtılmaktadır. Bu çalışma ile de, optoelektronik uygulamalarında optik geçişleri ayarlamak için çok önemli olan, farklı malzemelerin istiflenmesiyle yaratılan, sinerjik etki vurgulanmaktadır.

Anahtar Sözcükler: MXene, MoS2, Grafen, Karbon fiber, Optoelektronik.

ACKNOWLEDGEMENTS

I would like to express my sincere gratitude to my thesis supervisor, Nihan KOSKU PERKGÖZ, for her guidance, encouragement, and support throughout this research. Her feedback has been instrumental in shaping this thesis.

I am also grateful to Feridun AY for his assistance throughout my research. His persistent efforts and insistence on achieving the highest level of quality have been invaluable in producing a more robust and rigorous study. His expertise and feedback have played a crucial role in enhancing the quality of the studies.

I would like to extend my thanks to my research group MIDAS for their support throughout this journey. I appreciate their insights, feedback, and camaraderie.

I wish to express my gratitude to TUBITAK for granting me a scholarship for the project titled "İleri Malzeme Yüksek Teknoloji Platformları ile Elektronik ve Optik Bileşen Üretimi için Stratejik Ar-Ge Birliği" with project number "20AG025, 1004" under program number “20AG001”. The financial support has enabled me to focus on my research and produce the best possible results.

Finally, I would like to express my deepest gratitude to my mom and dad for their unwavering love, support, and encouragement throughout my academic journey. Their sacrifices and love have been my strength and inspiration. I am forever grateful for their unwavering support.

.

Elif Sevgi SİCİM

29/05/2023

STATEMENT OF COMPLIANCE WITH ETHICAL PRINCIPLES AND RULES

I hereby truthfully declare that this thesis is an original work prepared by me; that I have behaved in accordance with the scientific ethical principles and rules throughout the stages of preparation, data collection, analysis and presentation of my work; that I have cited the sources of all the data and information that could be obtained within the scope of this study, and included these sources in the references section; and that this study has been scanned for plagiarism with "scientific plagiarism detection program" used by Eskişehir Technical University, and that "it does not have any plagiarism" whatsoever. I also declare that, if a case contrary to my declaration is detected in my work at any time, I hereby express my consent to all the ethical and legal consequences that are involved.

Elif Sevgi SİCİM

CONTENTS

Page

LIST OF TABLES

Page

LIST OF FIGURES

Page

GLOSSARY OF SYMBOLS AND ABBREVIATIONS

2D	:	Two Dimensional
CVD	:	Chemical Vapor Deposition
Mo_2C	:	Molybdenum Carbide
MoS_2	:	Molybdenum Disulfide
CH_4	:	Methane
MoO_3	:	Molybdenum Trioxide
TMDCs	:	Transition Metal Dichalcogenides
SMU	:	Source Measure Unit
PMMA	:	Polymethyl Methacrylate
IPA	:	Isopropyl Alcohol

1. INTRODUCTION

Nanotechnology is poised to become the driving force behind the next growth cycle. Just as the industrial revolution transformed the world in the 19th century, and computers revolutionized society between 1969 and 2025, nanotechnology is expected to bring about rapid adoption and innovation in the years to come according to economist Norman Poire. Nanotechnology can be defined as the study and application of materials and systems at the nanometer scale, which ranges from approximately 100 nm to 1 nm. To put this into perspective, the thickness of a human hair is between 50^3 nm and 100^3 nm, the diameter of a virus is ~70 nm, and the diameter of an atom is 0.1 nm.

Nanoscience, on the other hand, is a multidisciplinary field that encompasses physics, chemistry, engineering, and biology, among other sciences, all working with materials and systems at the nanometer scale. It draws upon the expertise of various scientific disciplines to develop new materials and technologies that can function at the nanoscale. At the nanoscale, properties such as size and shape become critically important, and materials can exhibit different properties than their bulk counterparts. For example, bulk gold appears yellow in color, but nano-sized gold particles appear red due to the restricted movement of electrons in the smaller particles. In addition, the melting points of materials can be affected by their size at the nanoscale. At the nanoscale, surface atoms require less energy to move because they are in contact with fewer atoms of the substance. This means that the melting point of a material can be lower at the nanoscale than it is at the bulk scale.

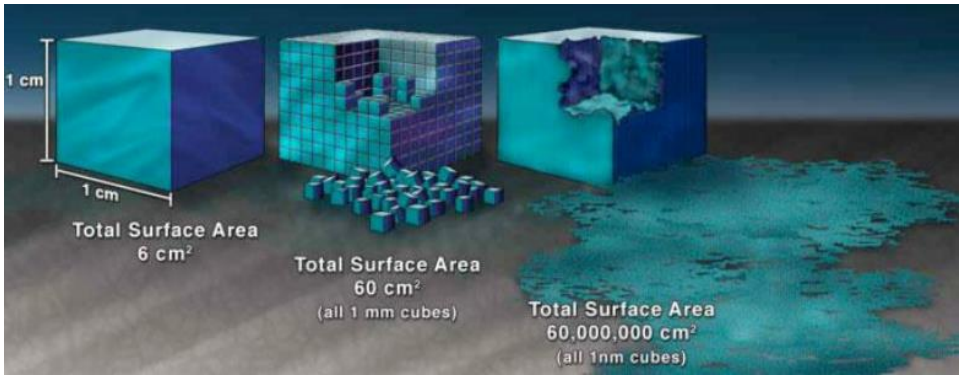

Figure 1.1. *Illustration demonstrating the effect of the increased surface area provided by nano-sized materials (Satyajeet Chaudhari, 2013)*

The study and application of nanoscience has opened up exciting new possibilities for innovation across a wide range of fields, including avionic applications. By incorporating nano-sized materials, enhancements in electrical, thermal conductivity, and mechanical strength of the materials used in aerospace systems can be achieved. Additionally, it offers lightweight design options, multifunctionality, and advanced integration capabilities for aircraft design. Moreover, these enhancements enable the development of multifunctional features such as electrically conductive composites for lightning strike protection, antistatic coatings to prevent electrostatic discharge, hydrophobic surfaces to repel water, and radar-absorbing applications for stealth capabilities. These functionalities are critical for ensuring the safety, efficiency, and operational effectiveness of avionic systems. Nanoscience also holds great importance in optoelectronic applications. The nano-sized materials exhibit size-dependent absorption, emission, and scattering of light, as well as the ability to manipulate the flow of photons, enabling advancements in areas such as high-speed optical communication, solar energy conversion, sensing, and imaging. Additionally, it enhances the performance of optoelectronic devices, such as increasing light absorption or emission efficiency. The nano-sized structures allow for the integration of multiple functions into a single device, leading to improved functionality and versatility.

Nanotechnology has emerged as a field with immense potential, with its impact on society expected to be significant in the coming decades. As early as 1959, Richard Feynman recognized the revolutionary possibilities of manipulating individual atoms and molecules in his talk "There's Plenty of Room at the Bottom." Since then, advancements in nanotechnology have led to groundbreaking developments in materials science, medicine, and other areas. In particular, the discovery of graphene, a 2D material, in 2004 has opened up a new era of research in nanotechnology. Graphene's remarkable properties, such as its strength, electrical conductivity, and transparency, have made it a promising candidate for applications in electronics, energy storage, and beyond. Furthermore, there is a growing interest in developing other 2D materials with semiconducting properties for use in switchable and optoelectronic devices, making them highly sought-after by both the scientific and industrial communities. Computational 2D Materials Database published a report in 2018 outlining the properties of more than 1500 2D materials with different crystal structures, which have the potential to create synthetic materials and devices utilizing 2D building blocks (Sten Haastrup, 2018). Among these

materials, MXenes discovered in 2011 are slightly ahead of other 2D materials due to their unique properties. The discovery of these novel 2D materials had a significant impact on materials science, providing benefits such as metallic conductivity, hydrophilicity, ease of processing, relatively high yields.

Overall, the research on 2D materials is progressing with each passing day, revealing the vast possibilities offered by the field of nanotechnology. However, to fully harness the power of nanotechnology, it is essential to have a deep understanding of the properties and behavior of materials at the nanoscale. By delving into the unique characteristics of 2D materials at this scale, we can unlock new possibilities for innovation and pave the way for a brighter future. Therefore, further research in this rapidly evolving field is crucial in order to fully realize the potential of nanotechnology and its impact on society.

1.1. Two Dimensional Materials

1.1.1. Graphene

Graphene is the first truly 2D crystalline material and represents an entire category of 2D materials. The structure of graphene consists of a hexagonal arrangement of sp^2-bonded carbon atoms, with each unit cell containing two carbon atoms. A stable graphene sheet was experimentally discovered in 2004 by Giem and Novoselov (K.S. Novoselov K. G., 2004). In graphene, the sp^2 hybrid orbitals of each carbon atom combine to form sigma (σ) bonds with three neighboring carbon atoms, resulting in a trigonal planar structure (A. Castro Neto, 2009). Graphene's mechanical properties are attributed to its σ bonds, which are formed by the sp^2 hybrid orbitals of adjacent carbon atoms in a trigonal planar structure. σ bonds provides exceptional structural rigidity. Additionally, the p orbitals of these carbon atoms are oriented perpendicular to the plane and can create a partially-filled π band through bonding, which results in the distinctive electronic properties of graphene. The presence of π electrons enables conduction.

Graphene has a unique band structure, with a linear dispersion of its π electrons, which makes it a zero-gap semiconductor. Metals, on the other hand, have a partially-filled valence band and empty conduction band, while semiconductors have a distinct energy gap between these two bands. Thus, graphene is considered as a semimetal. Due to the linear dispersion, its electrons and holes have zero effective mass and move at a constant speed known as the Fermi velocity. The charge carriers are regarded in analogy

to relativistic massless particles like phonons (K.S. Novoselov K. G., 2005), (M.S. Purewal, 2006).

Experimental evidence has demonstrated the exceptional properties of graphene, including high thermal conductivity at room temperature, remarkable transparency, and exceptional mechanical stability and flatness. High carrier mobility has been reported 15000 $cm^2/V.s$ for graphene on SiO_2 substrate, 27000 $cm^2/V.s$ for epitaxial graphene and 200000 $cm^2/V.s$ for suspended graphene (K.S. Novoselov K. G., 2005), (C. Berger, 2006), (K. Bolotin, 2008).

1.1.2. MXene

MXene is a young member of 2D transition metal carbides, nitrides, and carbonitrides. MXene has a layered arrangement in which the transition metal atoms are sandwiched between two layers of carbon and/or nitrogen atoms. The general formula for MXene is $M_{n+1}X_nT_x$, where M is a transition metal, X is carbon and/or nitrogen, T represents surface terminations, and n can vary depending on the specific MXene material (Naguib M., 2014) . The n value typically ranges from 1 to 3, but higher values are also possible. The exact structure and properties of MXene can vary depending on the specific transition metal and surface termination used. The surface of the MXene layers can be terminated with various functional groups. The T groups can affect the interlayer spacing and the orientation of adjacent layers, which in turn affect the properties and the exact structure of the MXene material (Kamysbayev V, 2020). Also, replacing carbon with nitrogen changes the arrangement of atoms, causing the electronic properties of MXene to change (Khazaei M, 2013). MXene with carbonitride and nitride compositions has the potential to display stronger metallic properties compared to that with carbide composition (A.N. Enyashin, 2013). In addition, the electronic properties of MXene can be tuned by replacing the outer metal layers with a different metal. Both experimental and theoretical studies have suggested that layered molybdenum-titanium MXenes exhibit properties similar to semiconductors (Babak Anasori, 2016). Also, it has been reported that a variety of cations such as Na+, K+, NH4+, Mg2+, and Al3+ can enhance the capacitance value beyond 300 F/cm^3 (farads per cubic centimeter) by inserting between the MXene layers (Maria R Lukatskaya, 2013).

The first MXene was discovered in 2011 by immersing Ti_3AlC_2 in hydrofluoric acid at room temperature. This process selectively etched away the aluminum layers,

resulting in a 2D form which has a chemical formula of Ti_3C_2 (M. Naguib, 2011). Figure 1.2 a) displays a scanning electron microscope (SEM) image of a Ti_3AlC_2 particle, which has a volume of approximately 1500 μm^3. The image shows how the basal planes of the particle spread out and separate from each other due to the HF treatment. The band structure of single-layer MXene with OH and F surface termination and no termination, revealed by DFT calculation is shown in Figure 1.2 b). The band structure of a single layer of Ti_3C_2 exhibits characteristics of a semimetal and has a finite density of states at the Fermi level. If terminated with OH and F groups, the band structure of Ti_3C_2 exhibits a semiconducting behavior, showing a distinct gap of 0.05 eV and 0.1 eV between the valence and conduction bands. Thus, it has been shown that it is possible to tune the electronic structure of the exfoliated MAX layers by changing the functional groups.

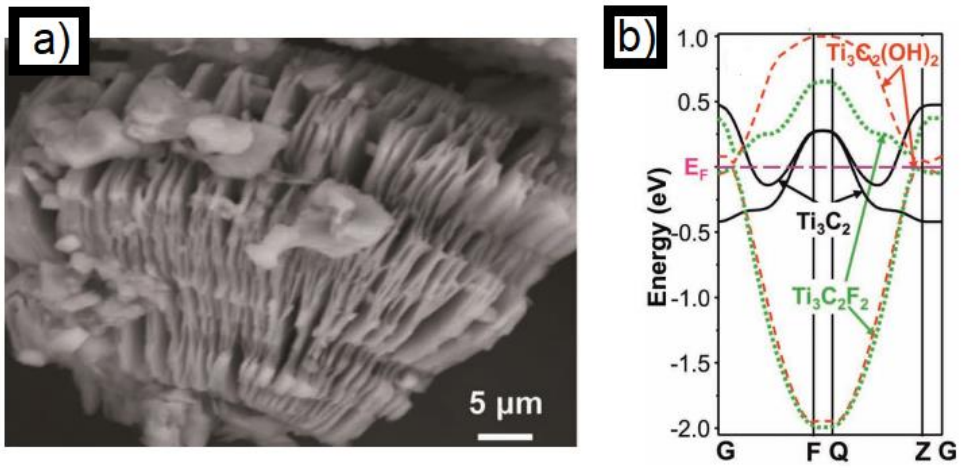

Figure 1.2. *a) SEM image of a sample after HF treatment b) The bant structure, showing a change from metal to semiconductor as a result of change in the surface chemistry (M. Naguib, 2011)*

The most commonly used method for MXene synthesis involves selectively etching the A layer from MAX compounds through a strong acid, like hydrofluoric acid or hydrochloric acid, which leaves behind a two-dimensional MXene layer. MAX compounds have a three-dimensional crystal structure consisting of multiple layers stacked on top of each other. Each layer in a MAX compound consists of a transition metal atom sandwiched between two layers of A and X atoms, and the layers are stacked on top of each other in a periodic manner.

Although the selectively etching is the most used method, it has some disadvantages. The etching conditions, such as acid concentration, time, and temperature,

need to be tuned accordingly to achieve the desired conversion to MXene depending on the each MAX structure. There are quite numerous tuning combinations required for successful MXene synthesis, as etching conditions have to be modified for each composition, for example due to differences in bond strengths between different M elements and Al layers (M. Khazaei, 2014). Moreover, some of these combinations can result in the formation of fluorides and oxides during the MXene synthesis process (Abdelmalak, 2014). Although, CVD synthesis of MXene is a relatively new and developing field, it offers several advantages over traditional etching methods. In recent years, Mo_2C, one of the MXene structure, has been synthesized by the CVD method without functional groups (Chuan Xu L. W.-L.-M., 2015), (Dechao Geng X. Z., 2016), (Dechao Geng X. Z., 2017). Consequently, this method has been reported to offer several advantages, including better control over MXene thickness and morphology, the ability to synthesize large-area films, and the potential for the scalable production.

MXene have a unique properties, including high electrical conductivity, excellent mechanical strength, good thermal stability, and high surface area. High strength mechanical behavior has been reported 330 MPa for single layer $Ti_3C_2T_x$ (A. Lipatov, 2018). High electrical conductivity has been reported 24000 S cm^{-1} for $Ti_3C_2T_x$ (A. S. Zeraati, 2021).

1.1.3. Molybdenum disulfide

MoS_2 is a compound that consists of one molybdenum atom and two sulfur atoms, with a layered structure. Each layer of MoS_2 is composed of a hexagonal lattice of molybdenum atoms sandwiched between two layers of sulfur atoms. MoS_2 has several crystalline phases, which are different arrangements of the atoms in its crystal lattice. One of them is the trigonal prismatic (2H') phase. In this phase, inversion symmetry is broken due to a shift in the positions of the sulfur atoms, which creates a non-zero piezoelectric response in the material (K.S. Novoselov A. M., 2016). The broken inversion symmetry leads to a splitting of the valence and conduction bands, which can result in an increased electron mobility and improved performance in electronic devices. The other phase is metastable crystalline phase known as 1T-MoS_2 was discovered by intercalating 2H-MoS_2 with alkali metals (Wypych & Schöllhorn, 1992). While, in the 2H phase of MoS_2 behaves as an indirect bandgap semiconductor, the 1T phase of MoS_2 behaves as a direct

bandgap semiconductor. The 1T phase of MoS_2 exhibits enhanced electrocatalytic activity (Manish Chhowalla, 2013).

1.2. Characterization Tools

1.2.1. Raman spectroscope

Raman spectroscopy is a spectroscopic technique capable of probing the chemical composition of matter via vibrational modes of molecules excited by inelastic scattering of photons (Olutayo I. Olubiyi, 2015). In an inelastic scattering, known as Raman scattering, part of the energy of the incident photon is lost or increased. According this condition, the incident photon is shifted towards lower or higher frequency for the total energy of the system to remain constant. When the part of the energy of the incident photon is transferred to the interacting matter; a called Stokes Raman scattering, a downshift of the scattered photon will be observed. When the interacting matter emits energy to the incident photon; a called anti-Stokes Raman scattering, an upshift of the scattered photon will be observed.

The Figure 1.3 shows the Raman Spectroscopy Setup. The setup consists of a light source, a microscope, a filter, a spectrograph and a computer. The working principle is as follow at the basic level: A matter is excited with a source of monochromatic light, usually from a laser is used. Scattered Rayleigh light is filtered out by either a notch filter or an edge filter. The filter delivers the laser to the matter and allows the scattered Raman light to pass through. Then, the spectrograph divides the light into separate wavelengths. The computer aims data handling and instrument controls.

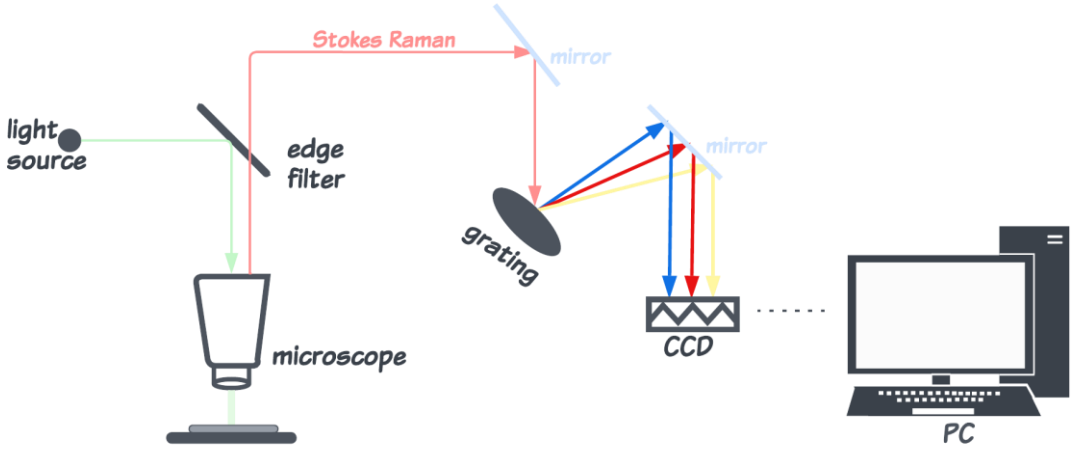

Figure 1.3. *Schematic of Raman Spectroscopy Setup*

The filter used in our laboratory is the edge filter. Edge filter allows the longer wavelength Raman light to pass through. In other words, only Stokes Raman shifts are observed. Edge filters offer better long term stability. They provide physical robustness at the cost of the loss of the anti-Stokes part of the spectrum.

Numerical aperture objective lens are an important measure of its ability to gather light and to resolve fine matter detail. The parts that can change depending on the lens are shown in the figure. The inferences from the lens are as follows: Collection solid angle is small for low numerical aperture lens. In case of higher numerical aperture lens, the collection solid angle became larger. However, laser spot size and sampling volume are inversely proportional with numerical aperture lens. High numerical aperture lens lead small laser spot size and small sampling volume. In other words, low numerical aperture lens lead large laser spot size and large sampling volume. Moreover, high numerical aperture lens cause high laser power density, which can potentially damage a sample, while it focuses the laser beam into very small spot. For transparent samples, low numerical aperture lenses work better because of the increased penetration of the laser into the sample. A larger sampling volume provides better sensitivity. However, for opaque samples, high numerical aperture lenses work better because there is almost no penetration of the laser into the sample. A small laser spot that under fills the entrance slit and a wide collection solid angle provide better sensitivity.

Scattered Raman light is collected and either dispersed by a spectrograph. The spectrograph consists of a monochromator, a grating and a CCD detector. The

monochromator uses a grating to disperse light and then focuses it at the exit. The diffraction grating separates light into its various wavelengths. The grooves are shaped to optimize the reflectivity of the grating for the working wavelength range. The groove density or groove spacing determines how well the wavelengths are separated. As the groove density increases, the definition of the lines improves, but less of the spectrum is captured simultaneously, as shown in Figure 1.4. Dispersion is a function of the focal length of the monochromator, the groove density of the grating and the working wavelength. Spectral resolution is a function of the dispersion, the width of entrance slit and the size of the detector pixel. In the final phase, the software is performing the calculation of the wavelength, wavenumber shift at each pixel on the CCD in order to produce a Raman spectrum. For any grating angle, it calculates the wavelength at each pixel and then converts that to Raman shift (Technologies, 2020).

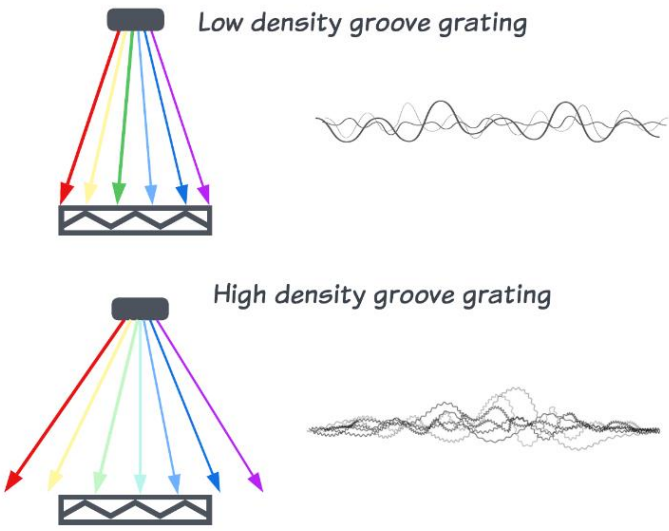

Figure 1.4. *Dispersion as a function of groove density*

1.2.2. Atomic force microscope

Atomic force microscopy is a surface analyze technique capable of creating a 3D profile of the surface on a nanoscale. AFM takes advantage of the atomic force between a tip and a sample surface. Unlike other high resolution microscopic techniques, which rely on interactions of electrons with a matter, AFM measures sample topography via a mechanical contact between the tip and the sample.

The Figure 1.5 shows the AFM Setup. The setup consist of a cantilever, a laser beam, and a photodiode. The working principle is as follow at the basic level: A cantilever scans over the sample surface with a very sharp tip. The cantilever is usually silicon or silicon nitride. As the tip approaches the surface the close range attractive force between the surface and the tip, cause the cantilever to deflect towards the surface. However as the cantilever is brought even closer to the surface, the tip makes contact with it, increasingly repulsive force takes over and causes the cantilever to deflect away from the surface. A laser beam is used to detect cantilever deflections by reflecting an incident beam off. Any deflection will cause slight changes in the direction of the reflected beam. A position sensitive photodiode is used to track these changes. According to the raised and lowered features on the sample surface, photodiode monitor the deflection by using a feedback loop to control the height of the tip. Thus maintaining constant laser position, the AFM will generate an accurate topographic map of the surface features.

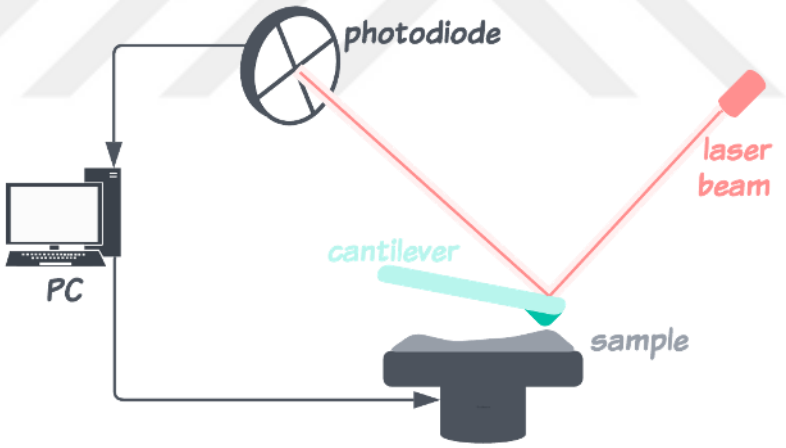

Figure 1.5. *Schematic of atomic force microscopy setup*

During contact with the sample, the probe experiences repulsive Van der Waals forces. This leads to the tip deflection described previously. As the tip moves far away from the surface attractive Van der Waals forces are dominant.

AFM can be operated in a number of modes, depending on the application. One of them is contact mode. In this mode, the tip is in continuous contact with the surface while the scanning, and it measures the mechanical contact force. The cantilever

deflection is the feedback parameter for this mode. The cantilever deflection is set by the user and is related to how hard the tip pushes against the surface. By maintaining a constant cantilever deflection, the force between the tip and the sample remains constant and an image of the surface is obtained. Its advantage is the fast scanning, but sometimes frictional and adhesive forces can cause damage to the sample.

Noncontact mode is one of other mode. In this mode, the tip of the cantilever doesn't contact the sample surface. The cantilever is oscillated at its resonant frequency or just above. The van der Waals forces, or any other long-range force above the surface decrease the resonance frequency of the cantilever. This decrease, combined with the feedback loop system, maintains a constant oscillation amplitude by adjusting the average tip-to-sample distance. Measuring this distance provides a topographic image. Its advantage; there is very low force on the sample, thus the tip lifetime will be long. Its disadvantage; generally gives lower resolution because of the contaminant layer on surface.

Dynamic mode is the most used mode in our laboratory. The cantilever oscillates at a high frequency or close to resonance. The tip lightly taps on the sample surface during the scanning. The frequency and amplitude of the driving signal are kept constant, to get a constant amplitude of the cantilever oscillation. As the tip gets closer to the sample, the interaction of Van der Waals forces and adhesive force cause the amplitude of the cantilever's oscillation to usually decrease. The amplitude of oscillation is the feedback parameter, and some dynamic modes have also different parameters for feedback such as frequency or phase. A topographic image is produced by the intermittent contacts of the tip with the sample surface. Its advantage being less destructive, also it allows high resolution. However, producing image is hard in liquids for this mode.

1.2.3. Probe station

A probe station is a tool that provides for electrical measurements, such as current-voltage (I-V) characteristics, capacitance-voltage (C-V) characteristics, and noise spectra, on individual semiconductor devices through the use of probes. They can also characterize semiconductor materials by measuring their electrical properties, such as resistivity and carrier concentration.

The probe station, in our laboratory, consists of a sample stage, four tungsten probes, a microscope, and a source-measure unit. The sample stage holds the

semiconductor device or material under test via a vacuum sample holder. The probes make contact with the sample. The microscope allows to align the probes precisely with the sample. The SMU apply electrical stimuli to the sample, such as voltage or current pulses. It can supply up to 200 V with a resolution of 100 fA. The electrical measurements are acquired through probes and then processed and analyzed using software. The software also provide various tools for data visualization and analysis.

2. EXPERIMENTAL

2.1. Chemical Vapor Deposition

CVD is a method to deposit 2D nanomaterials and thin films on various substrate. CVD involves chemical interactions between organometallic or halide chemicals and other gases to generate nonvolatile solid thin films on substrates (Sanjay J. Dhoble, 2023). The process typically takes place in a quartz tube, where the precursor gases are introduced and react to form the desired material. During CVD, the precursor gases are typically introduced through an inlet into the quartz tube. The gases then undergo various chemical reactions, including dissociation and deposition, on a heated substrate to form a 2D material/thin film. The substrate temperature and gas flow rates are carefully controlled to optimize the deposition process and ensure the desired properties of the resulting 2D material/thin film.

The objective of CVD is to produce large-area 2D materials with low-defect density and quality comparable to those obtained through exfoliation techniques. Precise control over layer numbers, domain size, and morphology is also a critical goal of the process. Numerous studies have showed the use of CVD method to produce high-quality 2D materials and their heterostructures with desirable properties, such as controllable thickness and scalable sizes (Pin-Chun Shen, 2018). These benefits make CVD a practical option for producing large-scale 2D atomic layers on a variety of substrates, which is crucial to fully realize the potential of 2D materials.

2.1.1. Graphene deposition

Graphene was obtained via the CVD method consisting of a 1-inch horizontal quartz tube. Copper was used as a substrate because it is a metal with low carbon solubility. Unlike metals with high carbon solubility, copper provides controlled deposition of carbon atoms on the surface without precipitation into the substrate, so it is one of the most preferred substrates for graphene (W. Fang, 2015), (X. Li, 2009), (K. S. Novoselov, 2012), (Kim, 2009). Firstly, copper was cleaned with acetone, IPA and deionized water via an ultrasonic bath, then dried via nitrogen gas. Clean copper was placed onto the quartz plate, which was then inserted into the tube, and positioned at the center of the heating zone. The vacuum control unit that is linked to the quartz tube was set to operate at its minimum possible pressure. Next, 100 sccm of hydrogen was introduced into the tube with a mass flow controller to etch the copper's native oxide layer

and to activate its surface. When the zone reached the desired growth temperature of 1035 °C, 40 sccm of methane was introduced into the tube for three minutes. In addition to being used as a carbon source, methane also makes it possible to obtain higher quality materials due to its decomposition at high temperatures (Pin-Chun Shen, 2018). The resulting carbon atoms deposited monolayer graphene on the copper due to three minutes. If it is desired to obtain multilayer graphene, this time is up to five minutes. After the time is over, the flow of methane gas was stopped with the mass flow controller and the zone was cooled down rapidly with the flow of hydrogen gas only. Finally, when the heating zone dropped below 100 °C, the flow of hydrogen gas was stopped, the pressure within the tube was balanced with atmospheric pressure, and the graphene/copper was removed from the tube.

2.1.1.1. Deposition parameters

Graphene deposition experiments had been carried out in a 3.15-inch quartz tube in our laboratory. Attempts were made to obtain graphene through a 1-inch quartz tube by changing the parameters. For example, the growth temperature was changed. Partial melting of copper was observed at higher temperatures, while lower temperatures could not provide enough conditions for carbon deposition. In another experiment, the gases used were decreased by same ratio being such as 20 sccm methane / 50 sccm hydrogen. This experiment also failed because the activation of the surface of the copper could not be achieved and/or the amount of carbon required for deposition could not be provided. The experiments in which successful graphene deposition was achieved are presented in Table 2.1.

Table 2.1. *Graphene experiments*

Experiment Number	CH_4 Flow Rate (sccm)	Temperature (°C)	Growth Time (min.)	Hydrogen Flow Rate (sccm)	Quartz Tube (inch)
1	40	1035	3	100	3.15
2	40	1035	30	125	1
3	40	1035	20	125	1
4	40	1035	3	100	1

The first row in the table shows the parameters for monolayer graphene obtained in the 3.15-inch tube. Experiments 2, 3, and 4 show the experiments that were carried out in a 1-inch tube. The second experiment resulted in multilayer graphene, whereas in the third experiment, where the methane flow time was reduced to 20 minutes, resulted in both multilayer, bilayer, and monolayer graphene parts over a copper irregularly. Eventually, thanks to the fourth experiment, the deposition of monolayer graphene in a 1-inch tube was successfully achieved.

2.1.1.2. Graphene characterization

Optical microscopy images of graphene on copper are presented in the Figure 2.1. Graphene is nearly transparent to visible light and does not reflect or scatter enough light to be visible under an optical microscope. This is the reason why a clear hexagonal shape of the graphene layer cannot be observed. The little crackles or markings that can be seen in the images might be caused by defects or impurities in the graphene layer.

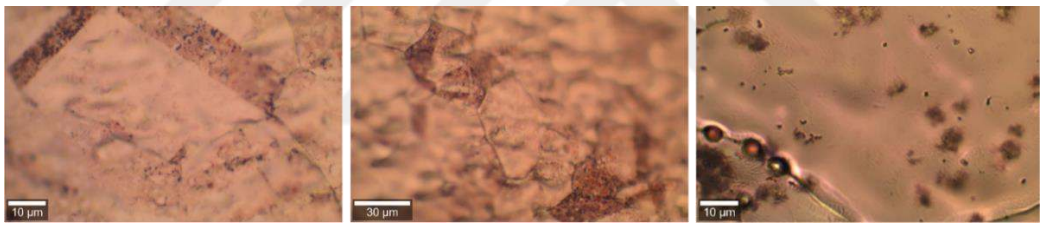

Figure 2.1. *Optical microscopy images of graphene*

Although it cannot be seen with an optical microscope, it is possible to identify graphene obtained with a Raman spectroscope. Raman spectrum from monolayer graphene is shown in Figure 2.2. The figure shows the two prominent bands required to characterize the obtained graphene; the G band and the 2D band. G band represents the planar configuration of sp^2 bonded carbons and is associated with the E_{2g} phonon mode (Lancelot, 2011). G band commonly present at 1582 cm^{-1}. It is independent of the excitation laser frequency. 2D band is result of a two phonon lattice vibrational process. The changes in band shape have to do with changes to the active components of the vibration, whereby a monolayer graphene possesses only one component, while multilayer graphene has several component. 2D band commonly present at 2685 cm^{-1}. As the layer thickness increases, the band position shifts to higher wavenumber. The most important is that, the ratio of the intensities of these bands gives information about the

number of graphene layer. According to the provided Raman spectrum, the I_{2D}/I_G ratio is ~3, which indicates that the obtained graphene is monolayer according to the literature (Zhiqiang Tu, 2014), (Yu Q, 2011), (Mukesh Singh, 2014), (L. Huang, 2012).

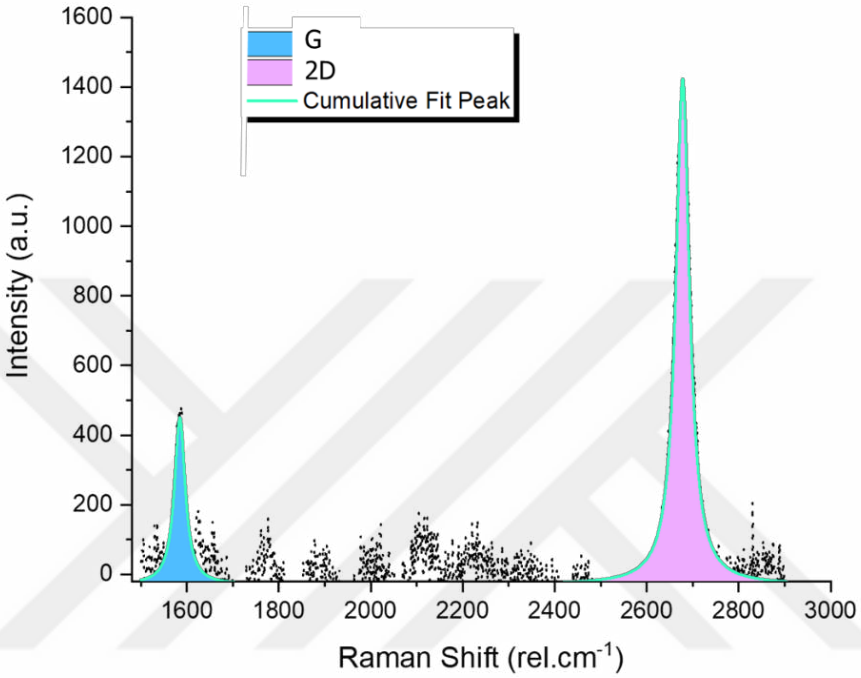

Figure 2.2. *Raman spectrum for monolayer graphene on copper*

AFM data of multilayer graphene are presented in the Figure 2.3. However, the height of monolayer graphene varying between 0.4 nm and 1.7 nm reported in the literature could not be measured (W. Lisheshar Ibrahim, 2022). This may be because there are often air bubbles or water molecules that get trapped between the graphene and the substrate during transfer, making it difficult to measure the true thickness of the graphene layer.

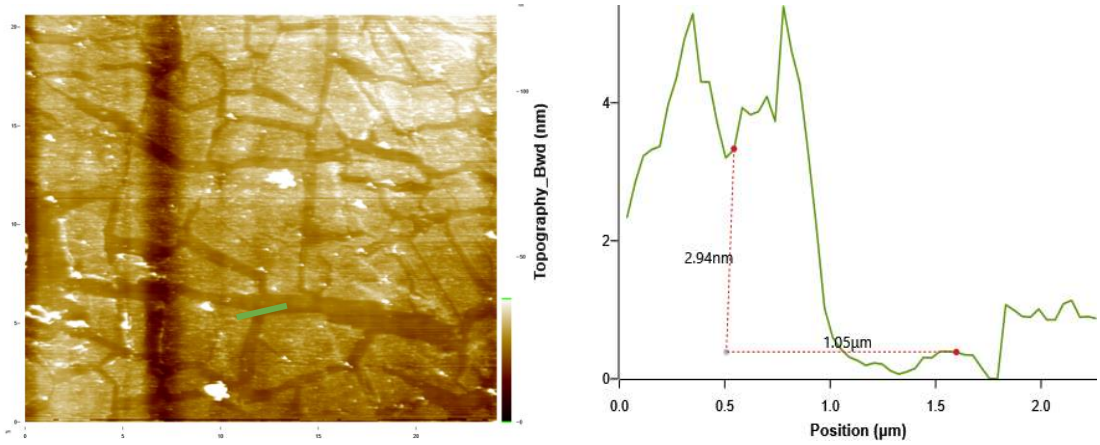

Figure 2.3. *Topography of the graphene on SiO_2/Si and the height profile along the green line in topography*

2.1.2. MXene Deposition

Mo_2C was obtained via the CVD method consisting of a 1-inch horizontal quartz tube. Molybdenum foil, as a transition metal source, and copper foil, as a catalyst for capturing carbon atoms were used in this deposition process. Firstly, the foils were cut with the purpose of making the molybdenum foil is smaller than the copper foil in size. They were cleaned with acetone, IPA and deionized water via an ultrasonic bath, then dried via nitrogen gas. Finally, molybdenum foil was placed onto the copper foil and the corners of the copper foil were folded over the molybdenum foil as shown in Figure 2.4.

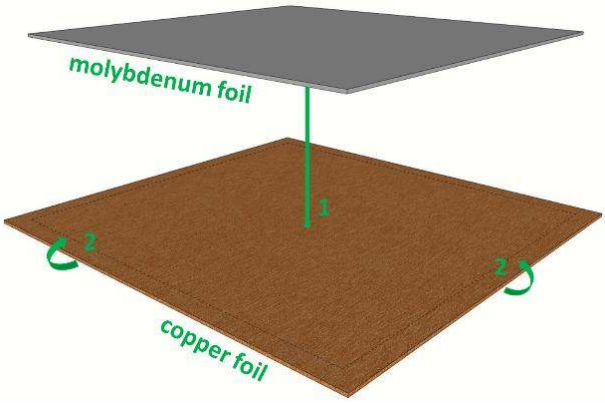

Figure 2.4. *Preparation of the foils*

The prepared foils were inverted and placed onto a quartz plate. Then, the quartz plate was inserted into the tube as shown in Figure 2.5 and positioned to the first part of the heating zone. After the temperature and pressure adjustment as required, hydrogen gas was introduced into the tube with a mass flow controller. Hydrogen gas was used as

an activator for copper surface throughout the process. Methane gas was used as a carbon source when the tube reaches the adjusted temperature. Both hydrogen and methane gases are necessary to initiate the reaction of carbide formation. At the end of growth time, the flow of the methane gas was stopped with the mass flow controller and the quartz tube was cooled down rapidly to room temperature with the flow of hydrogen gas only. Finally, the flow of hydrogen gas was stopped, and the Mo_2C on the molybdenum/copper alloy was removed from the tube. The process was performed under ambient pressure.

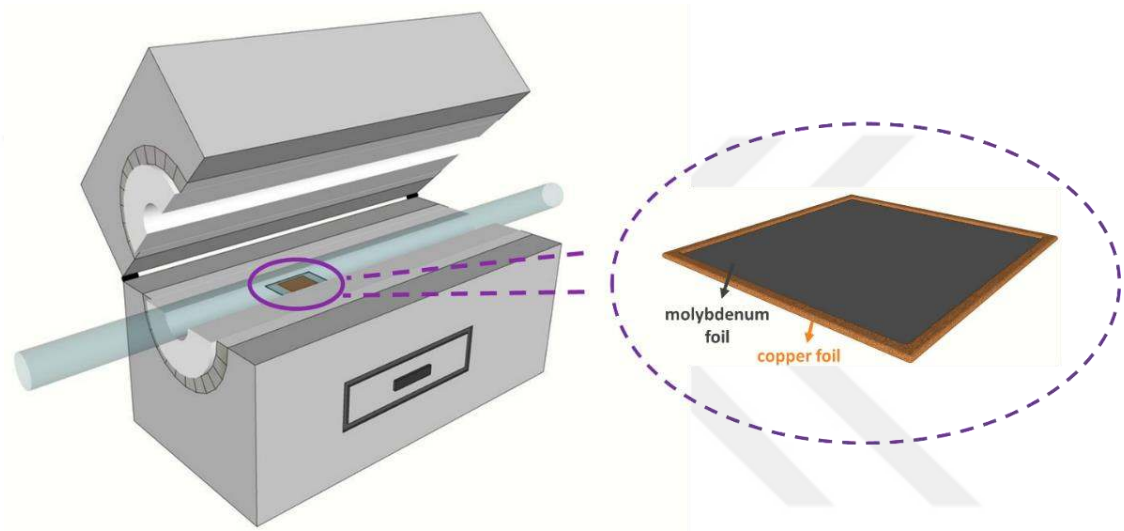

Figure 2.5. *Schematic of CVD system for Mo_2C. Inset: The bottom view of foils which are placed in the quartz tube*

2.1.2.1. Deposition parameters; copper thickness, temperature, methane flow rate, growth time

The Mo_2C deposition process begins with the melting of copper on molybdenum, and a molybdenum/copper alloy is formed on the surface. When the copper completely alloys with the molybdenum foil, the remaining molybdenum atoms rise to the surface. The process ends by capturing the methane supplied to the system and reacting on the surface to form Mo_2C. For this process, the amount of carrier gas, pressure and molybdenum foil used throughout the experiments were kept constant by looking at the previous studies in our laboratory (Kılıç, 2022). However, in subsequent experiments, the aim is to achieve the largest possible coating area of Mo_2C on the molybdenum/copper alloy by changing the copper thickness, temperature, methane flow rate, and growth time. Table 2.2 presents the thickness-dependent experiments carried out to select the appropriate copper foil.

Table 2.2. *Mo_2C process parameters for different thicknesses of copper foil*

CH_4 Flow Rate (sccm)	Ambient Pressure (torr)	Temperature (°C)	Growth Time (min.)	Copper Foil (µm)
10	776	1100	10	120.3
10	776	1100	10	60
10	776	1100	10	35

Figure 2.6 a) and b) are the results of experiments using copper with a thickness of 120.3 µm and 60 µm, respectively. Mo_2C formation is very rare, as the diffusion of molybdenum atoms becomes difficult when 120.3 µm and 60 µm foils are used. The region displayed in a) and b) the region where the most intense deposition occurs. In c), it can be clearly seen that when thin copper is used, Mo_2C is increasingly covering the surface. In other words, when thicker copper is used, the barrier faced by the molybdenum atoms becomes higher, making it more difficult for the molybdenum atoms to diffuse and form Mo_2C. Therefore, the experiments were continued with copper with a thickness of 35 µm.

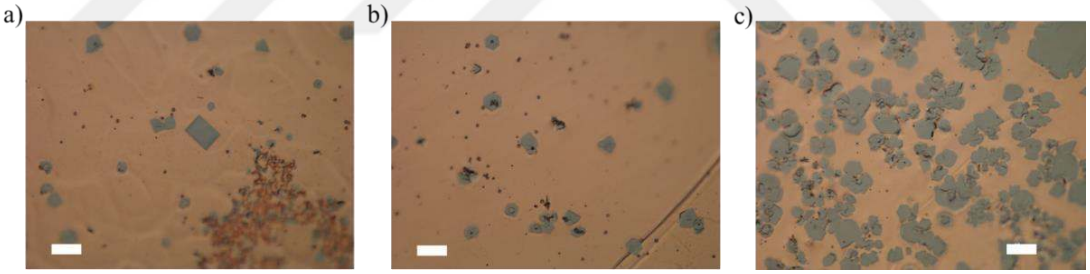

Figure 2.6. *Optical microscopy images of experiments with different thicknesses of copper foil; a) 120.3 µm b) 60 µm c) 35 µm. Scale bars: 10 µm*

The experiments carried out at different temperatures are shown in the Table 2.3. The experiments were started at 1035 °C and ended at 1200 °C, at which point the linear increase in coverage began to declinedue to rising temperature. In the experiment carried out at 1035 °C, the reaction did not occur because there was no change in the solid state of copper. Only the surface of the copper foil was activated by hydrogen, while the molybdenum foil remained the same.

Table 2.3. *Mo_2C process parameters for experiments carried out at different temperatures*

CH_4 Flow Rate (sccm)	Ambient Pressure (torr)	Temperature (°C)	Growth Time (min.)
10	750	1035	10
10	750	1060	10
10	754	1085	10
10	754	1090	10
10	752	1095	10
10	752	1100	10
10	750	1120	10
10	750	1150	10
10	750	1175	10
10	752	1200	10

As a result of the optic microscope examinations after the experiments, it was observed that CVD could not provide a consistent deposition across all areas on a sample. Therefore, in order to improve the reliability of the experiments, the sample removed from the tube was examined by capturing sequential optical microscopy images as illustrated in the Figure 2.7. The images were captured across the sample along a transverse line that was parallel to the width of the tube.

Figure 2.7. *Capturing sequential optical microscopy images from a sample. Inset: The sample: Mo_2C on molybdenum/copper foil. The blue squares represent each optical microscopy image that was captured*

The results of some experiments where the temperature is increased from 1060 °C to 1200 °C are shown in Figure 2.8 to Figure 2.12. Since the temperature of the experiment carried out at 1060 °C was below than copper's melting point of 1085 °C, copper could not completely become liquid state. As a result, the density of molybdenum atoms that could reach the surface was very low, leading to the formation of flakes with an average diameter of ~5 µm. However, in subsequent experiments, it was observed that an increase in temperature resulted in an increase in coverage.

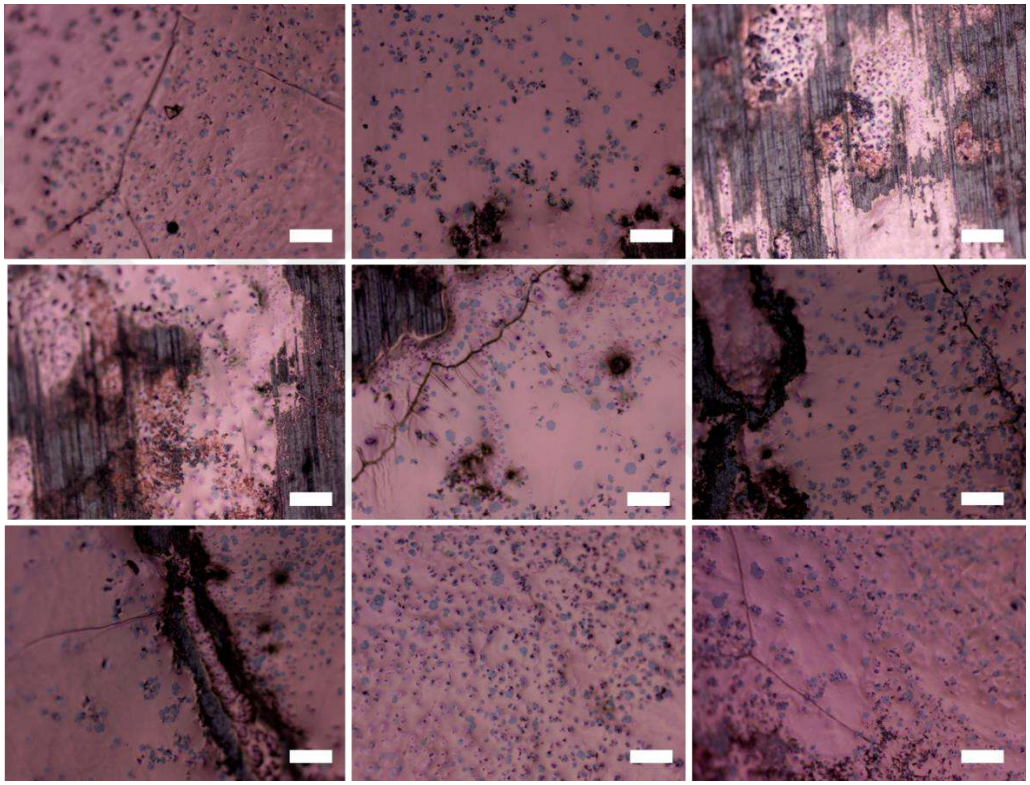

Figure 2.8. *Optical microscopy images of the experiment at 1060 °C. Scale bars: 50 µm*

While the surface coverage results were not significantly different between the experiments carried out at 1120 °C and 1150 °C, as displayed in Figure 2.9 and Figure 2.10, the flakes formed at 1150 °C were relatively larger, and their coverage was more uniform. The average diameter of these flakes was ~25 µm.

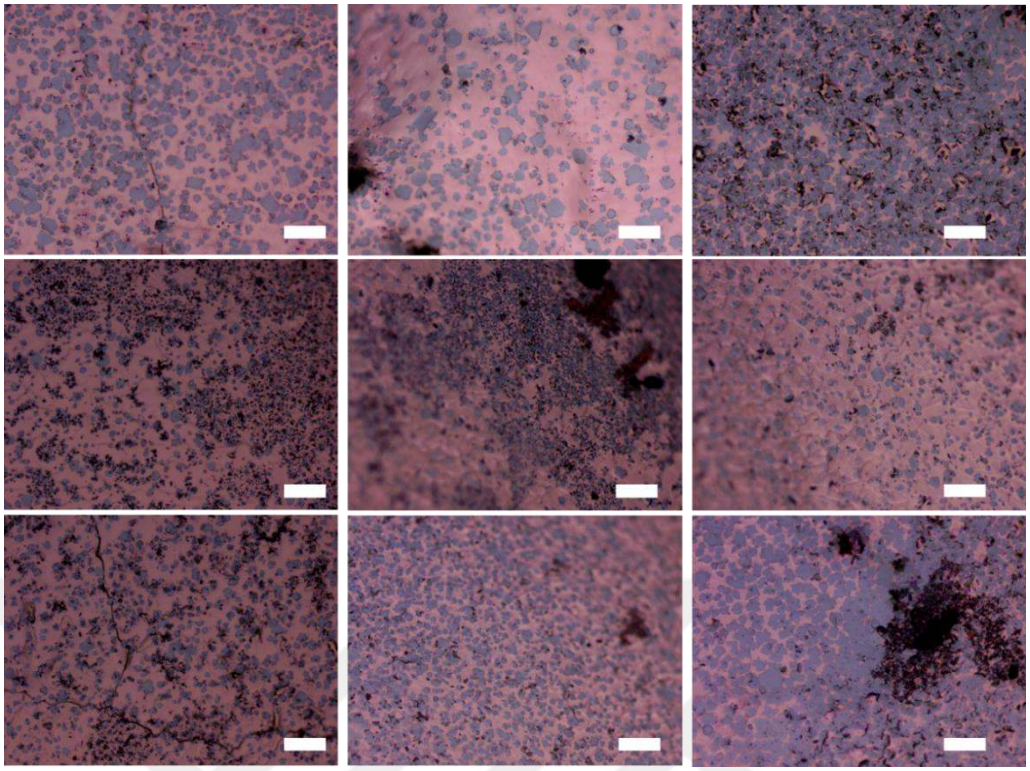

Figure 2.9. *Optical microscopy images of the experiment at 1120 °C. Scale bars: 50 µm*

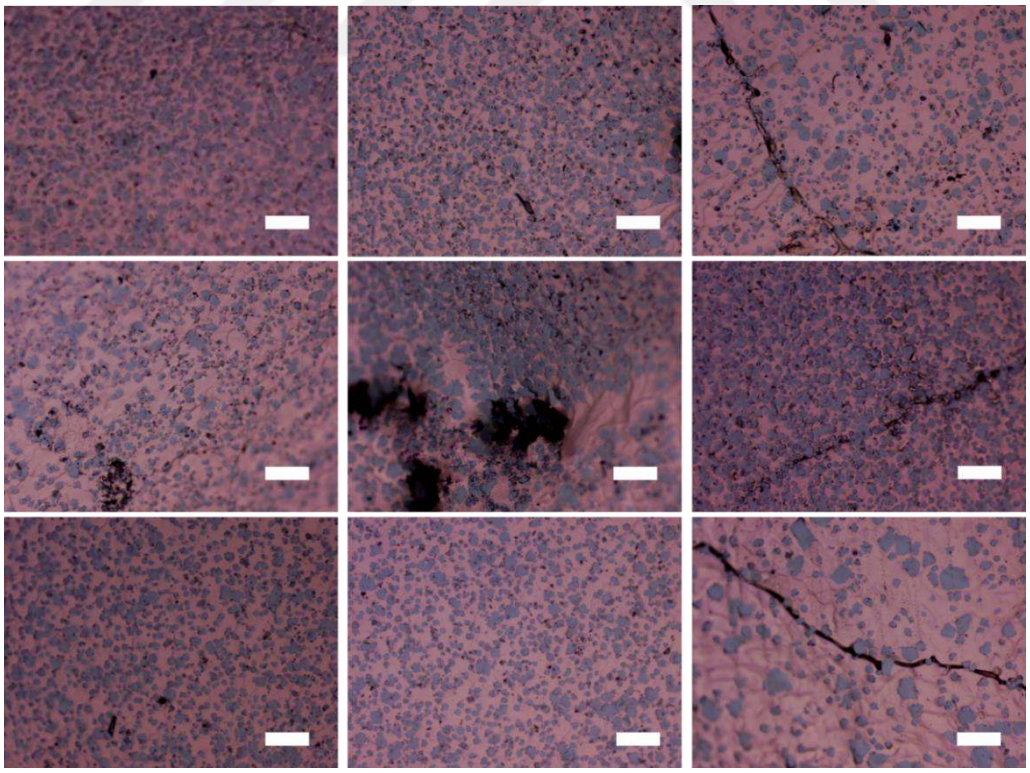

Figure 2.10. *Optical microscopy images of the experiment at 1150 °C. Scale bars: 50 µm*

Maximum coverage was achieved in the experiment at 1175 °C. This density was obtain by the accumulation of Mo_2C flakes without change in flake size.

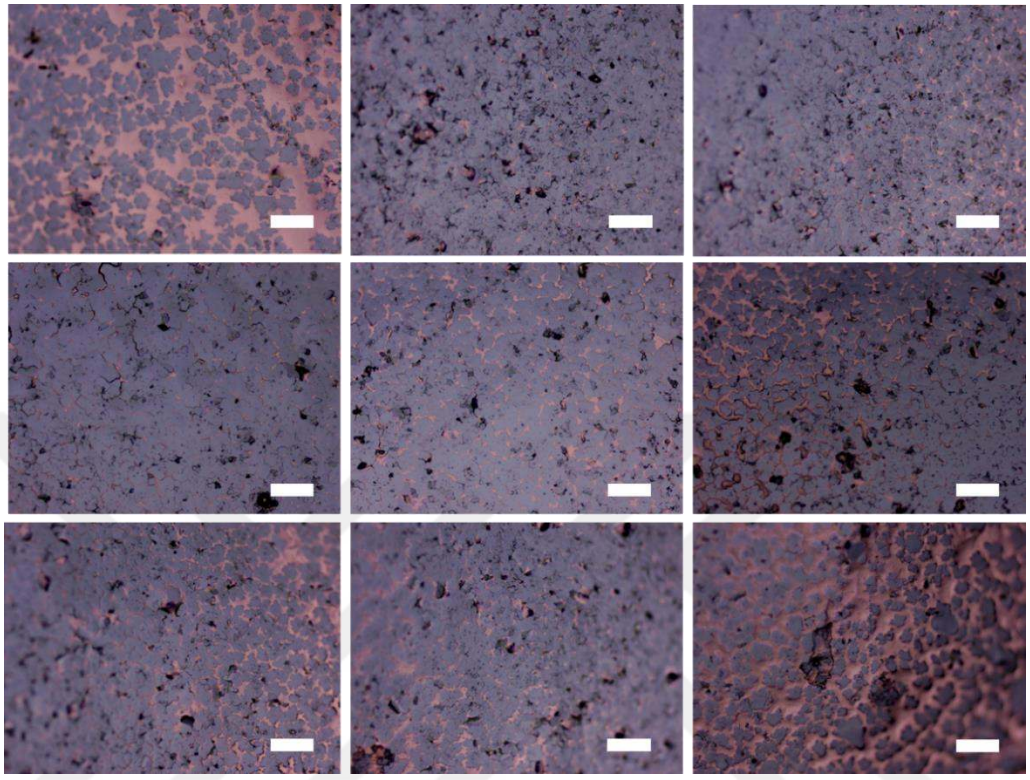

Figure 2.11. *Optical microscopy images of the experiment at 1175 °C. Scale bars: 50 µm*

The linear relationship between coverage and temperature was broken at 1200 °C, which is the maximum experiment temperature. Although dense sites were encountered in places, a significant decrease in coverage was observed overall. In addition, although the size of the flakes formed is large, some changes were observed in their structure, such as their formation in fractal shapes.

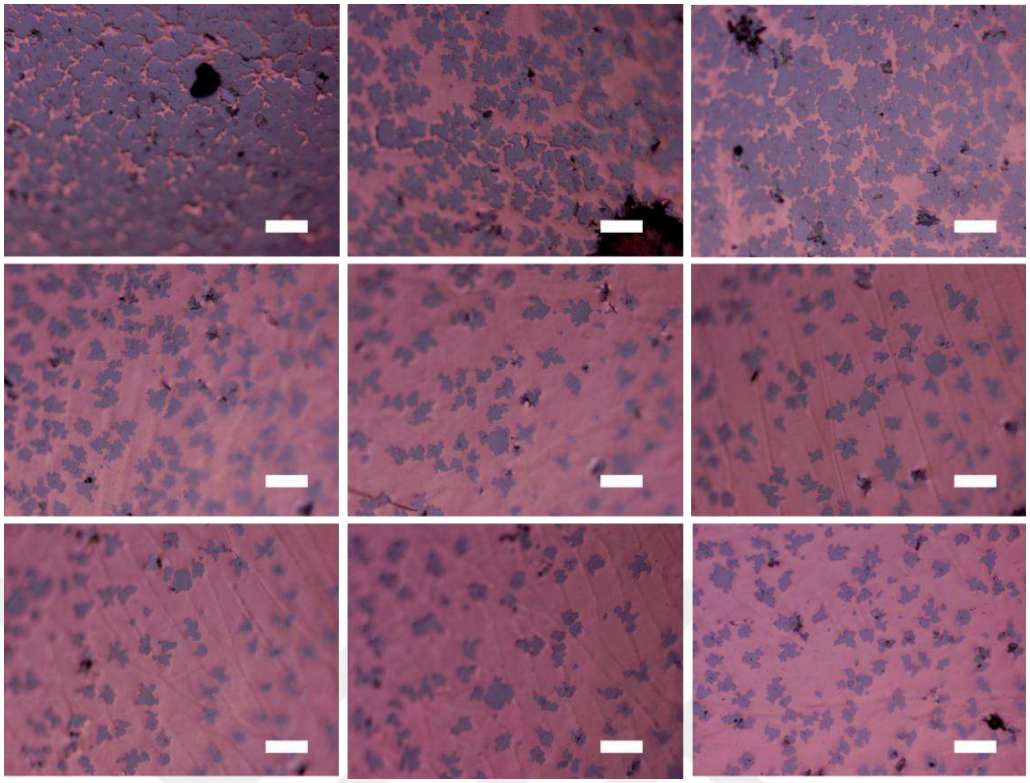

Figure 2.12. *Optical microscopy images of the experiment at 1200 °C. Scale bars: 50 µm*

Experiments using different methane flow rates from 0.7 sccm to 8 sccm are shown in Table 2.4. The results are displayed from Figure 2.13 to Figure 2.17 with sequential optical microscopy images, as explained before. In general, it was observed that the formation of Mo_2C increased as the molybdenum atoms were able to capture more carbon atoms with the increase of methane flow rate during growth time.

Table 2.4. *Mo_2C process parameters for experiments carried out with different methane flow*

CH_4 Flow Rate (sccm)	**Ambient Pressure (torr)**	**Temperature (°C)**	**Growth Time (min.)**
0.7	763	1150	10
2	748	1150	10
4	750	1150	10
6	750	1150	10
8	753	1150	10

Looking at Figure 2.13, it was observed that Mo_2C formation was very rare, with only a few having a width of ~1 µm and a length of ~30 µm. As the methane flow increased, the coverage is also increased because more carbon atoms react with

molybdenum atoms on the surface. In addition, despite the increase in methane flow rate, there was no significant change in flake size and in the structure, especially beyond 4 sccm.

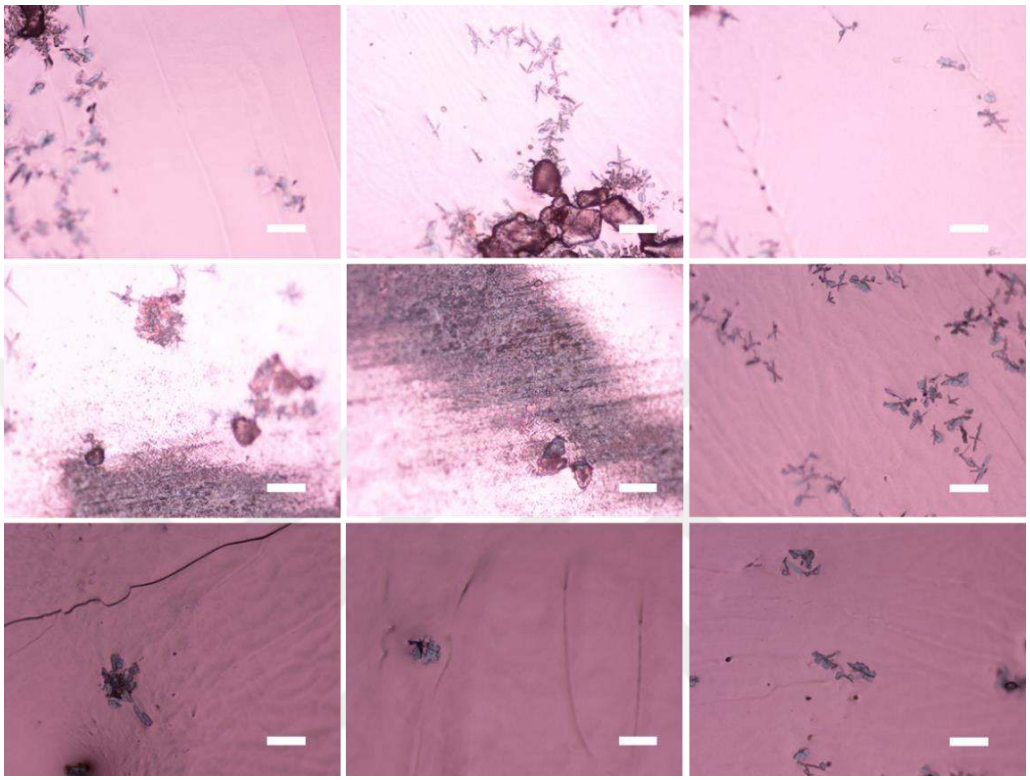

Figure 2.13. *Optical microscopy images of the experiment with 0.7 sccm methane flow. Scale bars: 50 µm*

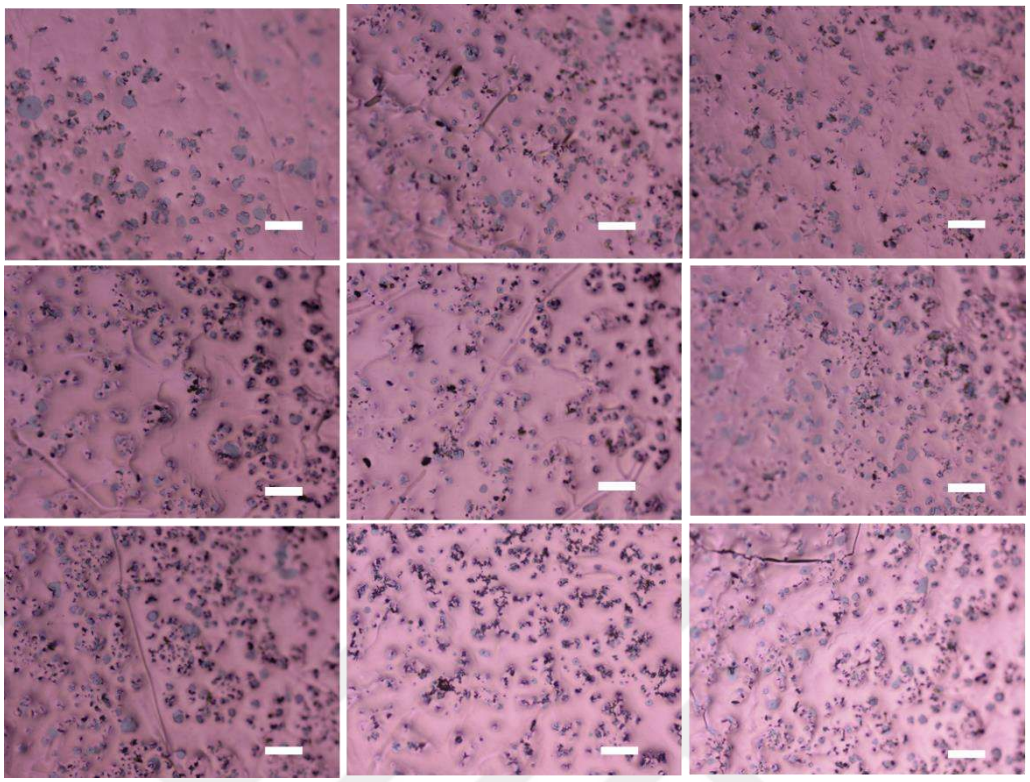

Figure 2.14. *Optical microscopy images of the experiment with 2 sccm methane flow. Scale bars: 50 µm*

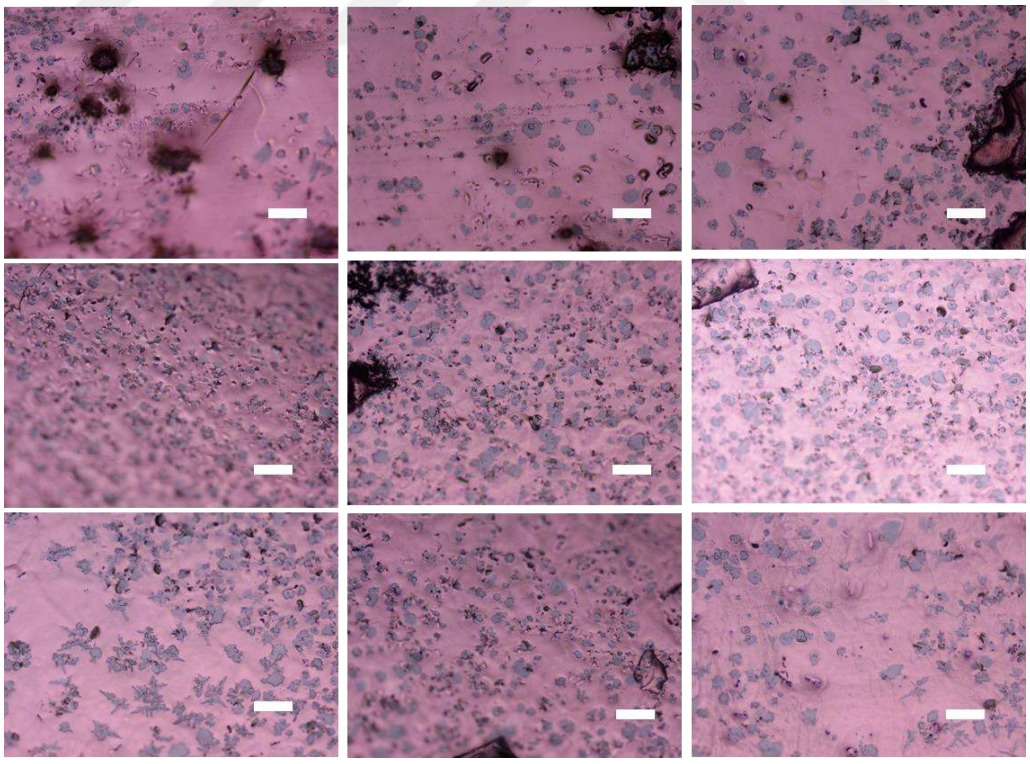

Figure 2.15. *Optical microscopy images of the experiment with 4 sccm methane flow. Scale bars: 50 µm*

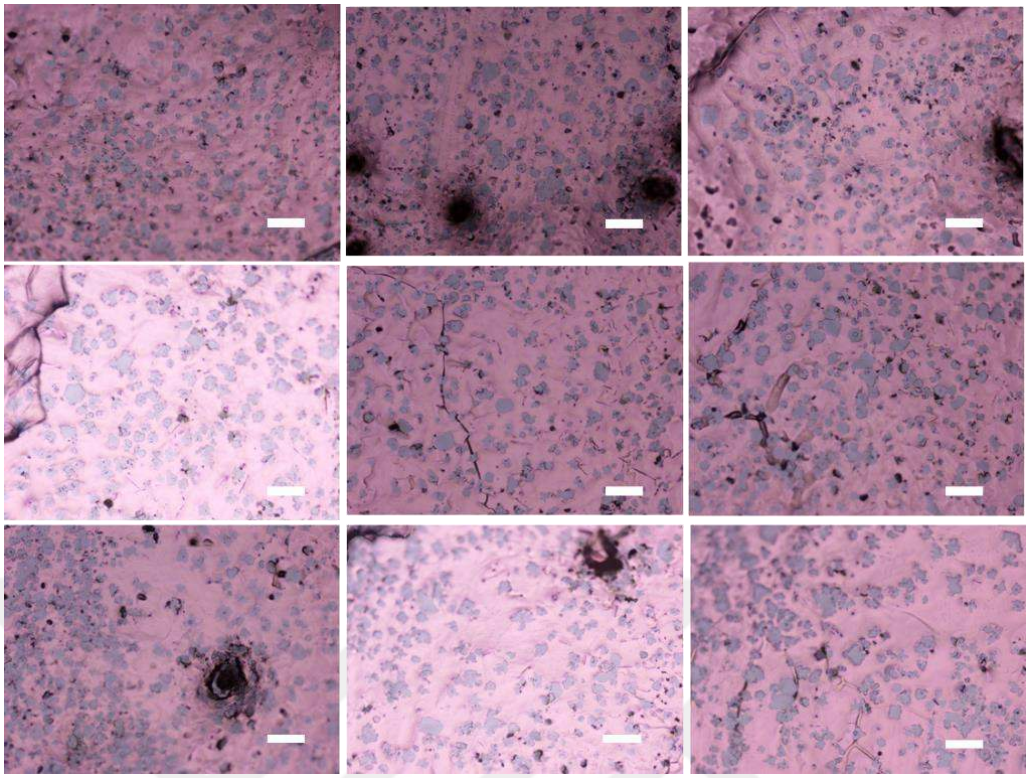

Figure 2.16. *Optical microscopy images of the experiment with 6 sccm methane flow. Scale bars: 50 µm*

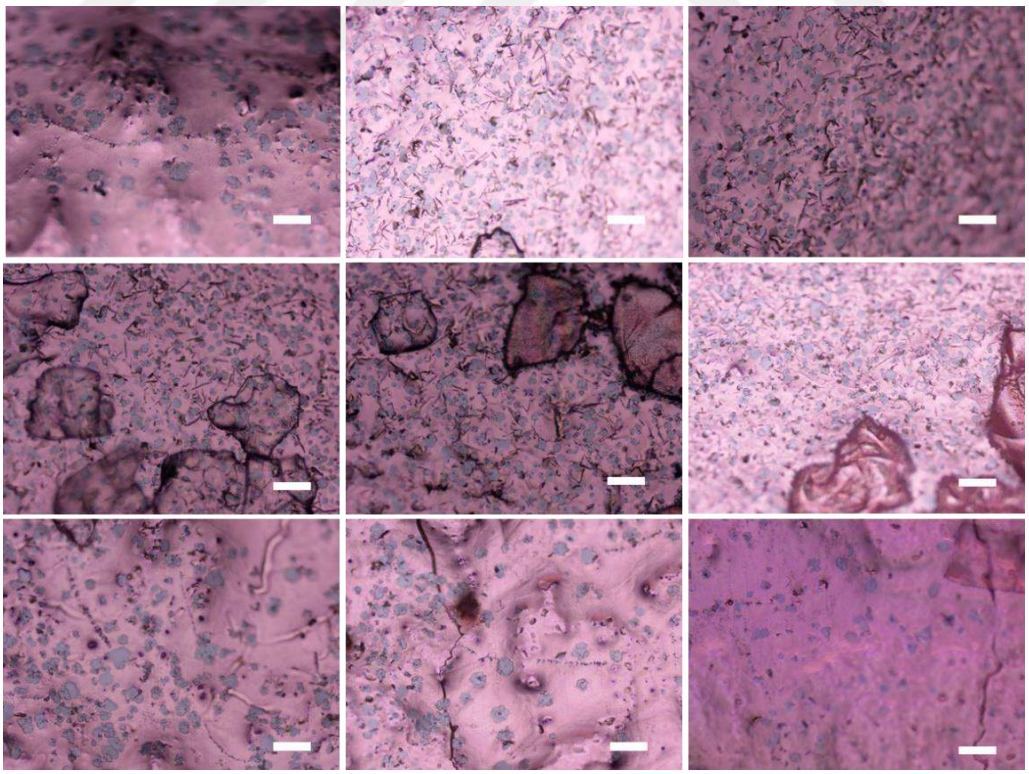

Figure 2.17. *Optical microscopy images of the experiment with 8 sccm methane flow. Scale bars: 50 µm*

The observations from the methane flow and temperature experiments indicated that temperature is a more effective parameter in the deposition of Mo_2C than others. Therefore, at first, it was decided that the growth time experiments should be performed at 1090 °C. This temperature was chosen because it was high enough to cause the copper to become liquid state, but not too high to mask the impact of growth time on the experiment. All experiments carried out regarding the growth time are shown in the Table 2.5.

Table 2.5. *Mo_2C process parameters for experiments carried out during different growth times*

Experiment Number	CH_4 Flow Rate (sccm)	Ambient Pressure (torr)	Temperature (°C)	Growth Time (min.)
1	4	764	1090	10
2	4	764	1090	30
3	4	763	1090	60
4	4	764	1150	30
5	6	738	1150	30
6	6	740	1175	30
7	0.7	763	1150	30
8	0.7	764	1150	60

Looking at Figure 2.18 and Figure 2.19, it was observed that the increase in growth time increases the size of Mo_2C flakes, so the coverage. However, no significant changes were observed in Figure 2.19 and Figure 2.20, probably due to carbon saturation.

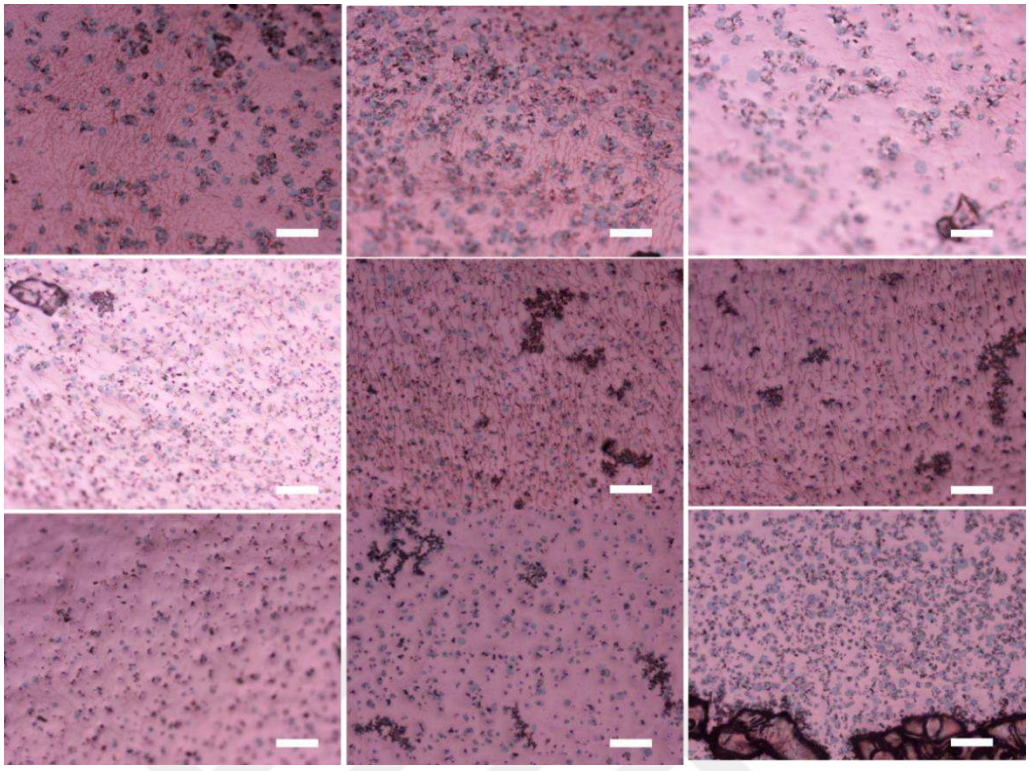

Figure 2.18. *Growth time experiment #1. Scale bars: 50 µm*

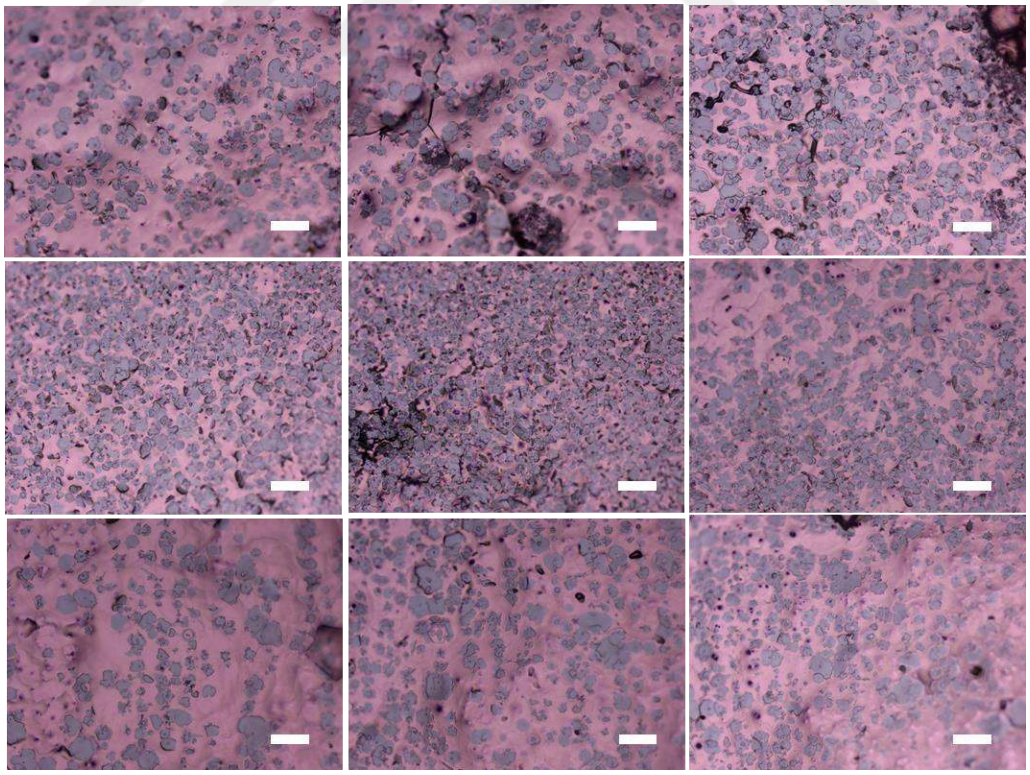

Figure 2.19. *Growth time experiment #2. Scale bars: 50 µm*

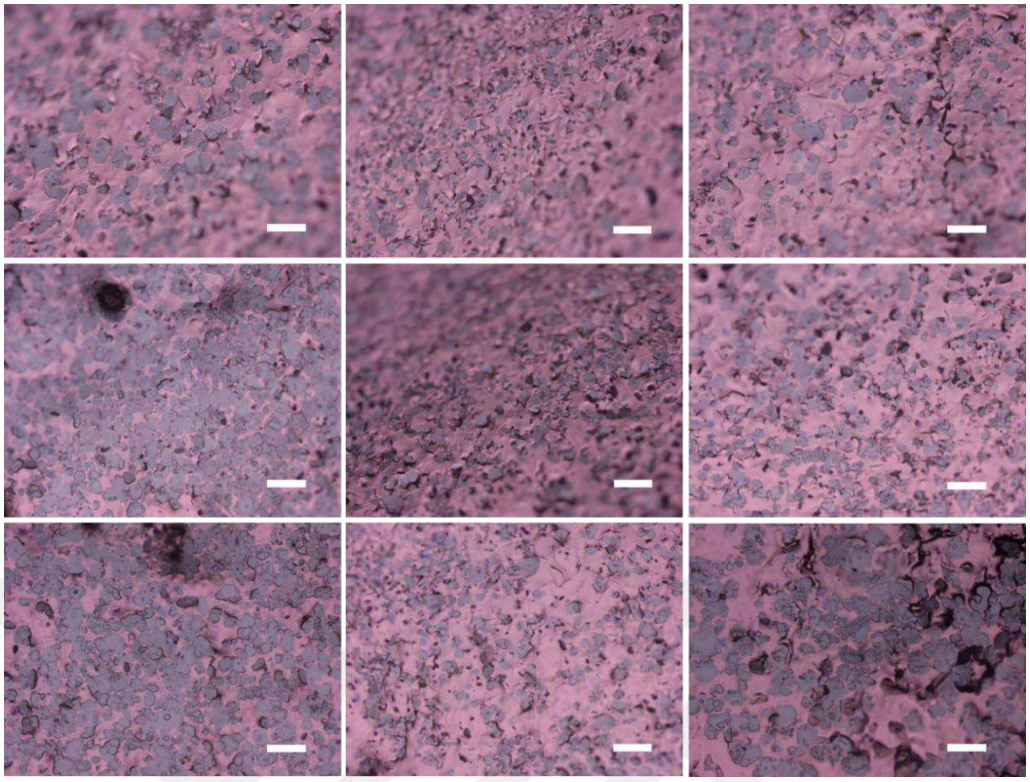

Figure 2.20. *Growth time experiment #3. Scale bars: 50 µm*

The aim of the experiments was to fully cover the surface with Mo_2C. Based on the previous experiments, it was believed that this aim could be achived by using 4 sccm of methane at 1150 °C for a duration of 30 minutes. Its result is displayed in Figure 2.21. Although the maximum coverage was achieved with the result shown in Figure 2.21, experiments 5, 6, 7, and 8, given in the table, were also carried out, because it was desired to reach the maximum coverage without overlapping of the flakes.

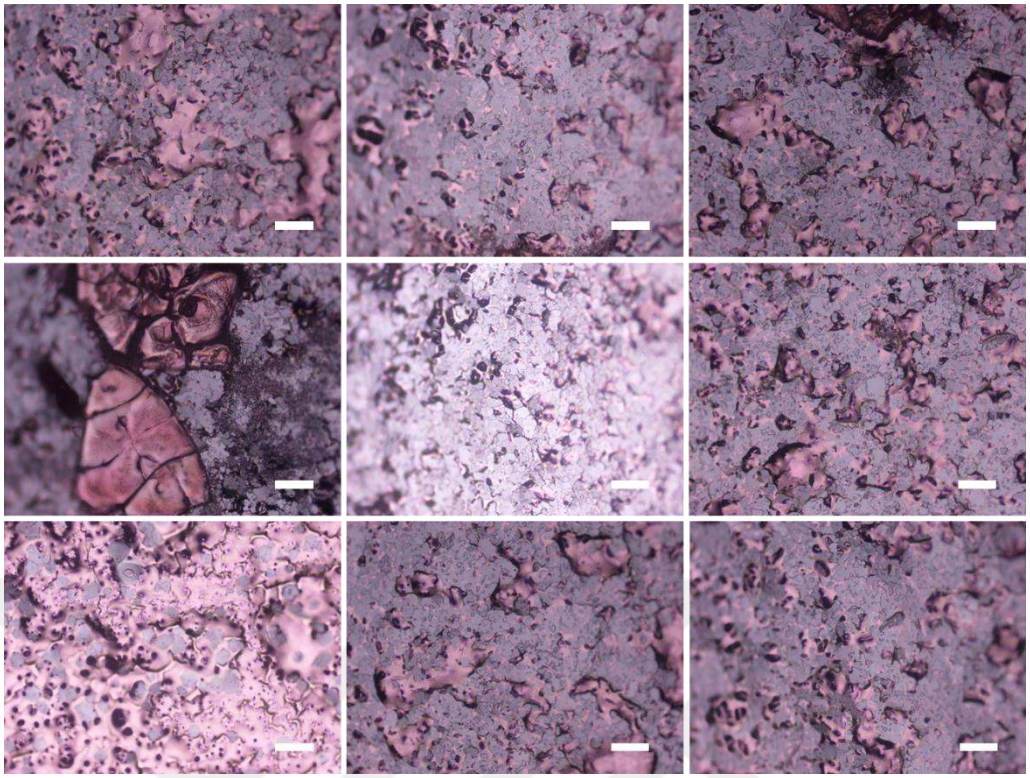

Figure 2.21. *Growth time experiment #4. Scale bars: 50 µm*

Looking at the results displayed between Figure 2.22 and Figure 2.25, it is observed that almost all of the surface is covered with Mo_2C, indicating that the goal was achieved despite overlapping of the flakes in some areas. It should be noted that in the experiments where 0.7 sccm of methane was used, a relatively flat deposition was observed due to the bottom-to-bottom arrangement of rod-shaped Mo_2Cs, instead of overlapping.

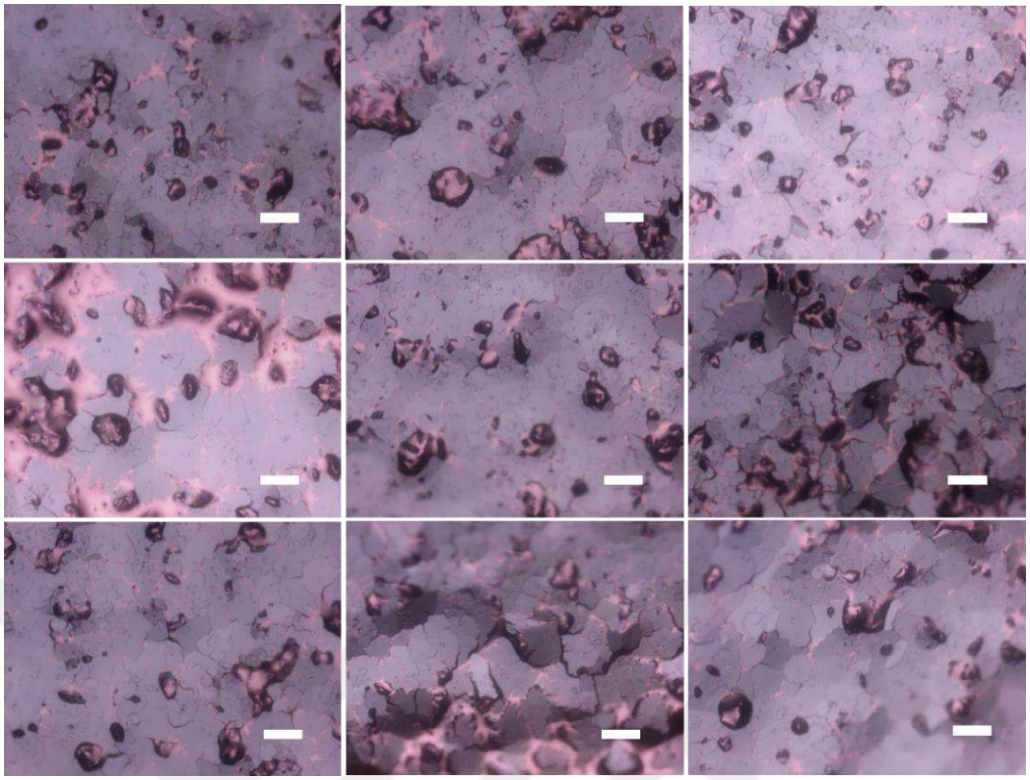

Figure 2.22. *Growth time experiment #5. Scale bars: 50 µm*

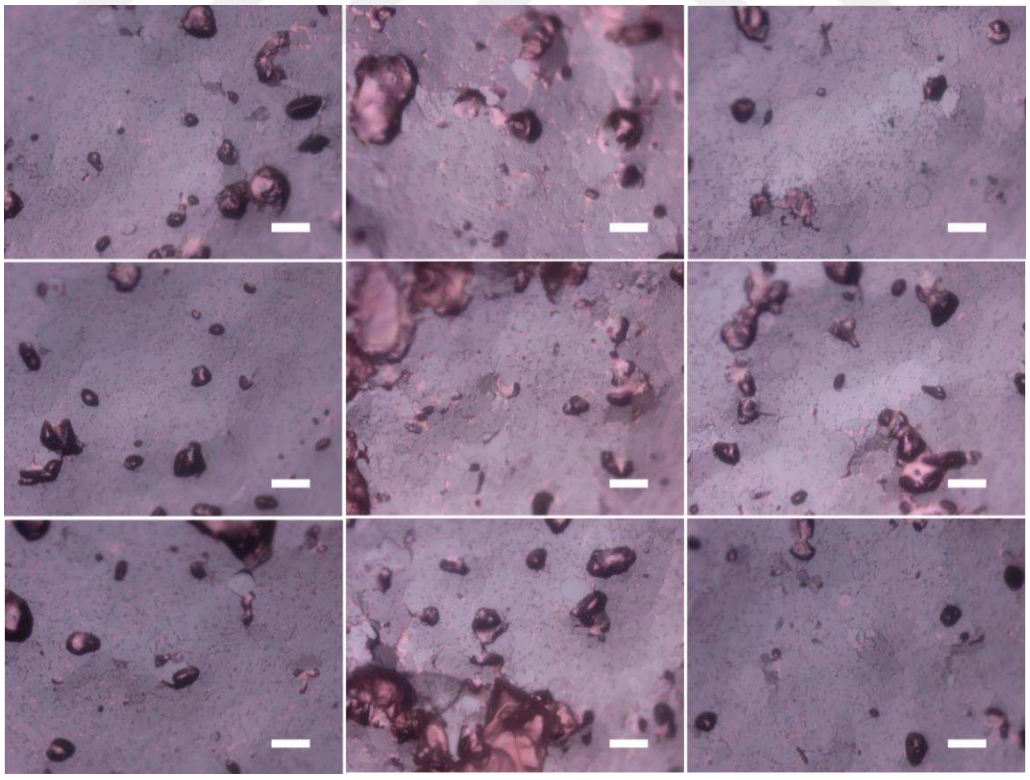

Figure 2.23. *Growth time experiment #6. Scale bars: 50 µm*

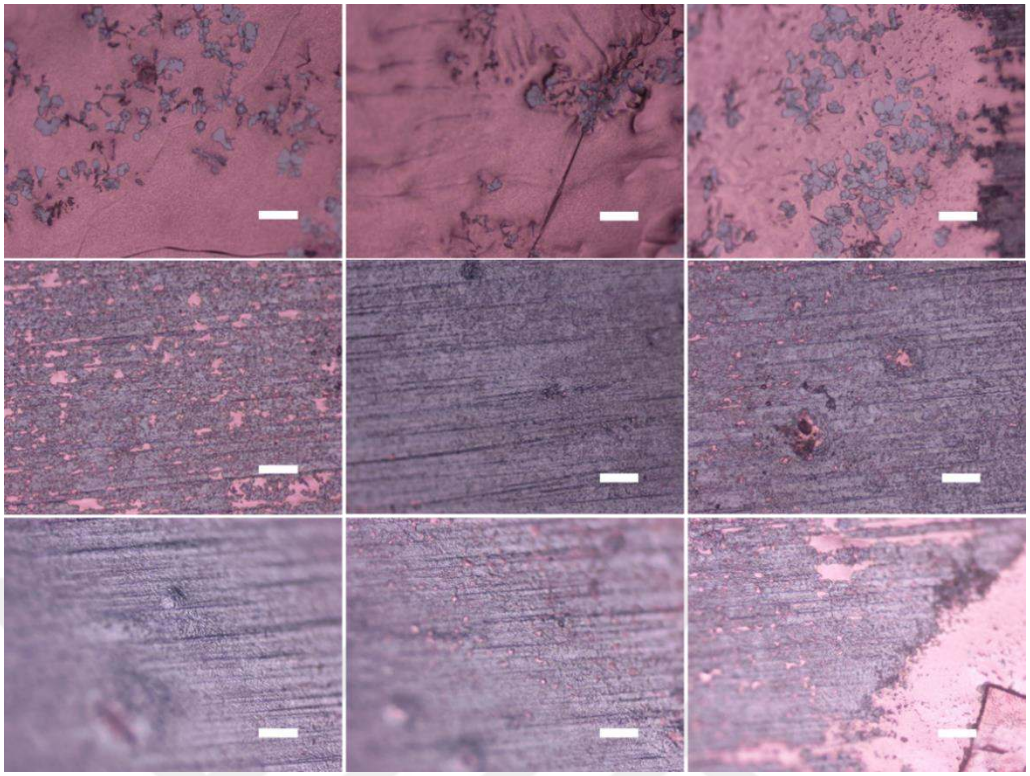

Figure 2.24. *Growth time experiment #7. Scale bars: 50 µm*

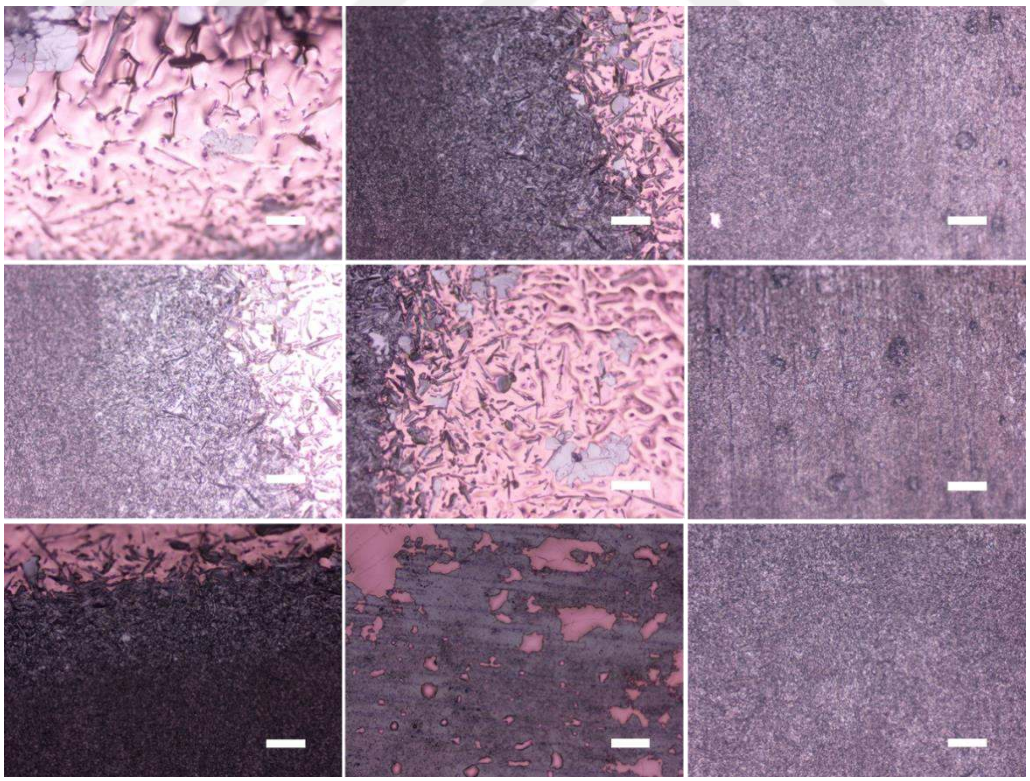

Figure 2.25. *Growth time experiment #8. Scale bars: 50 µm*

Prepared copper and molybdenum foils in all the experiments carried out so far were included in the CVD system on the quartz plate, and all of the obtained samples were made suitable for further use by a transfer process. In addition to these experiments, Mo_2C deposition was also carried out in order to dope to fibers. Since the sample removed from the CVD system was intended to be directly doped into the fibers, it was attempted to obtain two-way deposition of Mo_2C in the sample. For two-way deposition, configurations of the foils in the tube and experiments results obtained from these configuration are shown in the Figure 2.26. The foil configuration designed to catch methane gas flow from the side surfaces, resulted in a lower deposition of Mo_2C as shown in Figure 2.26 a). The densest deposition, on the other hand, obtained with the configuration that catches the methane from both the down surface and the up surface.

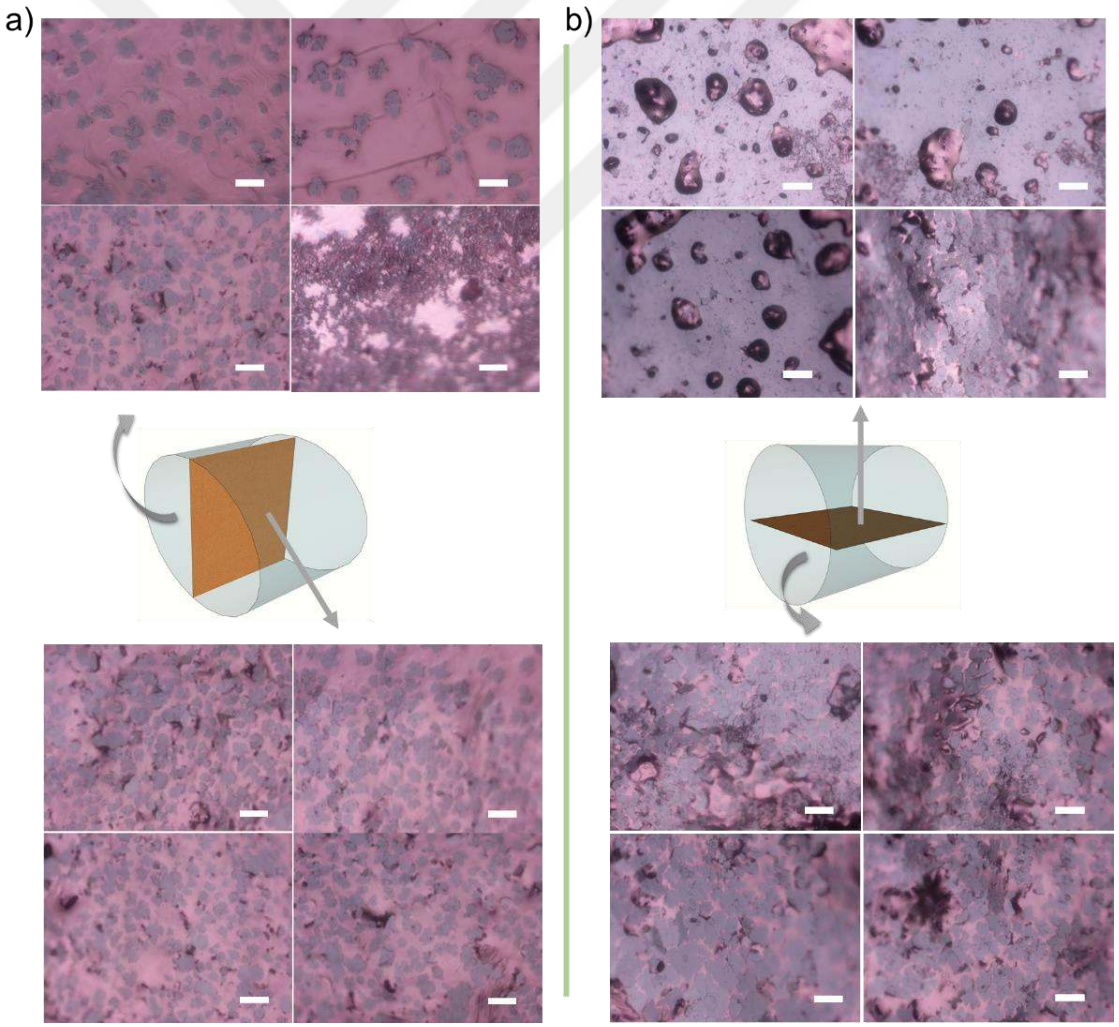

Figure 2.26. *Configurations for two-way deposition and the experiments results*

2.1.2.2. Mo_2C characterization

Mo_2C, one of the member of the MXenes, was firstly identified with a Raman spectroscope. The Raman spectrum of Mo_2C is displayed in Figure 2.27. To analyze the spectrum, the Lorentz model was used after subtracting the baseline. The positions of the peaks observed in the spectrum match the values reported in literature (Dechao Geng X. Z., 2016), (Chuan Xu S. S.-M., 2017), (Zhe Kang, 2019), (Tianshu Li, 2019). According to Tianshu Li et al., the peaks located at 170.7 cm^{-1} and 210 cm^{-1} classified as B_{3g} modes, while the peaks at 235 cm^{-1}, and 649 cm^{-1} are classified as A_g modes. Among these, the A_g modes and B_{3g} modes are mainly caused by the vibration of molybdenum atoms. Additionally, the A_g mode at 649 cm^{-1} is attributed to the vibration of carbon atoms and the peak at 141 cm^{-1} is attributed to both A_g and B_{3g} modes.

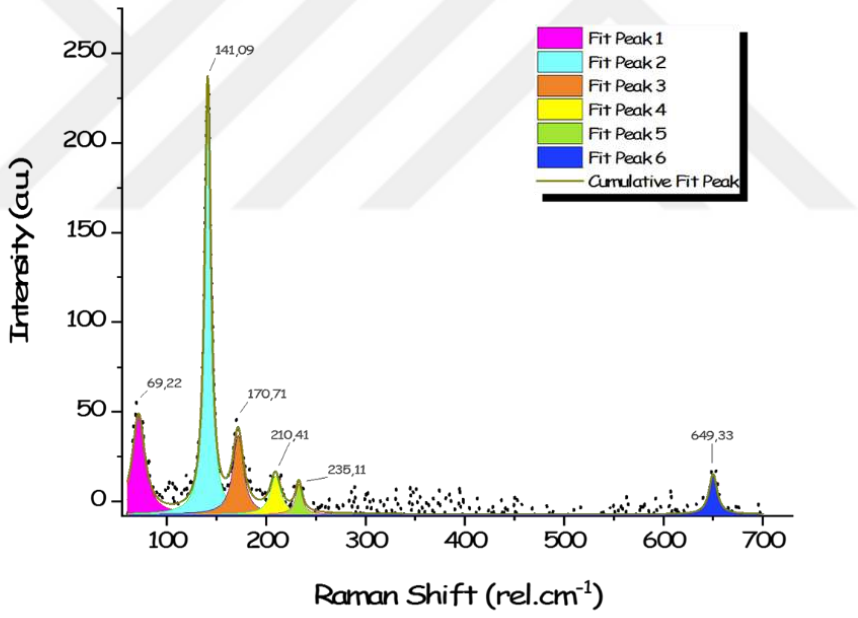

Figure 2.27. *Raman spectrum for Mo_2C on polycarbonate*

In Mo_2C deposition experiments, Mo_2C without graphene was obtained, which is different from what was previously reported in the literature. The Figure 2.28 displays both Mo_2C spectra with and without graphene that were deposited on molybdenum/copper alloy. The brown spectrum, without graphene, corresponds to the Mo_2C grown using a methane flow of 0.7 sccm. It should be noted that no graphene modes were detected in this spectrum. Moreover, it is worth mentioning that regardless of the

growth time and temperature, only Mo_2C peaks were identified in the Raman analysis when using a 0.7 sccm methane flow. On the other hand, when the flakes from all other deposition experiments were analyzed, both graphene and Mo_2C peaks were identified, as shown by the blue spectrum. Therefore, it is crucial to adjust the methane flow as 0.7 sccm, when it is not desired to have graphene within the Mo_2C deposition.

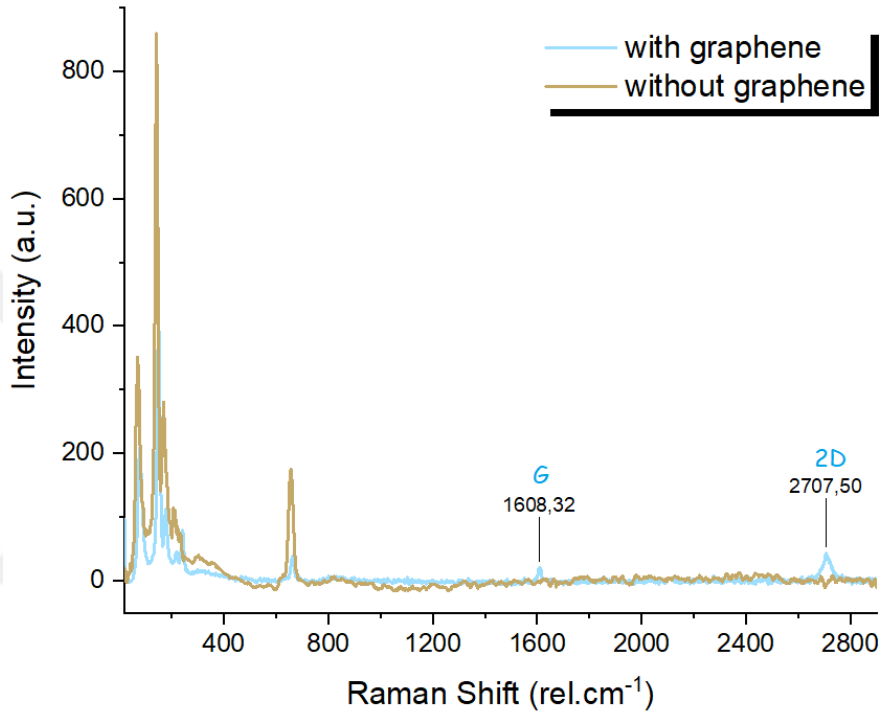

Figure 2.28. *Raman spectra for Mo_2C on molybdenum/copper alloy*

Although the peak positions of Mo_2C modes have been identified, there is insufficient information available to determine whether the peak positions or intensities can provide additional insights into the properties of the flakes. The following studies were carried out to establish a connection between Raman spectra and Raman data or flake structure. AFM data were taken from flakes with different thicknesses and line scan was taken from the same flakes. In addition, optical microscopy images of the same flakes were captured under both dark and bright fields. Calibration of the Raman device was performed prior to measurements to ensure precise outcomes. Using Origin program to intensity comparison of the spectra, the Raman data taken from the marked points on the microscopy image of the flakes were plotted on the same baseline as shown in Figure 2.29. All the Raman spectra were measured using the same 9 mW laser power, being

appropriate for comparison. As a result, there was no observed relationship between the thickness of the flakes and the intensity of the Raman signals. In addition, to investigate whether there is a correlation between peak positions and flake thickness, all the spectra were normalized and are shown in Figure 2.30 along with their peak positions. It was observed that only one peak shifted within the range of 650 rel.cm^{-1} - 655 rel.cm^{-1}, whereas the positions of the other peaks remained constant. At first, this peak seemed to shift in proportion to the thickness, but subsequent measurements did not support this observation. The AFM data for the flakes, which were subject to Raman measurements, are included in Figure 2.31 with their optical microscopy images.

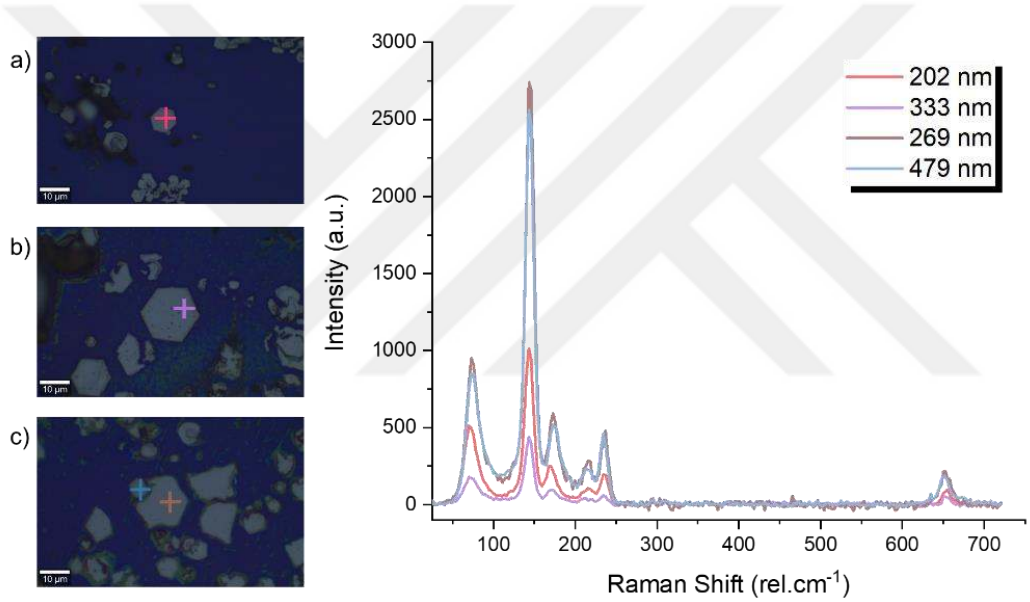

Figure 2.29. *Optical microscopy images of the flake with their marked measurement points; and their Raman spectra. The thicknesses of the flakes: a) 202 nm, b) 333 nm, c) 479 nm and 269 nm. Scale bars: 10 µm*

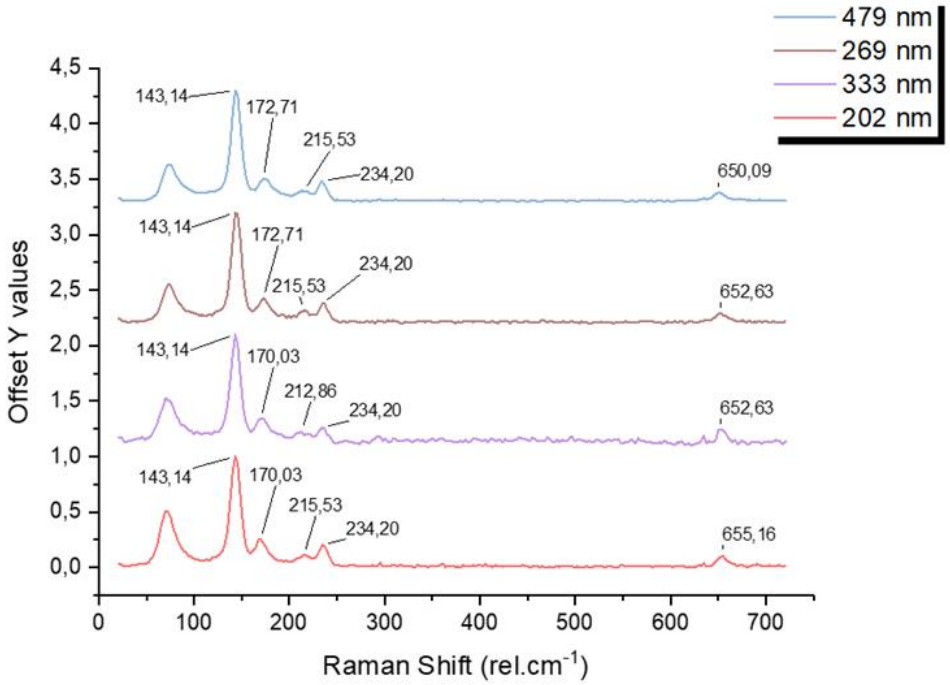

Figure 2.30. *Normalized Raman spectra for the flakes, which have different thicknesses*

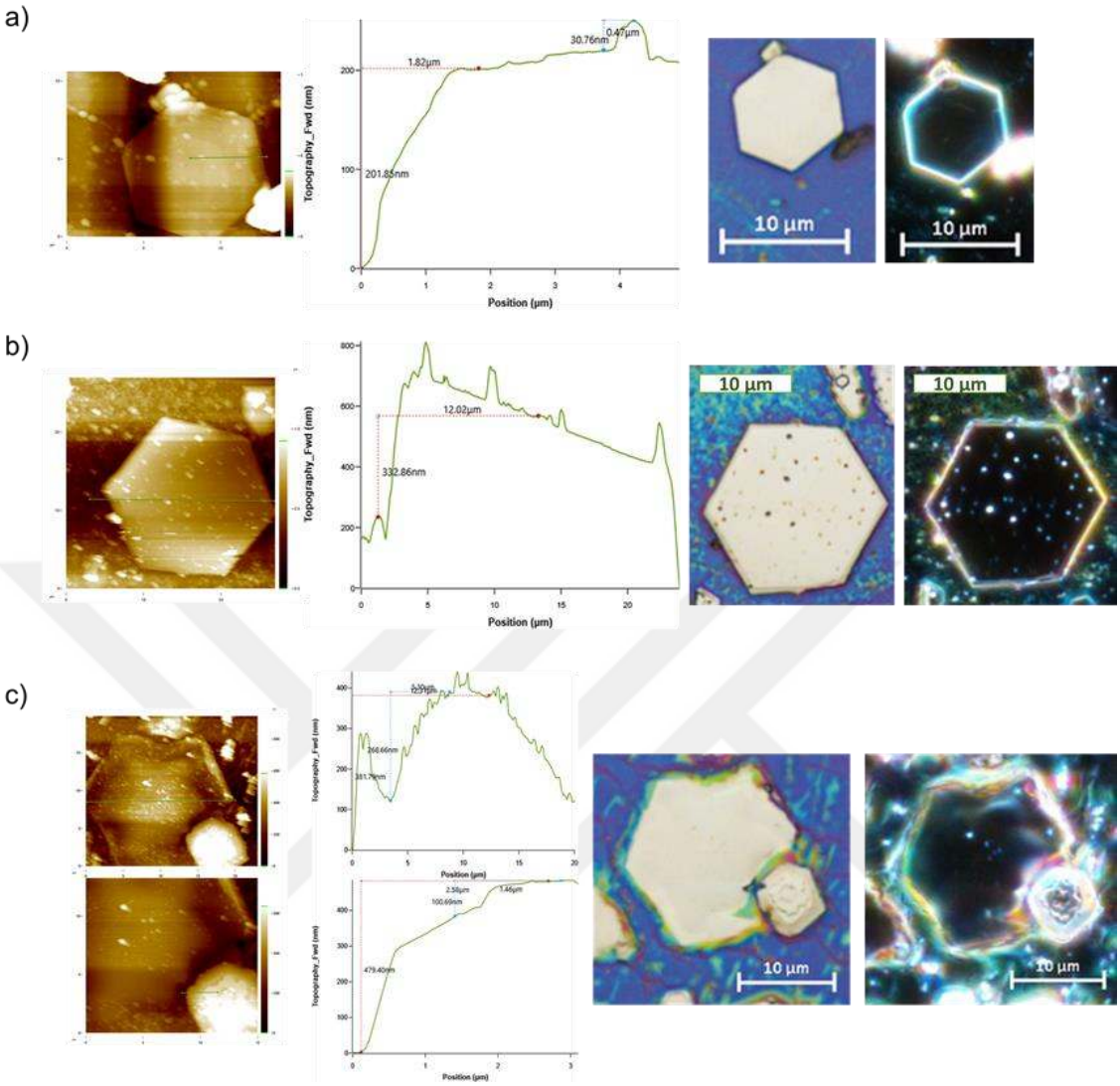

Figure 2.31. *Data for flakes of different thicknesses: Topographies, the height profiles along the green line, bright field and dark field optical microscopy images, respectively*

While an initial observation suggested a correlation between peak shifting and flake thickness, subsequent measurements revealed the opposite. Figure 2.32 shows that the peak shifted within the range of 650 rel.cm^{-1} - 655 rel.cm^{-1} is not related to the thicknesses of the flakes. Measurements in Figure 2.32 were taken with 5mW laser power.

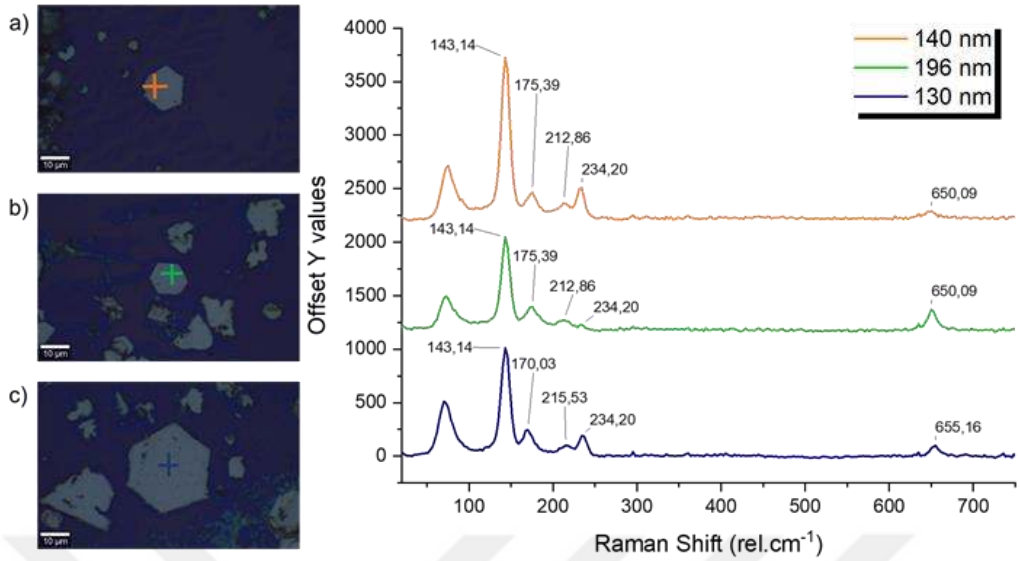

Figure 2.32. *Optical microscopy images of the flake with their marked measurement points; and their Raman spectra. The thicknesses of the flakes: a) 140 nm, b) 196 nm, and c) 130 nm. Scale bars: 10 µm*

The laser power used for measurement varies, due to the variance in thickness of MXene flakes. For example, a laser power of 8 mW caused burns on a 60 nm thick sample during measurement. Therefore, not all measurements in this study could be performed using the same laser power. Only, measurements taken at the same laser power were used for comparison purposes. Thus, the data presented in Figure 2.30 and Figure 2.32 cannot be directly compared. Nevertheless, both these figures together still indicate that the peak shifting between 650 rel.cm^{-1} - 655 rel.cm^{-1} is not related to the thickness of the flakes. Data for the flakes, where in Figure 2.32 is also presented in Figure 2.33.

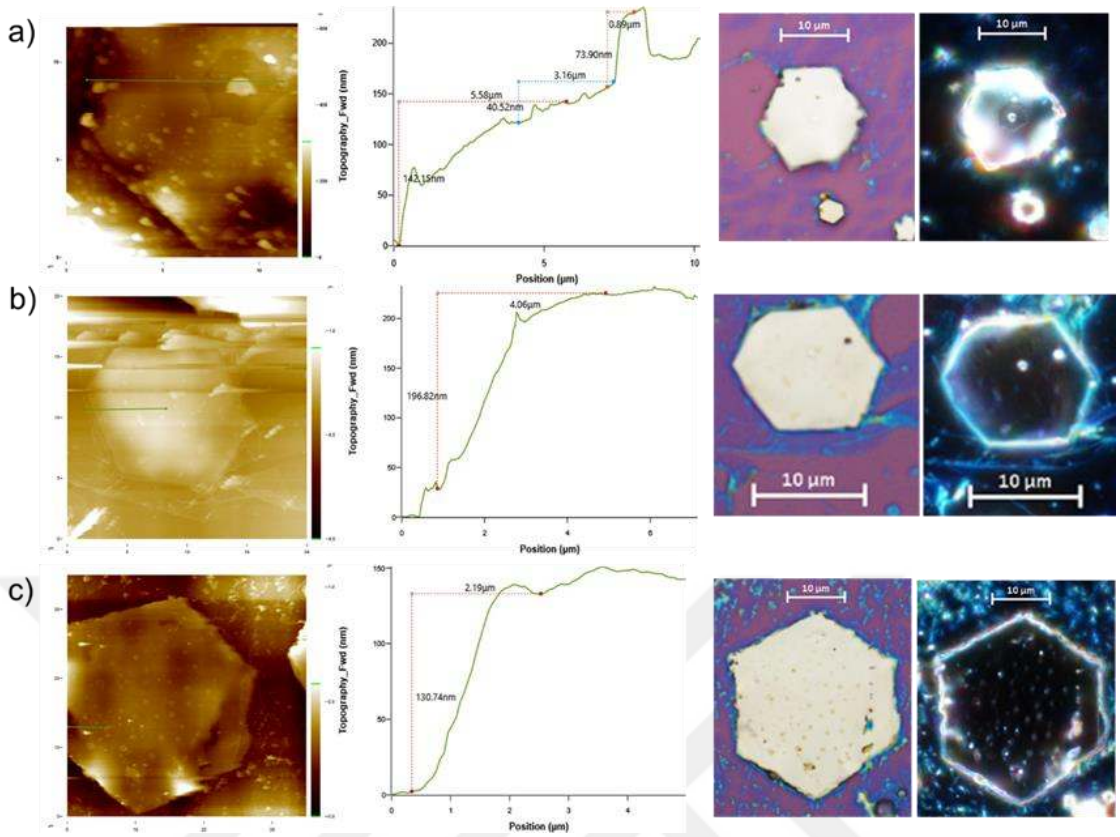

Figure 2.33. *Data for flakes, where in Figure 2.32: Topographies, the height profiles along the green line, bright field and dark field optical microscopy images, respectively.*

Despite investigating a large number of MXene flakes using Raman spectroscopy and AFM, no relationship was found. However, contrary to the literature, it was observed during these measurements that the thickness of the flakes was not related to the methane flow rate or temperature used in the deposition experiments (Merve Öper, 2022), (Dechao Geng X. Z., 2016). For example, even in the experiments of Mo_2C deposition used 2 sccm methane flow, 355 nm flake could be obtained, as displayed in Figure 2.36, whereas the experiment used 10 sccm methane flow could be concluded with average ~156 nm flakes, as displayed in Figure 2.33. Meanwhile, all flakes shown in Figure 2.33 were obtained as a result of experiments carried out using a methane flow of 10 sccm at 1150 °C. It was observed that increasing the methane flow rate did not lead to an increase in the thickness of Mo_2C flakes. In fact, the thickness of the flakes is not affected by the increase in methane flow rate. This conclusion is supported by the following figures. The CVD deposition experiment did not provide homogeneous flake thicknesses. Furthermore, the temperature did not affect the thickness of the flakes. Figure 2.39 and Figure 2.40 show results obtained from an experiments carried out at 1090 °C. These results (Figure 2.39,

Figure 2.40) contradicts the claim that an increase in temperature leads to an increase in flake thickness, when compared to the results in Figure 2.33, where the methane flow rate is kept constant at 10 sccm and only the temperature changes. These results are just a few among many experiments carried out, and other experiments also support the same conclusion.

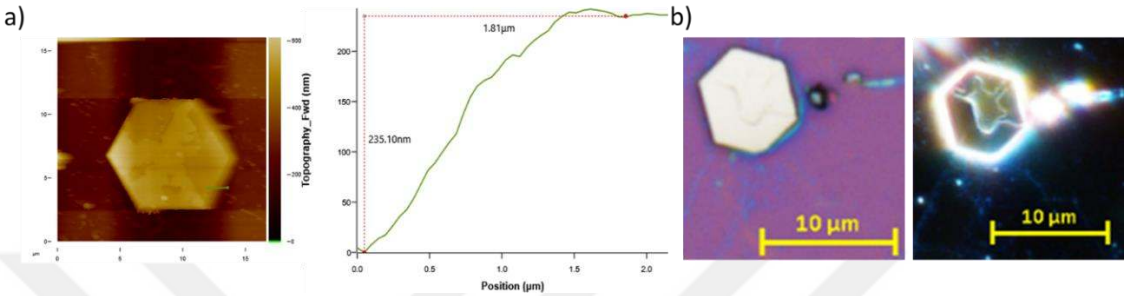

Figure 2.34. *a) Topography of a flake, which occurs with 2 sccm methane flow rate at 1150 °C and the height profile of 235.10 nm along the green line b) Bright field and dark field optical microscopy images of the flake*

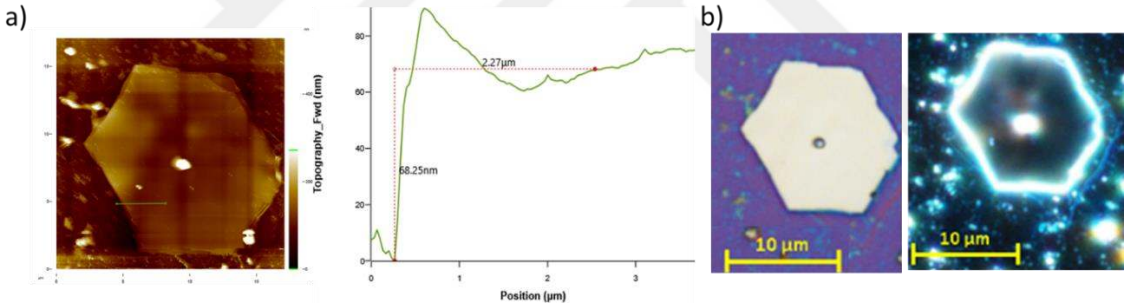

Figure 2.35. *a) Topography of a flake, which occurs with 2 sccm methane flow rate at 1150 °C and the height profile of 68.25 nm along the green line b) Bright field and dark field optical microscopy images of the flake*

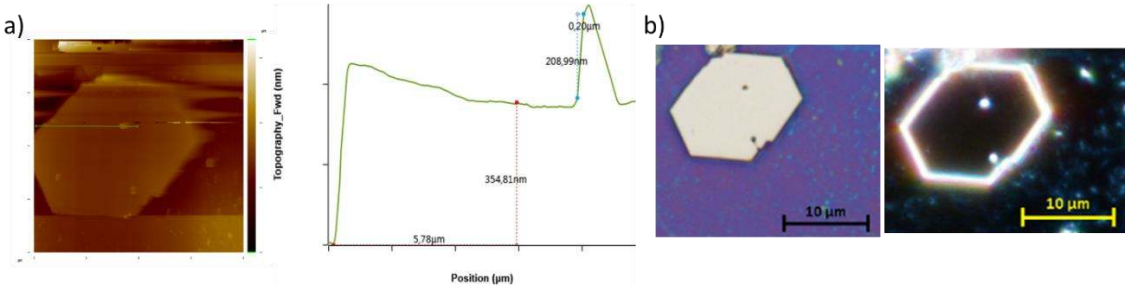

Figure 2.36. *a) Topography of a flake, which occurs with 2 sccm methane flow rate at 1150 °C and the height profile of 354.81 nm along the green line b) Bright field and dark field optical microscopy images of the flake*

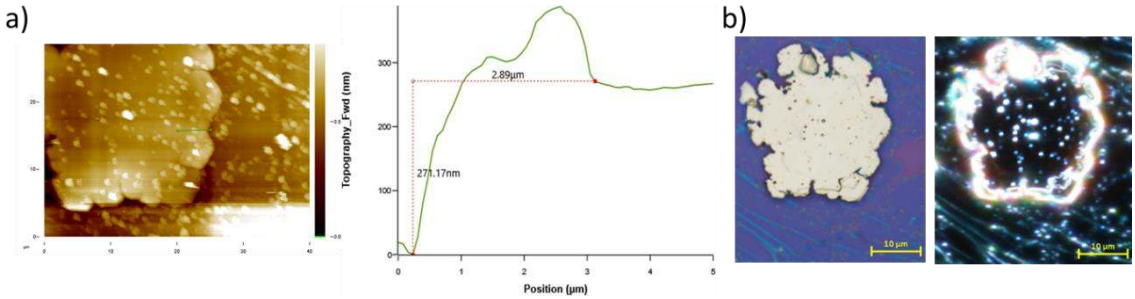

Figure 2.37. *a) Topography of a flake, which occurs with 6 sccm methane flow rate at 1150 °C and the height profile of 271.17 nm along the green line b) Bright field and dark field optical microscopy images of the flake*

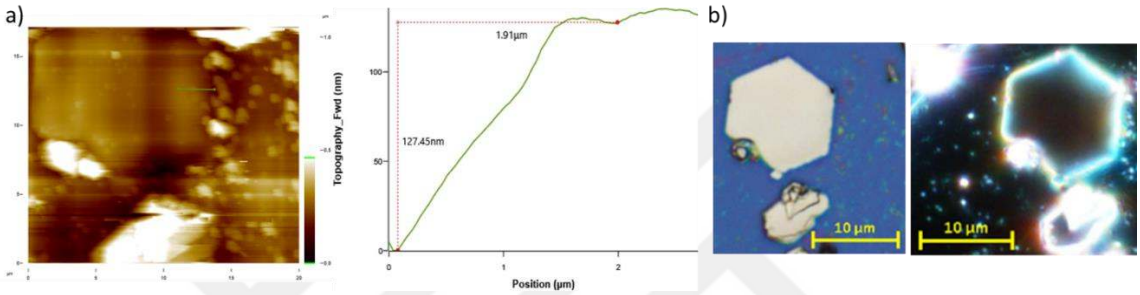

Figure 2.38. *a) Topography of a flake, which occurs with 6 sccm methane flow rate at 1150 °C and the height profile of 127.45 nm along the green line b) Bright field and dark field optical microscopy images of the flake*

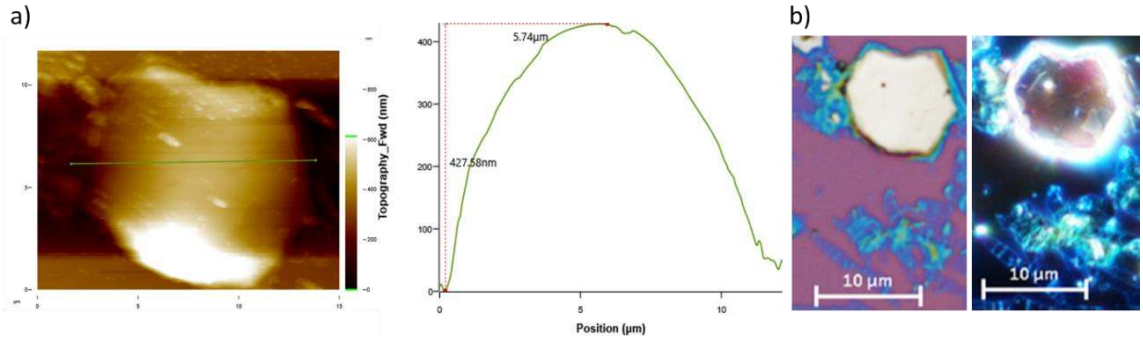

Figure 2.39. *a) Topography of a flake, which occurs with 10 sccm methane flow rate at 1090 °C and the height profile of 427.58 nm along the green line b) Bright field and dark field optical microscopy images of the flake*

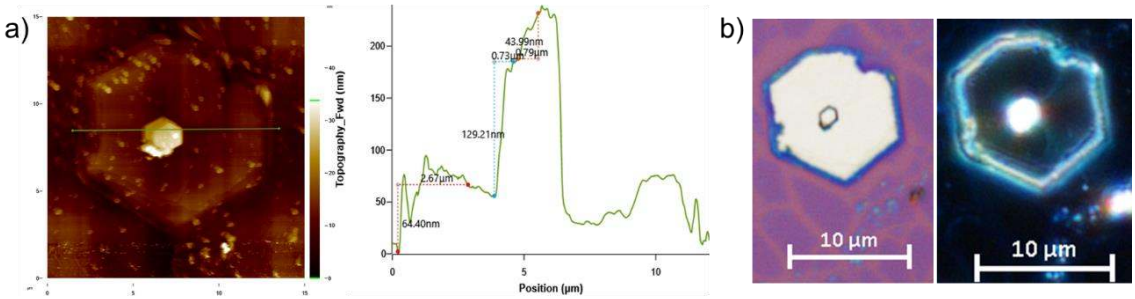

Figure 2.40. *a) Topography of a flake, which occurs with 10 sccm methane flow rate at 1090 °C and the height profile of 64.40 nm and 236.61 nm along the green line b) Bright field and dark field optical microscopy images of the flake*

2.1.3. Molybdenum disulfide deposition

Monolayer MoS_2 was obtained via the CVD method consisting of a 2.7-inch horizontal quartz tube. Glass and SiO_2/Si were used as substrates. After the cleaning process of the substrates, they were placed with precursors onto the quartz plate as shown in Figure 2.41. Glass and SiO_2/Si were placed over a graphite foil on the quartz plate. Graphite foil is used to prevent the cracking of glass. Glass serves a dual purpose as both a substrate and a catalyst. Due to the presence of Na+ ions within it, glass catalyzes the deposition process. About 0.5 mg MoO_3, as a precursor, was placed 4 cm in front of the substrates. 300 mg sulphur, as a reactance, was placed 15 cm in front of MoO_3. The quartz plate was placed in such a way that the sulphur is outside of the heating zone at first as shown in Figure 2.41. Then, 150 sccm of nitrogen was introduced into the tube with a mass flow controller and used as a carrier gas throughout the process. When the temperature reached 750 °C, the furnace of CVD was pulled left so that the sulphur part is also included in the heating zone ~5 min. At the end of the time, the zone was cooled down rapidly. Finally, when the heating zone dropped below 100°, the flow of nitrogen gas was stopped, and the quartz plate was removed from the tube. The process was performed under ambient pressure.

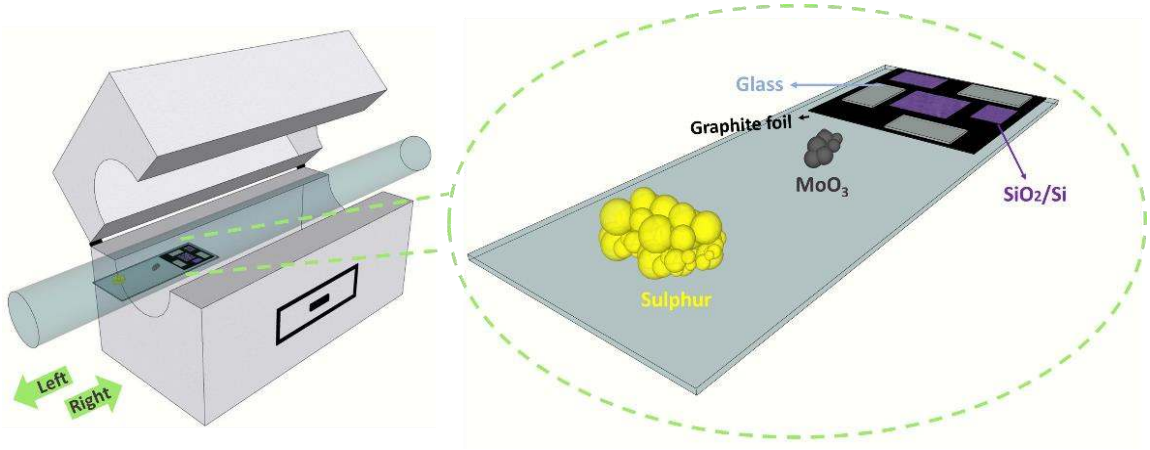

Figure 2.41. *Schematic of CVD system for MoS_2. Inset: The top view of the precursors and substrates on the quartz plate placed in the quartz tube*

2.1.3.1. Molybdenum disulfide characterization

MoS_2, one of the TMDCs, was firstly identified with a Raman spectroscope. The Raman spectrum of MoS_2, which was deposited on glass substrate, is displayed in Figure 2.41. To analyze the spectrum, the Gauss model was used after subtracting the baseline. E_{2g} (in-plane atomic vibration) and A_{1g} (out-of-plane atomic vibration) modes of MoS_2 were detected at 387 rel.cm^{-1} and 407 rel.cm^{-1}, respectively. The difference between the E_{2g} and A_{1g} modes can also provide information about the MoS_2 layer. In this case, the 21 rel.cm^{-1} difference indicates that the MoS_2 deposited on glass is a monolayer (Hüseyin Şar, 2019).

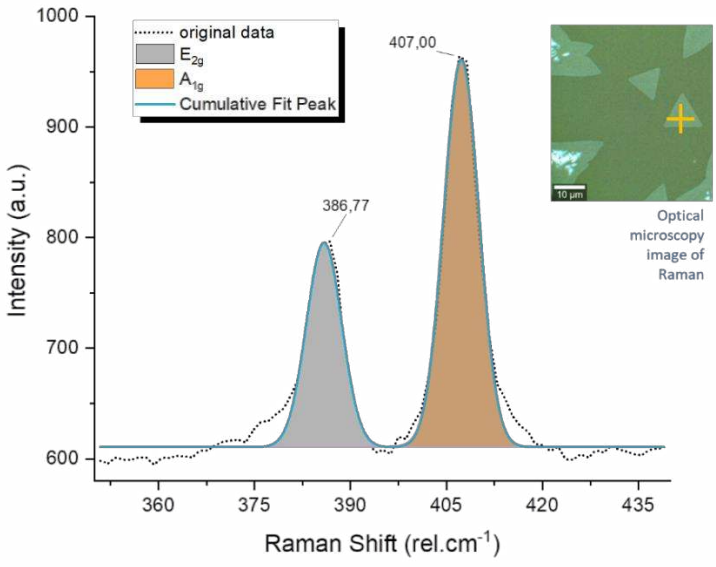

Figure 2.42. *Raman spectrum for MoS_2 on glass and the microscopy image*

The deposited MoS_2 on glass was transferred onto a SiO_2/Si to perform AFM measurements. Figure 2.43 shows a topography of MoS_2 on SiO_2/Si, with a measured height profile of 0.76 nm. The thickness of a monolayer MoS_2 is reported values ranging from 0.7 nm to 1.2 nm in the literature (Alexandar D. Marinov, 2023). Therefore, this measurement also confirms that the deposited MoS_2 is a monolayer.

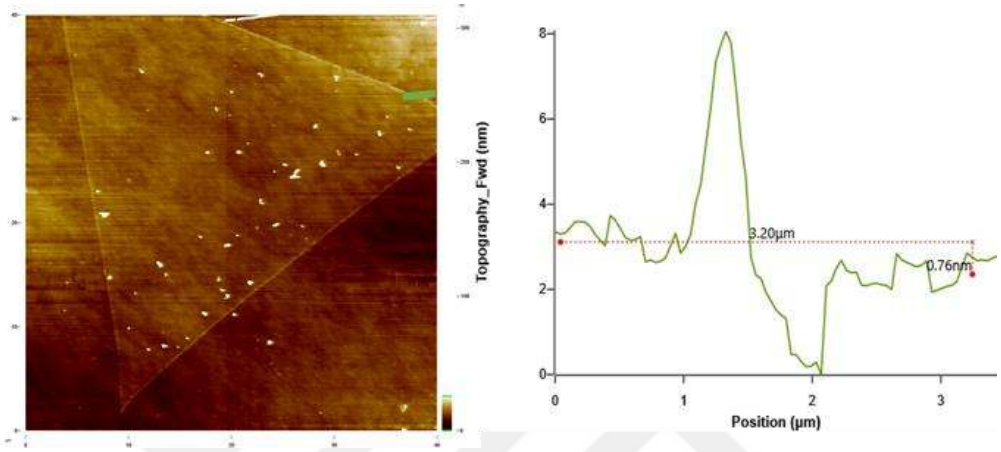

Figure 2.43. *Topography of the MoS_2 on SiO_2/Si and the height profile along the green line in topography*

The shape and appearance of MoS_2 flakes can vary depending on several factors, such as the synthesis method, and substrate. However, in our laboratory, MoS_2 deposited by CVD generally has a triangular shape. An example of MoS_2 deposited on SiO_2/Si is shown in Figure 2.44.

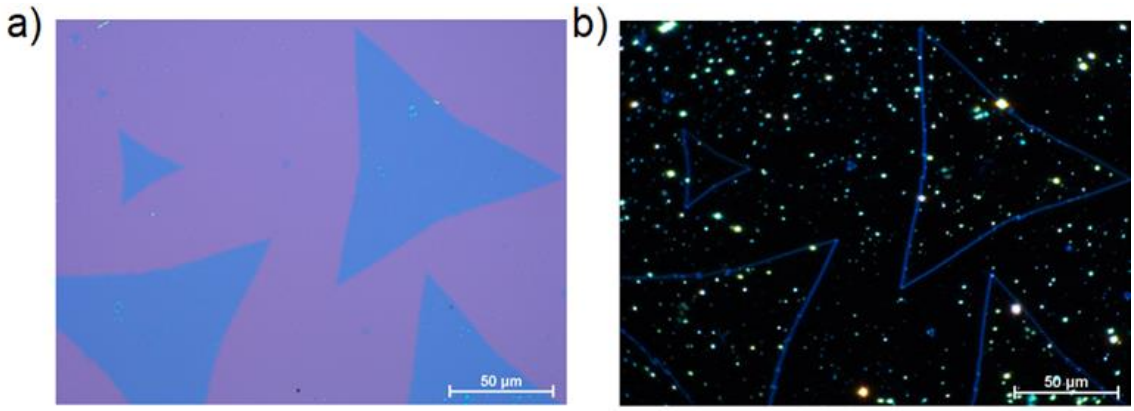

Figure 2.44. *Optical microscopy images of MoS_2 on SiO_2/Si under a) bright and b) dark fields*

2.2. Transferring 2D Materials

Transferring 2D materials to the desired substrates is necessary in order to perform further characterization or integrate 2D materials into devices. For example, Raman spectroscopy has not been feasible on the copper foil used for growing graphene, due to the metallic properties of copper. Another example, foils are not suitable for lithography because they are typically not flat enough to achieve the necessary precision for lithographic patterning. Therefore, transferring the material onto a flat substrate such as silicon wafers or glass is necessary.

The nano-sized materials produced during the transfer process are vulnerable to external factors, making it crucial to handle them systematically during experiments to avoid potential risks. Each transfer step is a critical process that requires careful attention, and hundreds of experiments have been carried out to optimize the transfer process.

2.2.1. Photoresist assisted transfer

This transfer process is suitable for 2D materials obtained by deposition on metal foil in CVD, such as graphene and Mo_2C. To begin the process, the sample (either graphene or Mo_2C) is initially positioned onto the quartz plate. Then, photoresist is dripped onto it, and it is then placed in the furnace. After a certain period of time, the sample is removed and left in a metal solvent. Once the bottom metal layer etched away by the solvent, the sample undergoes appropriate cleaning processes, is placed on the desired substrate, and completely adhered using a hot plate. The sample is then put in a suitable solvent to remove the photoresist layer, and undergoes final cleaning processes to complete the transfer.

The most important part of this process is the etching away of the metal layer, which has been extensively studied through numerous parameters. These parameters include determining the optimal solvent, amount of solvent, dissolution time, cleaning and drying times. In addition, temperature and time settings during the use of a hot plate are also important parameters to consider. All these vary depending on the material being used and the substrate onto which it will be transferred. For example, Figure 2.45 shows a Mo_2C sample is immersed in an iron chloride solution, where the white flakes that have lost molybdenum/copper alloy layer underneath and the black alloy that has not completely yet disappeared visible. The optical microscopy captured the image around three and a half hours after the sample was added to the solution. The image reveals that

a uniform etching is not formed, and as a result, the flakes that have lost the underlying metal layer faster are exposed to iron chloride for a longer duration. This causes damage to the formed flakes, making them fragile and eventually causing them to break and fall apart.

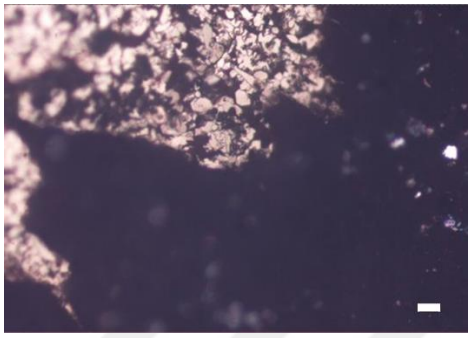

Figure 2.45. *Mo_2C sample in a solution of iron chloride after ~3.5 hours later. Scale bar: 30 µm*

Despite all efforts, it has been found to be highly challenging to closely monitor and manage the etching away of the foils. Despite all experiments, it has not been possible to maintain the flakes in their original form. In experiments where ammonium sulphate was used instead of iron chloride, the time taken to etch was ~48 hours. In some cases, there was no etching observed, but instead, only the foils on the side that came into contact with the ammonium sulfate solution turned black, and there was no shedding of the sample. These experiments were repeated at temperatures above room temperature for both iron chloride and ammonium sulphate. Increasing the temperature shortened the etch time for ammonium sulfate and increased the destruction for iron chloride. As a result, even though CVD resulted in full coverage of MXene flakes, not all the flakes could be successfully transferred to the desired substrates.

In case the substrate is polycarbonate, the damage of the solvents to the polycarbonate is another highly challenging parameter to consider. The reaction of polycarbonate to photoresist solvents is as shown in Figure 2.46. Upon contact, the reaction of acetone can be immediately observed, while in the case of ethanol, the effects can be seen under an optical microscope and are directly proportional to the duration of the polycarbonate's exposure to the solvent. They cause polycarbonate to swell or dissolve, which leads to surface damage, cracking, or even complete failure of the substrate. To say that the remover does not cause any damage would not be right, but it can be noted that the polycarbonate typically remains mostly undamaged after a certain

amount of contact time. Therefore, the remover was chosen as the solvent for photoresist as a compatible with polycarbonate to avoid damages to the substrate.

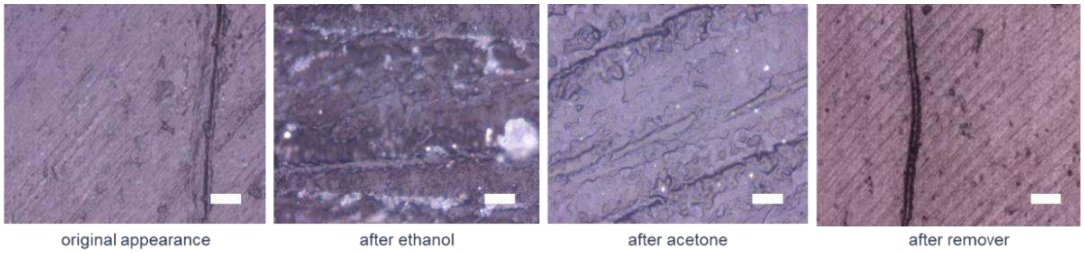

Figure 2.46. *Optical microscopy images of the polycarbonate, its original appearance, and its appearance after exposure to the specified chemicals, respectively. Scale bars: 50 µm.*

The thickness of the photoresist layer dropped on the sample is not the most critical factor, but still noteworthy. There are various causes of transferrin failure, including the photoresist layer being too thick or too thin or not being left for an enought duration in the oven or being left for too long. When the layer is too thick, it may be exposed to acetone for a prolonged time, resulting in more damage to the 2D material. Conversely, when the layer is very thin, it is fragile and may break during cleaning or adhesion, leading to losses. Moreover, leaving it in the oven for too long causes it to become more fragile and lose its holding feature, while leaving it for too little time may cause the 2D material to curl or fold during the transfer from one process to another since it does not completely lose its fluidity.

2.2.1.1. Results of the photoresist assisted transfer

The microscopy images on the substrates of the 2d materials carried out with photoresist assisted transfer are presented in this section. Graphene transfers were also confirmed by Raman spectra. In Figure 2.47, microscope images of polycarbonate and carbon fiber, on which graphene was transferred, are presented with marked Raman measurement points. The spectrum taken from the blue marked point on the polycarbonate in Figure 2.47 a) confirms the presence of bilayer graphene on it. Likewise, according to the spectrum taken from the orange marked point on the carbon fiber in Figure 2.47 b), the existence of multilayer graphene is confirmed.

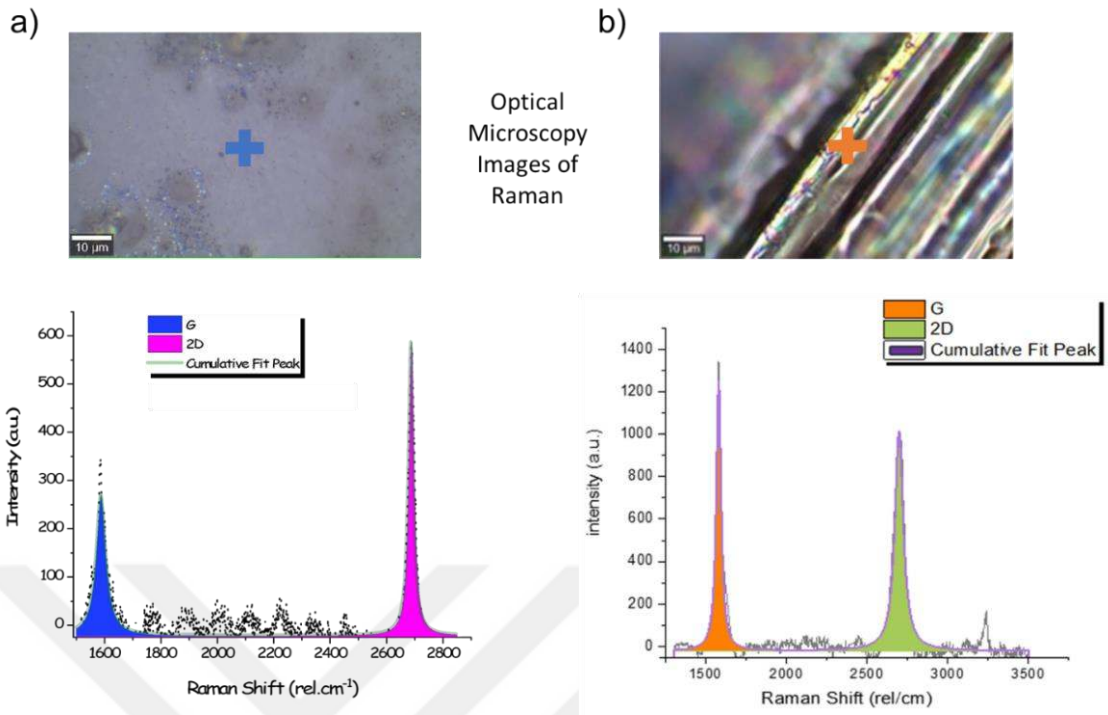

Figure 2.47. *Optical microscopy images of graphene and their Raman spectrum on a) polycarbonate and b) carbon fiber. Scale bars: 10 µm*

The Figure 2.48 shows photoresist assisted MXene transfers. The full coverage MXenes obtained from CVD was attempted to be transferred to polycarbonate, SiO_2/Si, carbon and glass fiber, but some flakes were lost due to factors discussed earlier. Approximately half of the desired MXenes were successfully transferred to the substrates.

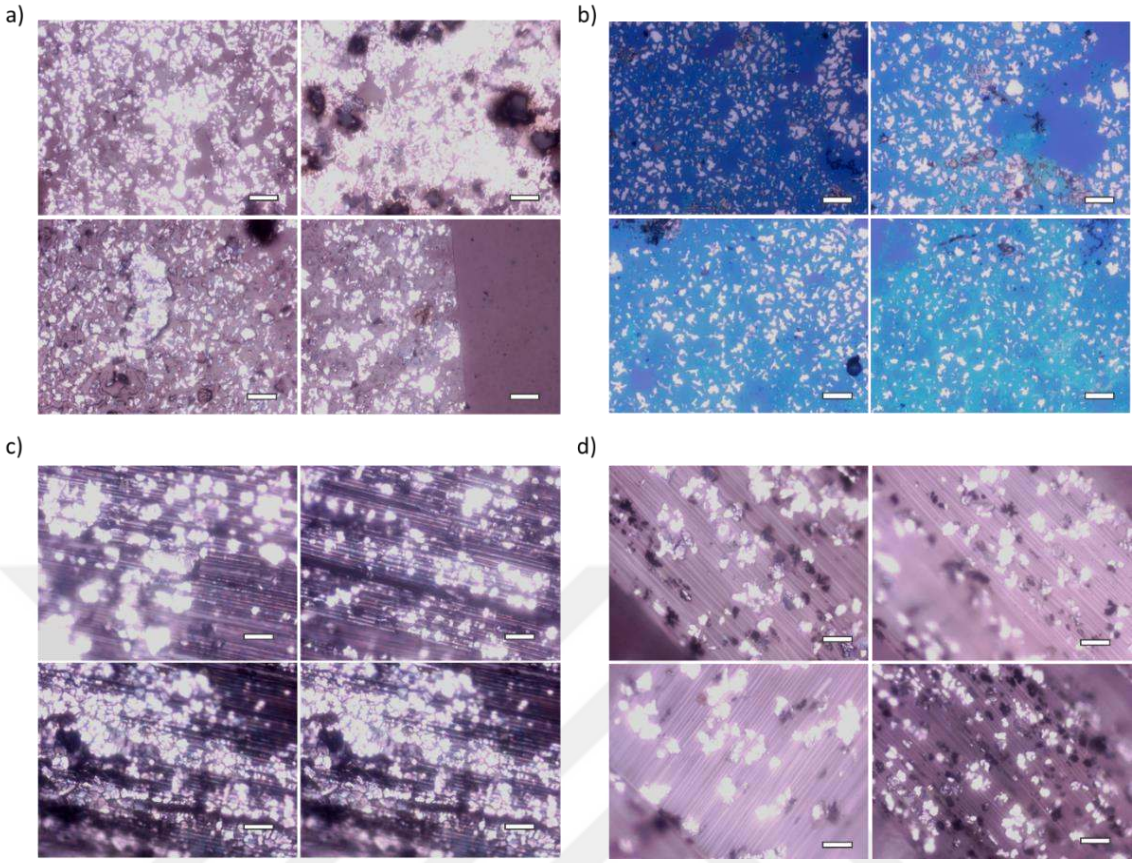

Figure 2.48. *Optical microscopy images of MXene flakes on a) polycarbonate, b) SiO_2/Si, c) carbon and d) glass fiber, respectively. Scale bars: 50 µm*

2.2.2. PMMA assisted transfer

This transfer process is suitable for 2D materials obtained by deposition on the hydrophilic nature of substrate, such as MoS_2 on glass. To begin the process, the sample (MoS_2) is initially spin-coated with PMMA and then baked on a hot plate, which causes the PMMA to wrap around the edges of the glass. To allow permeation of water, the PMMA layer at the edge must be carefully cut with a knife. 2D material attached to PMMA are then peeled off the glass by gradually immersing them in DI water at an right angle. The resulting film of PMMA and 2D material floats on top of the water and can be removed using a target substrate. The sample is then baked to remove all moisture and ensure complete adhesion using a hot plate. Finally, the sample is placed in a suitable solvent to remove the PMMA and undergoes a series of cleaning processes to complete the transfer.

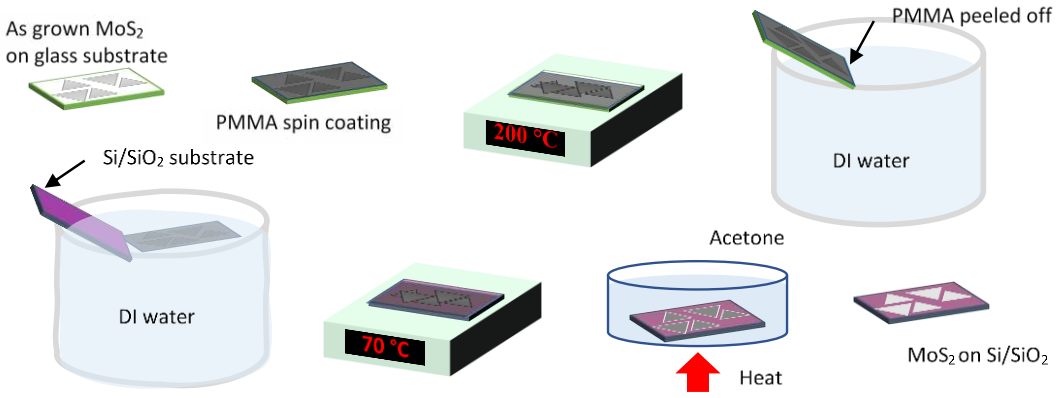

Figure 2.49. *Illustration of the hydrophilic peel-off technique (Wonge Lisheshar Ibrahim, 2022)*

3. GRAPHENE TRANSFERRED CARBON FIBERS: INVESTIGATIONS INTO CONDUCTIVITY MEASUREMENTS

Graphene was transferred onto carbon fiber in order to improve the existing properties of carbon fibers and to add functional properties to the fibers. In recent years, composite materials have increasingly replaced traditional raw materials due to their superior strength-to-weight ratio, high impact resistance, and damage tolerance, specially for thermoplastic and thermosetting materials used in avionic applications. With the assistance of graphene, by improving the composite materials using the carbon fiber in mechanical, electrical and thermal aspects; it is desired to reach lighter in weight and more conductive composites. The following section presents the pathways followed to accurately measure the conductivity of carbon fiber, as well as the changes in conductivity with the transfer of graphene.

3.1. Choosing the Contact Material

The best choice of contact material is determined by considering factors such as the stability of the resistance readings over time and the level of resistance achieved. To determine which contact material is most effective, the resistance of the carbon fiber was measured over different contact materials, including copper foil, silver paste, and aluminum sheet. The results obtained by measuring the carbon fiber's resistance over these contacts were compared with the results obtained by measuring the resistance of the carbon fiber without contact. The measurement results obtained with the multimeter are presented Table 3.1. Based on the results obtained, it was conclude that the best contact material for carbon fiber is silver paste. While the resistance values for aluminum sheet and copper foil were very high, silver paste achieved the desired level of resistance and demonstrated the most stable resistance readings over a short period.

Table 3.1. *Measurement results of carbon fiber over different contact materials*

Contact Materials	Contact Distance (mm)	Resistance (ohm)
Copper foil	45	11
	20	9
	11	7.3
	5	5.3

Aluminum sheet	42	18
	28	14.7
	22	10
	9	10
Silver paste	42	1.08
	28	0.92
	15	0.86
	12	0.74
without contact material	43	1.66
	35	1.54
	30	1.26
	19	0.93
	7	0.8

In addition, according to the graph in Figure 3.1, it is clearly seen that the resistance values with silver paste and without contact material are close to each other. This indicates that silver paste has a minimal effect on the resistance of the carbon fiber, which is another reason to choose it as a contact material.

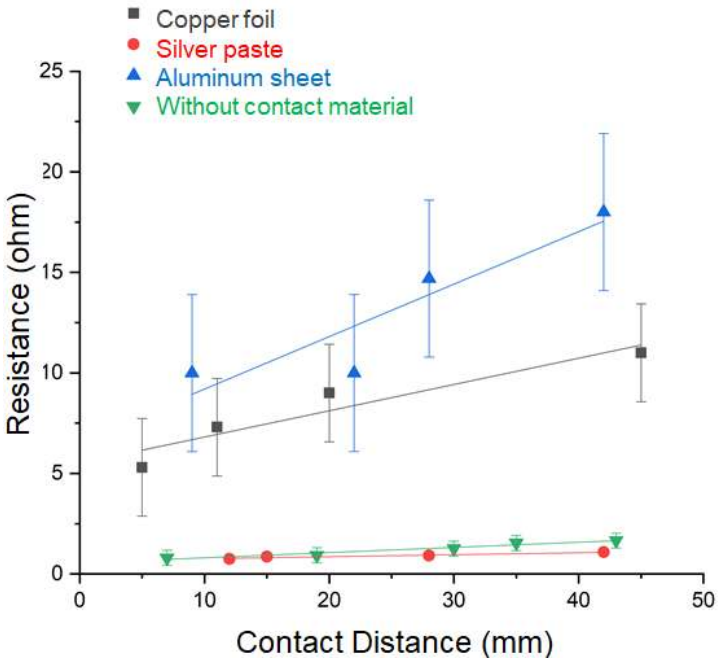

Figure 3.1. *Graph of resistance versus contact distance measured over different contact materials of the carbon fiber*

The Figure 3.2 displays the silver paste contacts created on the carbon fiber with specific distances, as well as the corresponding probe positions during the measurements.

Figure 3.2. *Distance based measurement images on silver paste contacts*

3.2. Impact of Chemicals Used During Transfer on Measurement Results

In order to investigate the effect of the chemicals used in the transfer method on the measurement results, the resistance of the carbon fiber was measured again by exposing it to the transfer process. While the resistance of the carbon fiber over various contact materials was measured using a multimeter, at this stage the measurements were carried out using a probe station as shown in Figure 3.3. The thin tips of the probe station were not able to make a proper contact with the perforated and non-tight weave structure of the carbon fiber, resulting in measurement issues. The problem was resolved by connecting the probe tips to the carbon fiber contacts using crocodile cables.

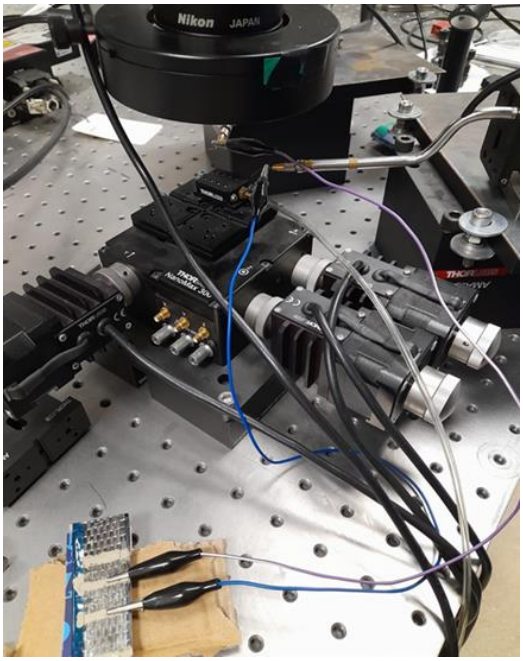

Figure 3.3. *Used probe station for the measurements*

The carbon fiber was subjected to a gradual increase in voltage through the interfece of probe station software over a specific time period. The corresponding changes in current and voltage were systematically recorded, and resistance values were computed based on the recorded data. To improve the reliability of the results, the measurements were repeated multiple times for a single distance. The Table 3.2 presents the achieved average measurement results.

Table 3.2. *Measurement results of carbon fiber with and without transfer process*

	Contact Distance (mm)	**Resistance (ohm)**	**Error Margin (ohm/mm)**
without transfer	41.079	1.054	0.017
	27.163	0.903	
	13.886	0.725	
	10.711	0.688	
with transfer process	27.509	0.873	0.023
	14.019	0.862	
	9.929	0.698	

Upon examining the measurement results, it was found that the margins of error were quite low and the resistance values obtained were in close proximity to each other. it was concluded that the chemicals used in the transfer method caused a slight increase in the resistance of the carbon fiber, but within an acceptable range. In other words, the impact of the chemicals used in the transfer process on the resistance of the carbon fiber is negligible and does not pose a concern.

3.3. Multilayer Graphene-Transferred Carbon Fiber

Multilayer graphene was transferred to carbon fiber. Then, the carbon fiber was subjected to movement and twisting to test its durability and see if it can produce consistent results under different conditions during the probe station measurement. This movement and twisting caused to introduce additional noise and variability in the measurements, especially since the carbon fiber bonds are not tight, so there was unstable electrical transmission between the layers of the carbon fiber. Therefore, margin of error and variance values were relatively higher. The same conditions were subjected to the un-transferred carbon fiber and measurements were taken in the same way. The graph of

the resistance curves based on the distance for both carbon fibers are presented in Figure 3.4.

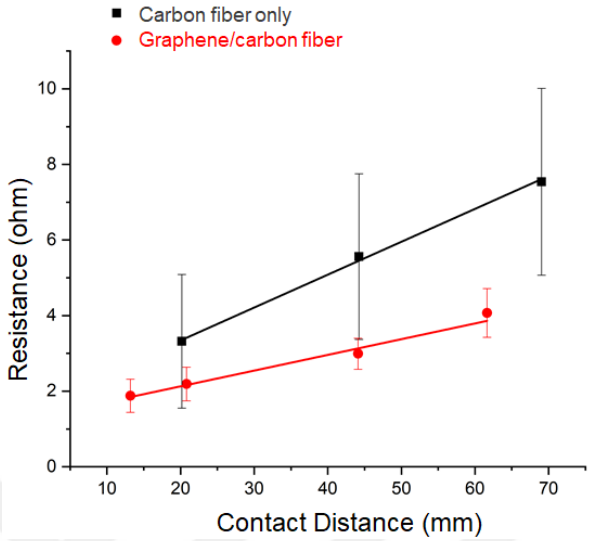

Figure 3.4. *Graph of resistance versus contact distance measured for multilayer graphene transferred and un-transferred carbon fiber.*

In the formula $R = \rho\, {}^{l}/_{A}$; R is resistance, ρ is resistivity, l is length, A is cross-sectional area. As seen in the formula, length and resistance are directly proportional. As the contact distance increases, the resistance value also increases. The linear regression curves of the resistance values are also seen in the Figure 3.4. Calculations were performed using the slope ($^{R}/_{l}$) of this curve (Mckenzie, 2015). The slope of the graphene-transferred curve is 0.042 Ω/mm. The cross-sectional area of the graphene-transferred sample is 10.39 mm^2. Considering the given values in the formula, the impedance value is calculated as 0.43 Ω.mm. In the $\sigma = {}^{1}/_{\rho}$ formula; σ denotes the intrinsic conductivity, and the intrinsic conductivity value was calculated as 2.32 $S.mm^{-1}$ according to this formula. Values for un-transferred carbon fiber were also calculated using the formulas given above. According to the processes performed, the intrinsic conductivity value was calculated as 1.12 $S.mm^{-1}$. Thus, it was calculated that the intrinsic conductivity of the carbon fiber increased by a factor of approximately 2.07 as a result of the multilayer graphene transfer.

Until now, silver paste was first applied to the carbon fiber and then direct measurement was taken through the silver contact after the paste had dried. From now, in order to reduce the additional noise during measurements, the carbon fiber placed

between PETs in a sandwich-like configuration as shown in Figure 3.5. As soon as the silver paste was applied, while it was still in its fluid state, copper wires were added in equal numbers onto the silver paste contacts. Then, it was dried, allowing the copper wires to adhere to the silver paste. Afterwards, it was placed between the PET strips, and then attached via laminating machine, with the copper ends left uncovered.

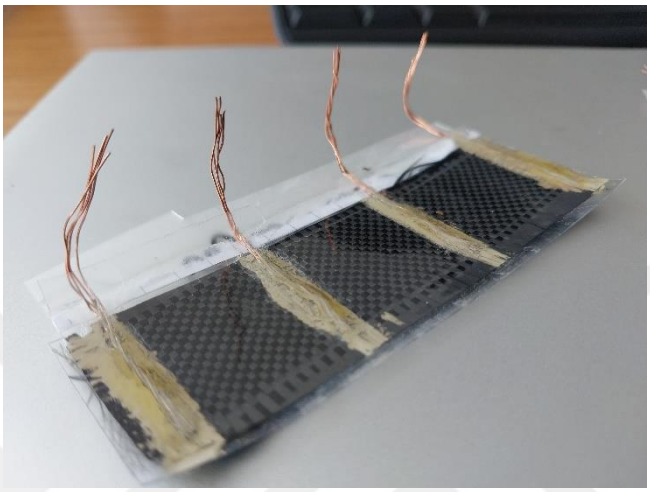

Figure 3.5. *The carbon fiber between PET strips*

The carbon fiber measured between PET strips was the carbon fiber supplied to our laboratory for the second time. That is, it was different from the one used in previous studies. The carbon fiber again was subjected to movement and twisting while being measured. The Table 3.3 presents the achieved average measurement results with standard deviations'. The laminating helped to firmly bond the carbon fiber and copper wires to the PET strips, reducing noise and variability in the measurements. In addition, copper wires helped to improve the contact, providing consistent flow of current. Thus, more stable of the resistance readings were recorded over time.

Table 3.3. *Measurement results of second carbon fiber with and without graphene transfer*

	Contact Distance (mm)	**Resistance (ohm)**	**Standard Deviation**
	80.55	1.662	0.043
second	48.66	1.186	0.031
carbon	47.39	1.397	0.154
fiber	21.41	0.741	0.108
	21.91	0.775	0.087

	76.287	1.808	0.014
With	56.648	1.426	0.007
multilayer	35.786	1.017	0.010
grafen	35.148	0.927	0.011
	15.421	0.539	0.012

However, unlike in the previous study, the graphene transfer was not able to increase in conductivity. As presented in the previous section, when determined using the linear regression curve, the intrinsic conductivity value of the second carbon fiber was 22.01 $S.mm^{-1}$. This value significantly greater than the previous intrinsic conductivity of the carbon fiber. The intrinsic conductivity of the second carbon fiber was measured to be 16.75 $S.mm^{-1}$ after transferring the graphene onto it. It is possible that the graphene did not show an enhancement in conductivity due to the high conductivity of the carbon fiber substrate. However, further investigation and analysis is required to determine the specific cause of the reduced conductivity.

4. MOS_2 DIRECTLY GROWN ON MXENE (MO_2C): INVESTIGATIONS INTO FLUORESCENCE LIFETIME IMAGING MICROSCOPY AND PHOTOLUMINESCENCE MAPPING

TMDCs offer great flexibility in terms of tuning their properties to obtain novel functionalities for potential applications in optoelectronics. In addition, heterostructures yield an extended range of functionalities via mixing and matching materials of different composition, structure, and dimensionality. The MoS_2/Mo_2C heterostructure is one of the example of such a combination. In this combination, MoS_2 is the effective light source, while Mo_2C is a metallic (Xianhu Zha, 2016). There are a few studies where MoS_2 and Mo_2C are used together. Jaeho Jeon et al. reported an epitaxial synthesis of Mo_2C via partial conversion of MoS_2 with thermal annealing, where they investigated a Mo_2C/MoS_2 junction using four probe and Hall measurements (Jeon, 2018). Another Mo_2C/MoS_2 junction also was reported by Seunghyuk Choi et al (Choi S., 2019). They synthesized Mo_2C from MoS_2 using a lithographically patterned SiO_2 masking layer via CVD and investigated electrical transport characterization of MoS_2/Mo_2C lateral junction. However, in this study, MoS_2 has been grown directly on Mo_2C by CVD method for the first time. Here, the effect of Mo_2C MXenes, a metallic material, on MoS_2, in 2H phase, has been observed using Raman, PL, and FLIM. CVD method contributes to the size of a growing structure to reach the required level of device integration. In addition, CVD method provides Mo_2C MXenes without functional groups (F, H, OH, and/or O) and according to theoretical studies, the majority of pure MXenes exhibit more powerful properties. The structure characterization of MoS_2/Mo_2C has been performed via a μ-Raman system. The surface morphology of the structure has been observed on tapping mode with AFM. Exciton dynamics have been observed by photoluminescence measurements. The fluorescence decay rates of the excited states of photons which created by light absorption have been revealed for the structure with FLIM, which is created via an intensity of each pixel determined by the lifetime.

This study points out that stacking different materials creates a synergetic effect which is critical in controlling optical transitions and should be considered for designing optoelectronic devices. Although research on the interlayer interaction in the hybrid structures is still in its early stages, they are up-and-come.

4.1. CVD Growth

The deposition process of MoS_2/Mo_2C on SiO_2/Si begins with the molybdenum carbide, which is a member of the MXenes family. Mo_2C is obtained via the chemical vapor deposition system consisting of a 1-inch horizontal quartz tube. Molybdenum foil, as a transition metal source, and copper foil, as a catalyst for capturing carbon atoms, are placed in the quartz tube as shown in Figure 2.5. The process parameters such as growth temperature, growth time, and gas flow rate are adjusted according to the experiments presented in 2.1.2.1 in order to obtain Mo_2C as desired. After obtaining Mo_2C MXene flakes, they are transferred to the SiO_2/Si substrate. As the final step of the heterostructure formation, the transferred Mo_2C MXene flakes on SiO_2/Si are placed in another CVD, which consists of a 2.7-inch horizontal quartz tube optimized for 2D TMDC growth. The illustration of the precursors and substrates on the quartz plate is in Figure 4.1 a). Glass, SiO_2/Si and $Mo_2C/SiO_2/Si$ are placed on a graphite foil on the quartz plate. MoO_3, as a precursor, is placed in front of the substrates. Sulphur, as a reactant, is placed in front of MoO_3. Initially, the quartz plate is placed in such a way that the sulphur powder is outside of the heating zone as shown in Figure 4.1 a). Nitrogen is used as a carrier gas throughout the process. When the temperature reaches the growth temperature, the furnace of CVD is pulled to the left so that the sulphur part is also included in the heating zone for 5 min. At the end of this duration, the quartz tube is cooled down to room temperature. The process is performed under ambient pressure. As a result of the final process, MoS_2 is grown in the presence of Mo_2C MXene flakes, and MoS_2/Mo_2C structures are obtained on SiO_2/Si as shown in Figure 4.1 b). Thus, MXene, a metallic material, and MoS_2, a semiconductor material, are combined in this way for the first time in CVD.

According to the optical microscopy images, the surface of the obtained hybrid structure is wrinkly and non-uniform. MoS_2 is suggested to grow on the flake of Mo_2C MXene by dispersing the initial MXene structure partially. Different color transitions are observed on the rough surface where the edges of the structure are rather dark indicating a thinner layer growth. The brighter parts point out to thicker layer growth. To simplify the analysis, three different regions are determined, namely the center, edge and middle regions as indicated in Figure 4.1 c) and Figure 4.1 d) of which the images are taken from the optical microscope as bright and dark fields, respectively.

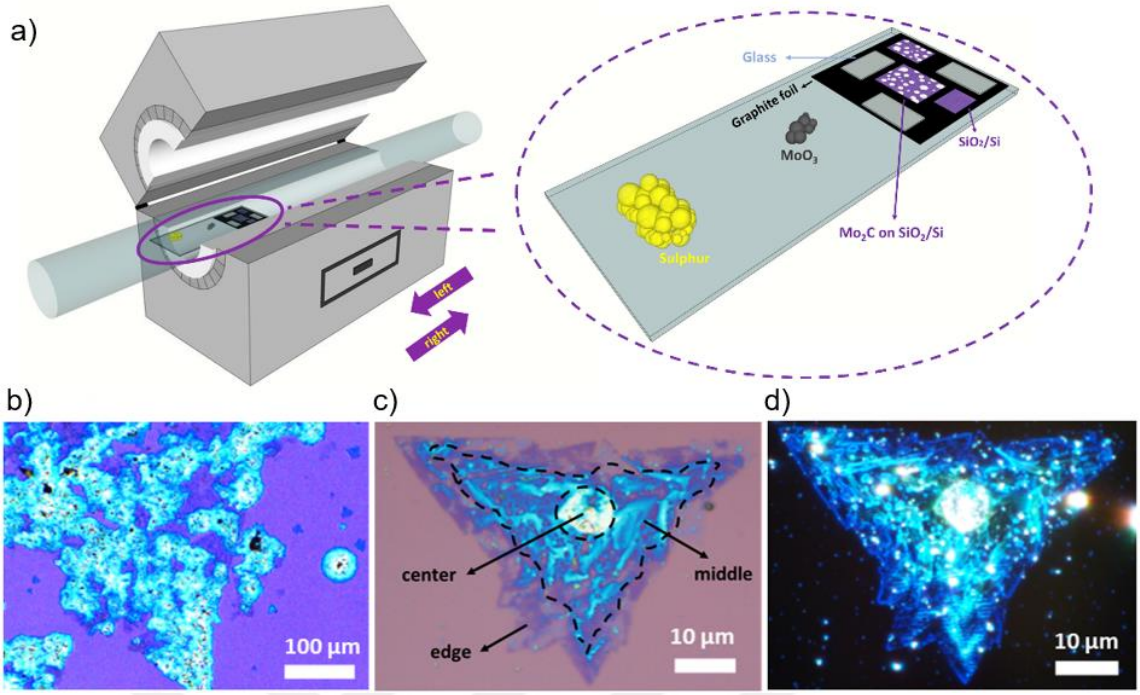

Figure 4.1. *Schematic of the CVD system designed for the growth of MoS_2/Mo_2C structures. Inset: The top view of the precursors and substrates on the quartz plate. b) Optical microscopy image of MoS_2/Mo_2C structure on SiO_2/Si. The purple color: SiO_2/Si substrate c) Bright field and d) dark field optical microscopy images of MoS_2/Mo_2C flake on SiO_2/Si*

4.2. Raman Measurements

Raman spectra of the flake have been taken from the three specified regions shown in Figure 4.2 a). These Raman spectra verify the growth of MoS_2 and Mo_2C structures for the specified regions. The spectra have been de-convoluted by using Lorentzian fit to indicate individual Raman modes. E_{2g} and A_{1g} modes of MoS_2 are easily observed in the spectrum, whereas Mo_2C modes are quite difficult to observe due to the very low signal-to-noise ratio. The zoom-in spectra from 40 cm^{-1} to 240 cm^{-1} display three fitted modes of Mo_2C.

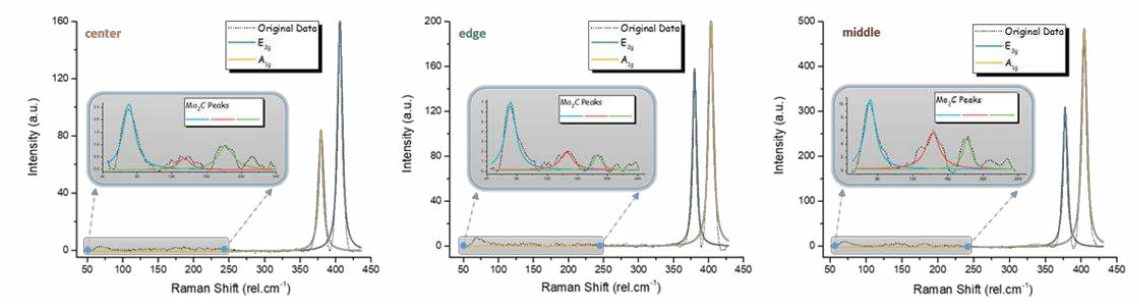

Figure 4.2. *Raman spectra of MoS_2/Mo_2C flake on Si/SiO_2 for three specified regions. Inset: The zoom-in spectra from 40 cm^{-1} to 240 cm^{-1}*

Raman intensity maps have been created in the same CCD range, to clarify the surface distribution, are shown in Figure 4.3. The maps, created according to the Mo_2C modes, show that MXene Raman intensities are almost quenching in the flake. In addition, the highest intensities (A_{1g} and E_{2g} modes respectively) are seen on created maps for MoS_2. In addition, the maps display that MoS_2 and Mo_2C are present irregularly throughout the flake, appearing in different site.

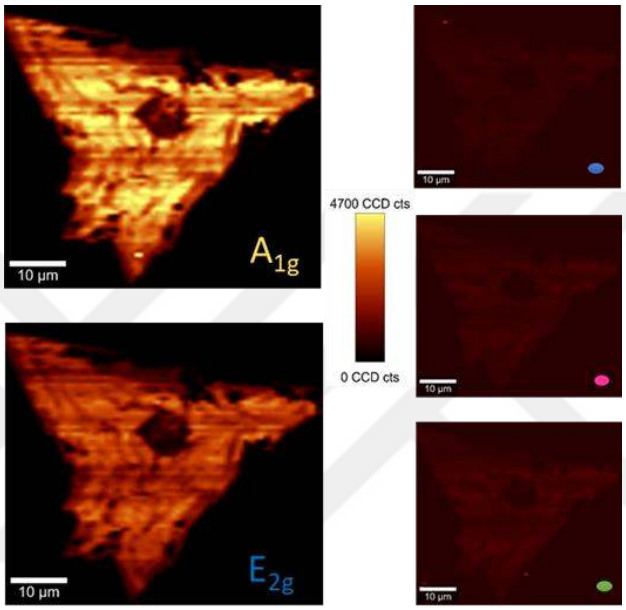

Figure 4.3. *Raman Intensity-Integrated Maps of examined flake for each Raman vibration mode; A_{1g} and E_{2g} for MoS_2 modes, blue-pink-green ellipse for Mo_2C modes. Inset: 0-4700 CCD cts range for all map.*

In Figure 4.4, three different points have been marked on the flake and the Raman spectra of MoS_2 modes taken from these points are shown. The highest MoS_2 Raman intensities are measured in the middle region, where the metallic and semiconductor materials are considered to be most mixed. Also, it is observed that the center region has the lowest intensity, which could be explained by the existence of MXenes in that site. In addition, the positions of the given peaks or the frequency differences give information about the stacking of MoS_2 in the flake. The formation of multilayer MoS_2 is indicated by the positions marked with lilac dashed lines in the Figure 4.4 b). Accordingly, at the edge, the formation of MoS_2 is either a monolayer or a few layers. Also, it can be deduced that the stacking of MoS_2 in the middle region is multilayered.

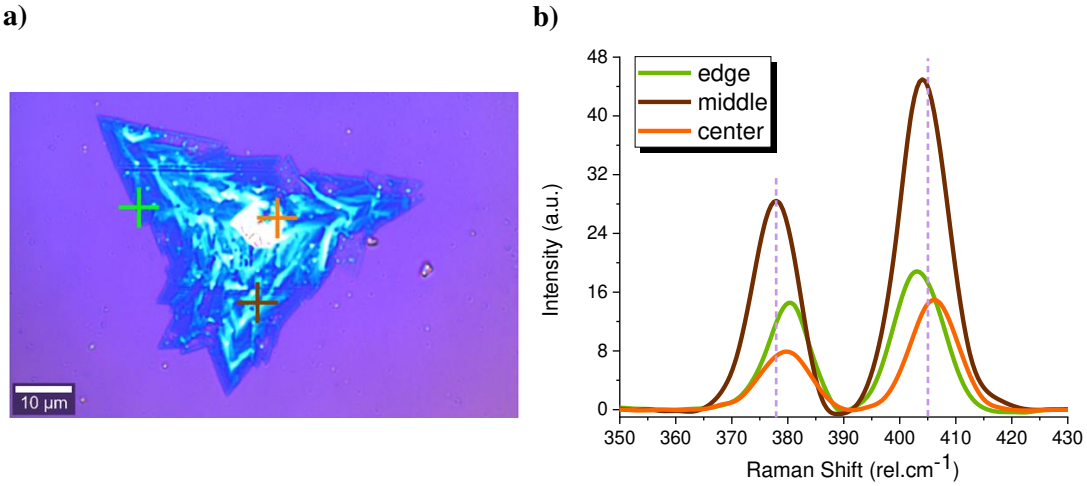

Figure 4.4. *a) Optical microscopy image of the flake with colored marks; and b) Raman spectra of MoS_2 modes corresponding to these marked regions.*

4.3. AFM Measurements

AFM height profile of the flake along the green line in Figure 4.5 a) is shown in Figure 4.5 c). Because of the non-uniform surface structure, the height profile is like oscillating and looks zigzag. The height of the edge region of the flake is ~8 nm and the middle region is ~12 nm. The edge and middle regions are close to each other, while the height of the center region is far from them, it is ~34 nm. So, from the edge to the center, the height of the structure increase. This increase is also observed clearly from the 3D topography in Figure 4.5 b).

AFM measurements are correlated with Raman spectra. Raman spectra have been normalized to observe the relationship with the height profile. Raman spectra of the specified regions of the MoS_2/Mo_2C flake on SiO_2/Si and bare monolayer MoS_2 on SiO_2/Si spectra are shown in Figure 4.5 e). Bare monolayer MoS_2 has been added for a better comparison. A shift in the E_{2g} and A_{1g} Raman vibration modes are observed. When the thickness of an atomic layer MoS_2 is compared to the thickness of MoS_2/Mo_2C flake on SiO_2/Si, an upshift of A_{1g} mode and a downshift of E_{2g} mode are observed. The frequency difference between the E_{2g} and A_{1g} modes increases from bare monolayer MoS_2 to the center of MoS_2/Mo_2C flake on SiO_2/Si. In the same way, from bare monolayer MoS_2 to the center of MoS_2/Mo_2C flake on SiO_2/Si, the thickness increases according to AFM measurements. Raman position map of A_{1g} mode is also shown in Figure 4.5 d) to support this inference. A_{1g} mode upshifts from 403 cm^{-1} to 407 cm^{-1} with increasing thicknesses.

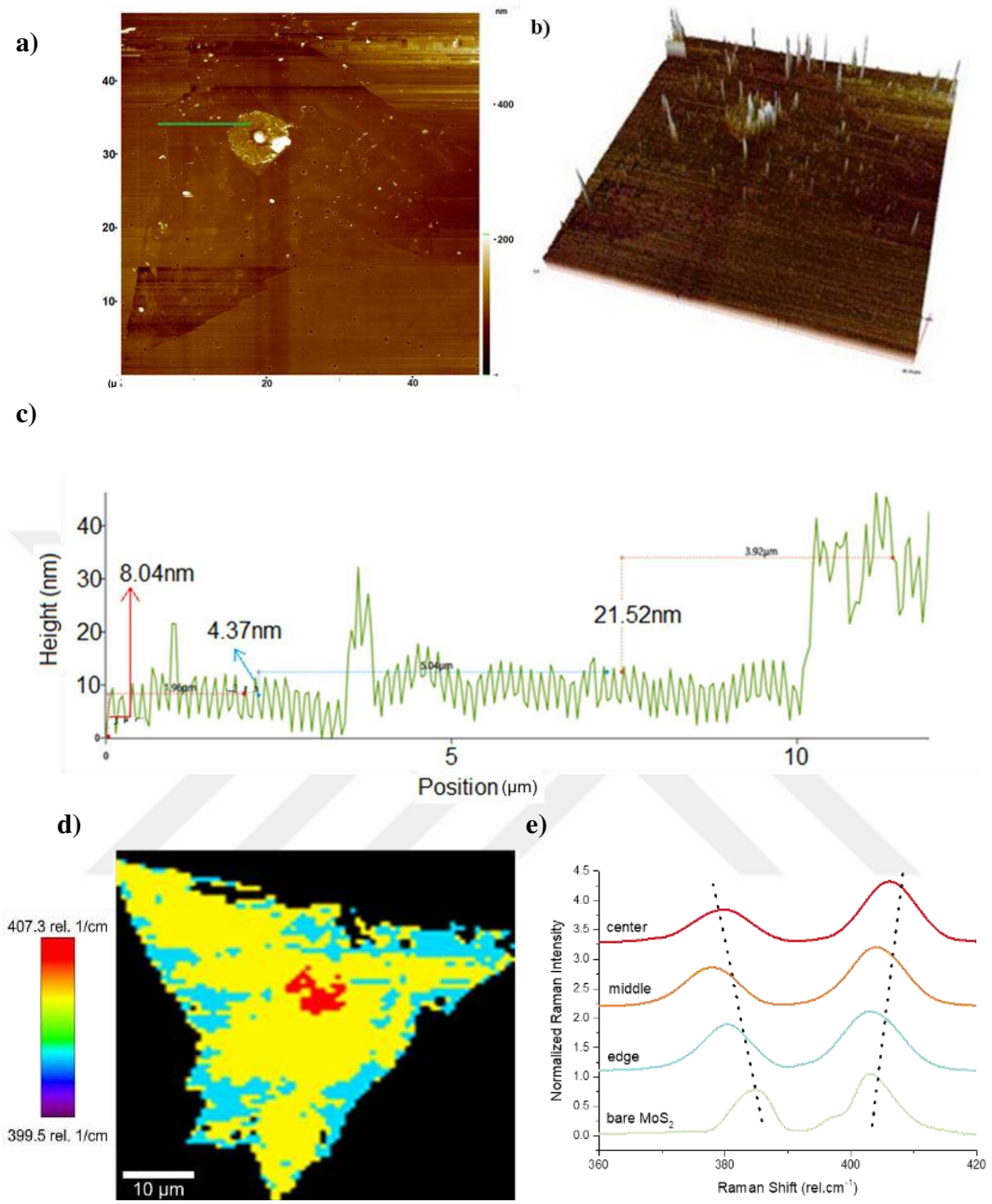

Figure 4.5. *a) Topography of the flake on SiO_2/Si. b) 3D Topography of the flake on SiO_2/Si. c) The height profile along the green line in a). d) Raman mode position map of A_{1g}. Scale bar: 10 µm. e) Raman spectra of MoS_2/Mo_2C flake on SiO_2/Si for specified regions in comparison with the bare monolayer MoS_2. The left and right columns of dashed lines; the positions of the E_{2g} and A_{1g}, respectively*

4.4. Photoluminescence Measurements

Photoluminescence intensities of three specified regions are shown in Figure 4.6 a). Photoluminescence intensity of MoS_2/Mo_2C flake on SiO_2/Si has non-uniform distribution, as in Raman spectra too. There is almost no photoluminescence in the center because of the metallic MXenes' existence. However, photoluminescence enhancement

is observed from the middle to the edge. This enhancement is also correlated to the thickness of the flake. Photoluminescence intensity increases, as the thickness decreases. The photoluminescence map is also shown in Figure 4.6 b) to support this inference.

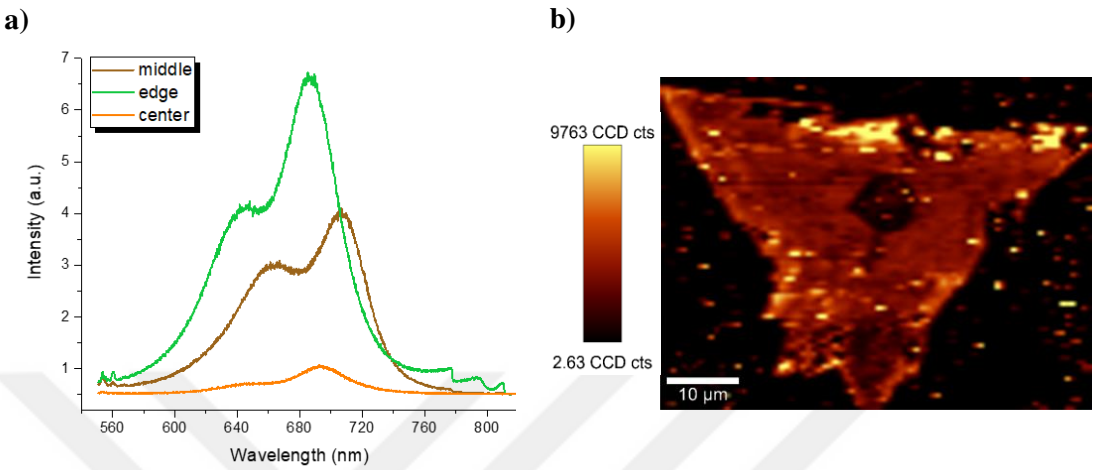

Figure 4.6. *a) Photoluminescence spectra of MoS_2/Mo_2C flake on SiO_2/Si for three specified regions b) Photoluminescence intensity map of MoS_2/Mo_2C flake on SiO_2/Si. Scale bar: 10 µm*

Moreover, to observe the effect of the combination of metallic and semiconductor properties on exciton transitions, photoluminescence spectra have been de-convoluted by using Gaussian fit. Bare monolayer MoS_2 spectra have been added to show differences from MoS_2/Mo_2C flake. The obtaining transitions are shown in Figure 4.7. Whereas the dominant exciton transition of monolayer MoS_2 is A, other transitions in MoS_2/Mo_2C flake are at least as active as A. A and B excitons are formed by the splitting in the valance band (Dhakal, 2014). The spin-orbit coupling and some interlayer coupling usually bring this splitting. MoS_2/Mo_2C flake hasn't got an atomic thickness, so its interlayer interactions can produce a local electric field at the interface. In addition, charge redistribution may occur between the materials that comprise the structure, through quantum tunneling or Coulomb interactions, causing structural changes in each other. Presumably, these have brought with the different characteristic transitions of excitons.

A trion is a lower energy resonance of the A exciton. The existence of A trion correlates to a reduction of photoluminescence (Kin Fai Mak, 2013). Moreover, nonradiative recombination is dominant in A trion transitions (Kang, 2021). Trions appear accompanied by a photoluminescence quenching. The enhancement of the A trion in the center is shown in Figure 4.7 a). In addition, photoluminescence almost quenches in the center of the MoS_2/Mo_2C flake as mentioned above. This quenching has been

observed, probably because nonradiative recombination occurs in the center of the MoS_2/Mo_2C flake. The photoluminescence intensity maps which are based on the spectra taken from the center are shown in Figure 4.7 b). The dominance of the A trion according to other transitions is also supported with the photoluminescence intensity map of the A trion.

a)

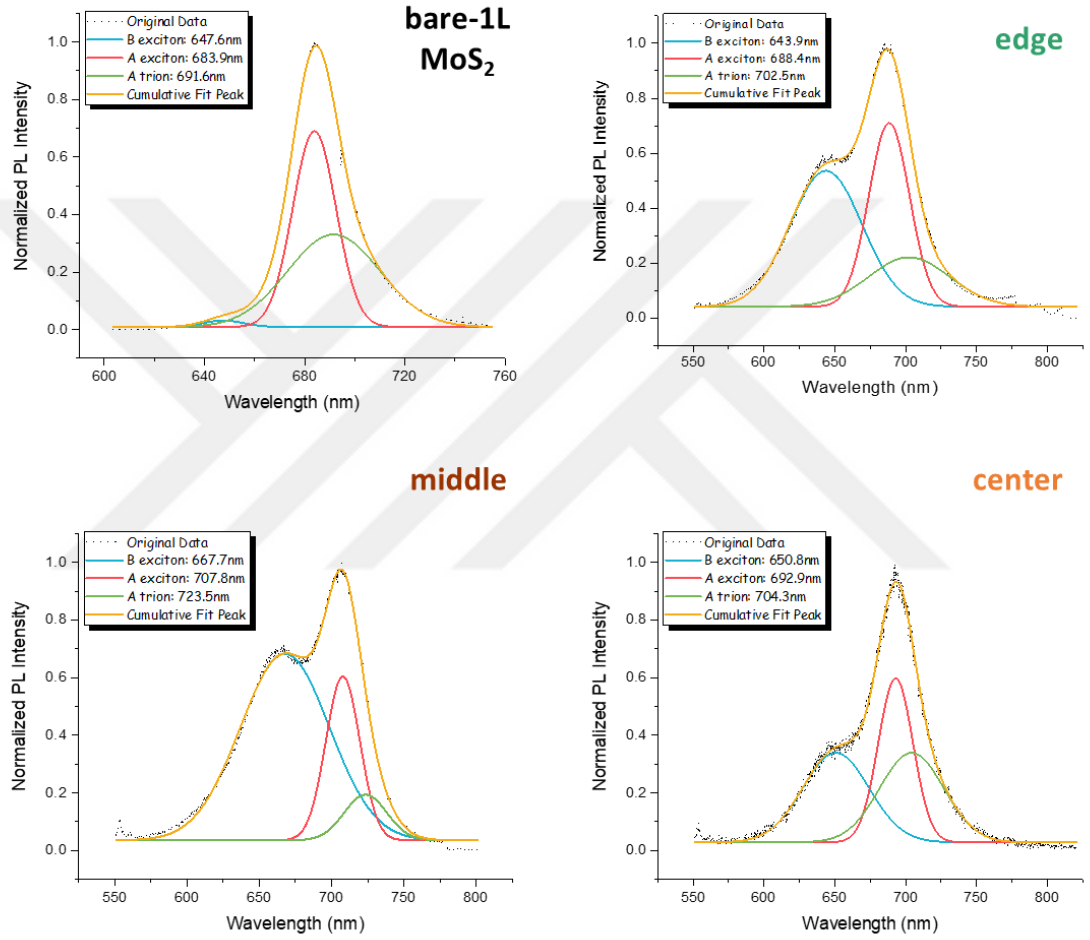

b)

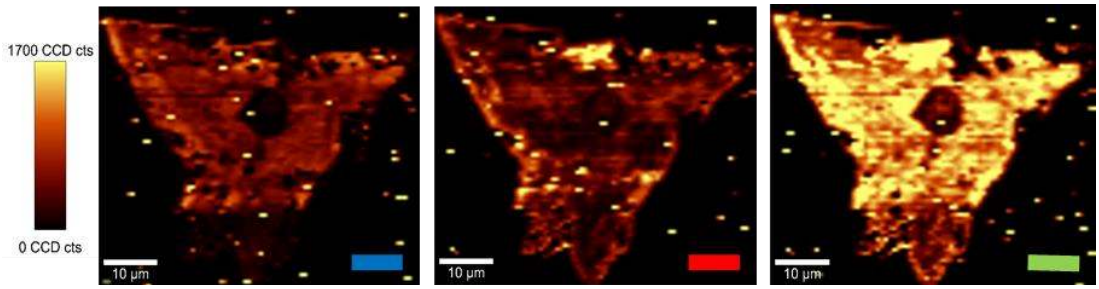

Figure 4.7. *a) Photoluminescence spectra of bare 1L (monolayer) MoS_2 on SiO_2/Si and photoluminescence spectra of MoS_2/Mo_2C flake on SiO_2/Si for three specified regions. Inset: Excitons and trion positions, obtained by Gaussian fit in nm. b) Photoluminescence Intensity-Integrated Maps of the structure for the transitions of the center; blue mark for B exciton, red mark for A exciton, green mark for A trion. Inset: 0-1700 CCD cts range for all maps. Scale bars: 10 µm*

4.5. Fluorescence Lifetime Measurements

Fluorescence lifetime is defined as the average time a fluorophore remains in the excited state (Gartia, 2012). MoS_2/Mo_2C flake on SiO_2/Si has been excited with a laser power of 0.25 mW at 12.5 ns excitation pulse sequence. It has absorbed a laser energy of 485 nm for the excitation. After excitation, the emission intensities of MoS_2/Mo_2C flake have decayed exponentially with different rates. Emission data and exponential decay curves are shown in Figure 4.8. The average time of MoS_2/Mo_2C flake from the excited state to the electronic ground state has been 0.42 ns in the edge region, whereas 0.37 ns in the middle region. If the middle region is considered as the region where metallic Mo_2C and semiconductor MoS_2 are most mixed, it is possible to attribute the shortened lifetime to additional pathways of de-excitation that provides by metal. A metal nanostructure increases the nearby electric field and creates a surface plasmon resonance thus fluorescence enhancement is observed (Shy-Hauh Guo, 2008). Fluorescence is one of the de-excitation pathways that increase the rate at which photons leave the excited state (Gartia, 2012). Photons of MoS_2/Mo_2C flake in the middle region leave faster from the excited state than photons in the edge region, probably due to the intense metallic MXene existence in the middle region. In other words, the edge region has a longer lifetime than the middle region.

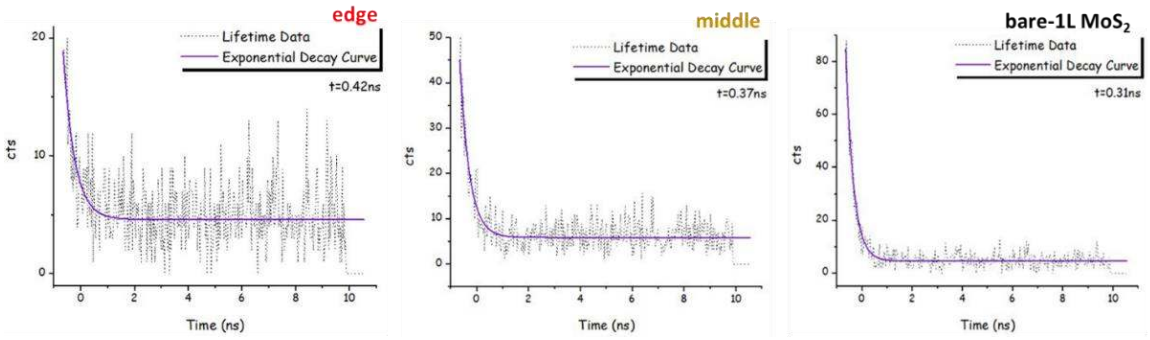

Figure 4.8. *Lifetime data and exponential decay curves of MoS_2/Mo_2C flake on SiO_2/Si in the edge and middle; and lifetime data and exponential decay curves of bare 1L MoS_2 on SiO_2/Si*

In addition, the lifetime of the bare monolayer MoS_2 has been 0.31 ns with the same conditions. This result shows that MoS_2/Mo_2C flake on SiO_2/Si has a longer lifetime than bare monolayer MoS_2 on SiO_2/Si. The FLIM of the MoS_2/Mo_2C flake has been created in the 0.2 ns - 0.45 ns lifetime range and is shown in Figure 4.9. This map shows that fluorescence lifetime measurement result could not be obtained from the center region, and the results at the measurement regions also show diversity. Moreover, the FLIM of bare monolayer MoS_2, from the study had been carried out before in our laboratory, was observed in the 0.2 ns - 0.45 ns range too (Ayberk Özden, 2016). In the results there, the FLIM of MoS_2 was obtained as a homogeneous image with a value of 0.3 ns. The longer lifetime of the MoS_2/Mo_2C flake is also supported by the same range of FLIMs generated in both the previous study and this study.

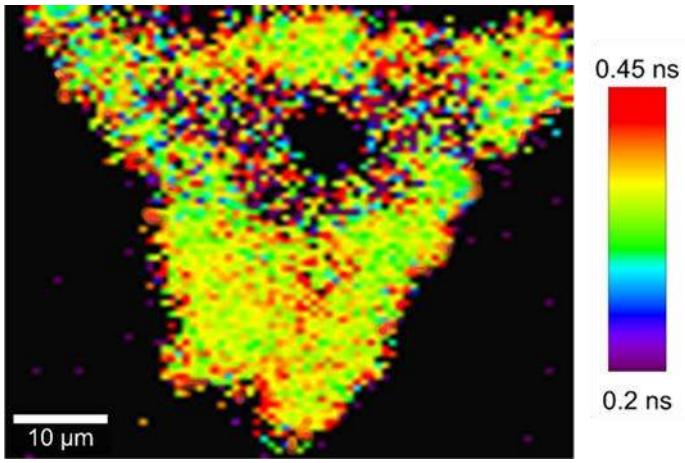

Figure 4.9. *Fluorescence Lifetime Image Mapping of MoS_2/Mo_2C flake on SiO_2/Si. Inset: 0.2 – 0.45 ns range*

5. CONCLUSIONS AND FUTURE ASPECTS

This thesis presented significant contributions to the field of nanoscience. Following the initial experimental investigations of 2D materials, subsequent chapters studied specific aspects. Chapter 3 presented conductivity measurement of nano-doped carbon fiber for composite materials for avionic applications. Chapter 4 presented the characterization of a novel 2D structure resulting from the combination of semiconductor and metallic properties, in relation to optical transitions for optoelectronic applications. The following paragraphs provide summaries of the chapters with the recommended future studies.

In the second chapter (2) of this thesis, deposition experiments were carried out for graphene, Mo_2C, and MoS_2 via the CVD, and their characterization studies were performed. Raman spectroscopy was used to determine the deposition of monolayer and multilayer graphene. However, a study on the exact number of layers for multilayer graphene has not yet been conducted. Layer determination studies in the literature are mostly related to exfoliated graphene production. At present, studies on determining the number of layers of graphene deposited via CVD are insufficient. Future studies can be conducted in this regard. In addition, deposition of large area graphene is also important, as it enables seamless integration into various surfaces, expanding its potential applications across different fields. The maximum size achieved for graphene layer was 1.7 cm x 7 cm. Future studies can be focus the size of graphene layer too.

The MXene was subjected to deposition experiments, wherein the copper thickness, temperature, methane flow rate, and growth time parameters were varied. The aim of the experiments was to achieve full coverage of MXene flakes over molybdenum/copper foil. At first, it was observed that the coverage increased with thin copper. Subsequently, it was observed that coverage increased with an increase in temperature, but only up to 1200 °C, after which coverage suddenly decreased. An increase in methane flow rate supported the increase in coverage, although it was not as effective as the other factors. An increase in growth time also supported the increase in coverage. In MXene characterization, studies were conducted to determine whether the positions and intensities of detected peaks provide information about the resulting flake. No clear correlation was observed between the peak data and either the thickness or the growth temperature of Mo_2C flakes. Further investigations are necessary to achieve a comprehensive understanding of the Raman data detected in Mo_2C flakes. In addition, it

was concluded that there is no clear relationship between the thickness of the flakes and either the growth temperature or the methane flow rate. Regardless of the experimental parameters, the thicknesses of the resulting flakes varied even within a single experiment. Future studies can focus on achieving a homogeneous thickness for the flakes. Finally, it was concluded that Mo_2C could be deposited without graphene. Raman data showed that no graphene modes were detected in Mo_2C flakes deposited with 0.7 sccm, which is important in achieving the desired characteristics for Mo_2C.

Monolayer MoS_2 was successfully obtained on both SiO_2/Si and glass, and its monolayer structure was confirmed via Raman spectroscope and AFM. Additionally, optical microscopy images of MoS_2 on the substrates are presented.

In the second chapter (2.2), information and results regarding the transfer processes of the deposited 2D materials onto SiO_2/Si, polycarbonate, and fibers are also provided. While the transfer of graphene and MoS_2 was successfully completed, it was shown that full coverage Mo_2C could not be transferred to the desired substrate. This problem was found to be caused by the chemicals used during the transfer process. In future studies, new transfers can be attempted by exploring more chemicals and learning from more literature examples.

The third chapter (3) focuses on conductivity measurements of the carbon fibers. At first, a silver paste was determined as the best contact material among the others. Subsequently, improvements were made to achieve stable measurements. It was found that placing the carbon fiber between PET strips gave low variations in the results. Furthermore, multilayer graphene transfer was carried out to increase the conductivity of carbon fiber. It was observed that the conductivity of the first supplied carbon fiber increased after graphene transfer, but no increase was observed when a more conductive carbon fiber was used. Nevertheless, the increase in conductivity observed in the first supplied carbon fiber is promising. For future studies, carbon fibers with known conductivity values or values that can at least lead us to conductivity, such as thickness, should be supplied. Then, efforts should be made to capture these values accurately. After confirmation of the accuracy, 2D material transfers can be made onto carbon fibers, and conductivity measurements can be investigated.

The fourth chapter (4) of this thesis presents a novel 2D structure, which introduced for the first time. This unique structure was obtained through the direct growth of a semiconductor, MoS_2, on metallic Mo_2C using the CVD. The structure was analyzed

in three different regions based on surface images captured with an optical microscope. Correlations between AFM and Raman/Photoluminescence measurements were observed, where the frequency difference between the E_{2g} and A_{1g} Raman vibration modes increased as the thickness of the new structure increased, and the photoluminescence intensity decreased with increasing thickness. Additionally, the Mo_2C affected the photon excitation and electronic dynamics of MoS_2, resulting in different optical transitions compared to the bare monolayer MoS_2. These transitions also varied for each region of the new structure due to its non-uniformity. Although lifetime results varied for each region, it was concluded that the new structure had a longer lifetime than the bare monolayer MoS_2. Future works can involve its characterization using various tools to better understand the properties of the newly produced structure.

REFERENCES

A. Castro Neto, F. G. (2009). The electronic properties of graphene. *Reviews of Modern Physics, 81*, 109-162. doi:10.1103/RevModPhys.81.109

A. Lipatov, H. L. (2018). Elastic properties of 2D Ti3C2Tx MXene monolayers and bilayers. *Science Advances, 4*(6). doi:10.1126/sciadv.aat0491

A. S. Zeraati, S. A. (2021). Improved synthesis of Ti3C2Tx MXenes resulting in exceptional electrical conductivity, high synthesis yield, and enhanced capacitance. *Nanoscale, 13*(6), 3572. doi:10.1039/d0nr07781g

A.N. Enyashin, A. I. (2013). Two-dimensional titanium carbonitrides and their hydroxylated derivatives: Structural, electronic properties and stability of MXenes Ti3C2−xNx(OH)2 from DFTB calculations. *Journal of Solid State Chemistry, 207*, 42-48. doi:10.1016/j.jssc.2013.09.010

Abdelmalak, N. (2014). MXenes: A New Family of Two-Dimensional Materials and Its Application as Electrodes for Li-Ion Batteries. *Thesis for the degree of PhD*. Philadelphia, USA: Drexel University.

Alexandar D. Marinov, L. B. (2023). Characterization of 1T/2H MoS2 and Their Carbon Composites for Energy Applications. *ACS Nano, 17*, 5163-5186. doi:10.1021/acsnano.2c08913

Ayberk Özden, H. Ş. (2016). CVD grown 2D MoS2layers: A photoluminescence and fluorescence lifetime imaging study. *physica status solidi (RRL) - Rapid Research Letters, 10*(11), 792-796. doi:10.1002/pssr.201600204

Babak Anasori, C. S. (2016). Control of electronic properties of 2D carbides (MXenes) by manipulating their transition metal layers. *Nanoscale Horizons, 1*, 227-234. doi:10.1039/C5NH00125K

C. Berger, Z. S.-H. (2006). Electronic confinement and coherence in patterned epitaxial graphene. *Science, 312*(5777), 1191-1197. doi:10.1126/science.1125925

Choi S., P. J. (2019). Scalable Two-Dimensional Lateral Metal/Semiconductor Junction Fabricated with Selective Synthetic Integration of Transition-Metal-Carbide (Mo(2)C)/-Dichalcogenide (MoS(2)). *ACS Appl Mater Interfaces, 11*(50), 47190-47196. doi:10.1021/acsami.9b14589

Chuan Xu, L. W.-L.-M. (2015). Large-area high-quality 2D ultrathin Mo2C superconducting crystals. *Nature Materials, 14*, 1135–1141. doi:10.1038/nmat4374

Chuan Xu, S. S.-M. (2017). Strongly Coupled High-Quality Graphene/2D Superconducting Mo2C Vertical Heterostructures with Aligned Orientation. *ACS Nano, 11*(6), 5906-5914. doi:10.1021/acsnano.7b01638

D. Geng, X. Z. (2016). Controlled growth of ultrathin Mo2C superconducting crystals on liquid Cu surface. *2D Materials, 4*(1). doi:10.1088/2053-1583/aa51b7

Dechao Geng, X. Z. (2016). Controlled growth of ultrathin Mo2C superconducting crystals on liquid Cu surface. *2D Materials, 4*. doi:10.1088/2053-1583/aa51b7

Dechao Geng, X. Z. (2016). Controlled growth of ultrathin Mo2C superconducting crystals on liquid Cu surface. *2D Materials, 4*(1). doi:10.1088/2053-1583/aa51b7

Dechao Geng, X. Z. (2017). Direct Synthesis of Large-Area 2D Mo2 C on In Situ Grown Graphene. *Advanced Materials, 29*(35). doi:10.1002/adma.201700072

Dhakal, K. M. (2014). Confocal absorption spectral imaging of MoS2: optical transitions depending on the atomic thickness of intrinsic and chemically doped MoS2. *Nanoscale, 6*(21), 13028-35. doi:10.1039/c4nr03495a

Gartia, M. R. (2012). Lifetime imaging of radiative and non-radiative fluorescence decays on nanoplasmonic surface. *Applied Physics Letters, 101*(2). doi:10.1063/1.4736575

Hüseyin Şar, A. Ö. (2019). Long-Term Stability Control of CVD-Grown Monolayer MoS2. *physica status solidi - Rapid Research Letter*. doi:10.1002/pssr.201800687

Jeon, J. H. (2018). Epitaxial Synthesis of Molybdenum Carbide and Formation of a Mo(2)C/MoS(2) Hybrid Structure via Chemical Conversion of Molybdenum Disulfide. *ACS Nano, 12*(1), 338-346. doi:10.1021/acsnano.7b06285

K. Bolotin, K. S. (2008). Ultrahigh electron mobility in suspended graphene. *Solid State Communications, 146*, 351-355. doi:10.1016/j.ssc.2008.02.024

K. S. Novoselov, V. I. (2012). A roadmap for graphene. *Nature, 490*(7419), 192-200. doi:10.1038/nature11458

K.S. Novoselov, A. M. (2016). 2D materials and van der Waals heterostructures. *Science, 353*(6298), 461. doi:10.1126/science.aac9439

K.S. Novoselov, K. G. (2004). Electric field effect in atomically thin carbon films. *Science, 306*(5696), 666-675. doi:10.1126/science.1102896

K.S. Novoselov, K. G. (2005). Two dimensional gas of massless Dirac fermions in graphene. *Nature, 438*, 197-200. doi:10.1038/nature04233

Kamysbayev V, F. A. (2020). Covalent surface modifications and superconductivity of two-dimensional metal carbide MXenes. *Science, 369*(6506), 979-983. doi:10.1126/science.aba8311

Kang, S. K. (2021). Enhanced Photoluminescence of Multiple Two-Dimensional van der Waals Heterostructures Fabricated by Layer-by-Layer Oxidation of MoS(2). *ACS Applied Materials Interfaces, 13*(1), 1245-1252. doi:10.1021/acsami.0c16880

Khazaei M, A. M. (2013). Novel Electronic and Magnetic Properties of Two-Dimensional Transition Metal Carbides and Nitrides. *Advanced Functional Materials, 23*(17), 2185–2192. doi:10.1002/adfm.201202502

Kılıç, N. B. (2022). Tailoring CVD MXene Layers for Applications in Aviation. *Thesis for the degree of Master*. Eskisehir Technical University, Electrical Electronics Engineering.

Kim, K. S. (2009). Large-scale pattern growth of graphene films for stretchable transparent electrodes. *Nature, 457*(7230), 706-710. doi:10.1038/nature07719

Kin Fai Mak, K. H. (2013). Tightly bound trions in monolayer MoS2. *Nature Materials, 12*(3), 207-211. doi:10.1038/NMAT3505

L. Huang, Q. C. (2012). Synthesis of high-quality graphene films on nickel foils by rapid thermal chemical vapor deposition. *Carbon, 50*(2), 551-556. doi:10.1016/j.carbon.2011.09.012

Lancelot, E. (2011). *Perspectives on Raman Spectroscopy of Graphene.* Jobin Yvon, France: Horiba Scientific. Retrieved from Horiba Scientific.

M. Khazaei, M. A. (2014). Trends in electronic structures and structural properties of MAX phases: a first-principles study on M2AlC (M = Sc, Ti, Cr, Zr, Nb, Mo, Hf, or Ta), M2AlN, and hypothetical M2AlB phases. *Journal of Physics: Condensed Matter, 26*(50), 505503. doi: 10.1088/0953-8984/26/50/505503

M. Naguib, M. K. (2011). Two-Dimensional Nanocrystals Produced by Exfoliation of Ti3AlC2. *Advanced Materials, 23*(37), 4248–4253. doi:10.1002/adma.201102306

M.S. Purewal, Y. Z. (2006). Unusual transport properties in carbon based nanoscaled materials: nanotubes and graphene. *Physica Status Solidi (B), 243*(13), 3418-3422. doi:10.1002/pssb.200669193

Manish Chhowalla, H. S.-J. (2013). The chemistry of two-dimensional layered transition metal dichalcogenide nanosheets. *Nature Chemistry, 5*, 263-275. doi:10.1038/NCHEM.1589

Maria R Lukatskaya, O. M. (2013). Cation intercalation and high volumetric capacitance of two-dimensional titanium carbide. *Science, 341*(6153), 1502-1505. doi:10.1126/science.1241488

Mckenzie, A. B. (2015). Characterization of Electrical Conductivity of Carbon Fiber/Epoxy Composites with Conductive AFM and Scanning Microwave Impedance Microscopy. *Thesis for the degree of Master*. University of Illinois at Urbana-Champaign, Science in Aerospace Engineering.

Merve Öper, U. Y. (2022). Controlled CVD growth of ultrathin Mo2C (MXene) flakes . *Journal of Applied Physics, 131*(2). doi:10.1063/5.0067970

Mukesh Singh, H. S. (2014). Growth of large sp2 domain size single and multi-layer graphene films at low substrate temperature using hot filament chemical vapor deposition. *Materials Letters*, 249-252. doi:10.1016/j.matlet.2014.04.066

Naguib M., M. V. (2014). MXenes: a new family of two-dimensional materials. *Advanced Materials, 26*(7), 992-1005. doi:10.1002/adma.201304138

Olutayo I. Olubiyi, F.-K. L. (2015). Chapter 17 - Advances in Molecular Imaging for Surgery. In *Image-Guided Neurosurgery* (pp. 407-439). Academic Press. doi:10.1016/B978-0-12-800870-6.00017-0

Pin-Chun Shen, Y. L.-H.-Y. (2018). CVD Technology for 2D Materials. *IEEE Transactions on Electron Devices, 65*(10), 4040-4052. doi:10.1109/ted.2018.2861002

Sanjay J. Dhoble, A. N. (2023). *Functional Materials from Carbon, Inorganic, and Organic Sources.* Woodhead Publishing Series in Electronic and Optical Materials. doi:10.1016/C2020-0-02903-8

Satyajeet Chaudhari, T. S. (2013). A Review on Polymer Tio2 Nanocomposites. *Journal of Engineering Research and Application, 3*(5), 1386-1391.

Shy-Hauh Guo, J. J.-C. (2008). Enhanced fluorescence and near-field intensity for Ag nanowire/nanocolumn arrays: evidence for the role of surface plasmon standing waves. *Optics Express, 16*(22), 18417-18425 . doi:10.1364/OE.16.018417

Sten Haastrup, M. S.-J. (2018). The Computational 2D Materials Database: high-throughput modeling and discovery of atomically thin crystals. *2D materials, 5*(4). doi:10.1088/2053-1583/aacfc1

Technologies. (2020). Retrieved from HORIBA Scientific: https://www.horiba.com/int/scientific/technologies/raman-imaging-and-spectroscopy/raman-spectroscopy/

Tianshu Li, W. L. (2019). Probing the Domain Architecture in 2D α-Mo2C via Polarized Raman Spectroscopy. *Advanced Materials*. doi: 10.1002/adma.201807160

W. Fang, A. L. (2015). A review of large-area bilayer graphene synthesis by chemical vapor deposition. *Nanoscale, 7*(48), 20335-20351. doi:10.1039/C5NR04756K

W. Lisheshar Ibrahim, H. Ş. (2022). Enhanced performance of supercapacitors based on rotationally stacked CVD graphene. *Journal of Applied Physics, 131*(16). doi:10.1063/5.0084969

Wonge Lisheshar Ibrahim, M. Ö. (2022). Evolution of Raman and photoluminescence spectral characteristics of monolayer CVD-MoS2 over a wide temperature range. doi:10.1016/j.vibspec.2022.103443

Wypych, F., & Schöllhorn, R. (1992). 1T-MoS2, a new metallic modification of molybdenum disulfide. *Journal of the Chemical Society, Chemical Communications*. doi:10.1039/C39920001386

X. Li, W. C. (2009). Large-area synthesis of high-quality and uniform graphene films on copper foils. *Science, 324*(5932), 1312-1314. doi:10.1126/science.1171245

Xianhu Zha, X. S. (2016). Intrinsic Structural, Electrical, Thermal, and Mechanical Properties of the Promising Conductor Mo2C MXene. *The Journal of Physical Chemistry C, 120*(28), 15082-15088. doi:10.1021/acs.jpcc.6b04222

Yu Q, J. L. (2011). Control and characterization of individual grains and grain boundaries in graphene grown by chemical vapour deposition. *Nat Mater*. doi:10.1038/nmat3010

Zhe Kang, Z. Z. (2019). Controlled Growth of an Mo2C—Graphene Hybrid Film as an Electrode in Self-Powered Two-Sided Mo2C—Graphene/Sb2S0.42Se2.58/TiO2 Photodetectors. *Sensors, 19*(5), 1099. doi:10.3390/s19051099

Zhiqiang Tu, Z. (2014). Controllable growth of 1–7 layers of graphene by chemical vapour deposition. *Carbon*, 252-258. doi:10.1016/j.carbon.2013.09.002

CURRICULUM VITAE

ORCID ID: 0000-0001-6806-763X

Name Surname : Elif Sevgi SİCİM

Education and Professional Background:

- 2020-current, Eskisehir Technical University, Electronic, Master's degree
- 2015-2020, Eskisehir Osmangazi University, Electrical Electronics Engineering, Bachelor's degree

Publications and/or Scientific/Artistic Activities:

- Sicim S. E., 2022, 16th Nanoscience and Nanotechnology Conference, Oral Presentation, Middle East Technical University, Ankara.
- Sicim S. E., Kök D., Güdük I., Gengeç P., and Edizkan R., 2020, "Development of Intelligent Companion Robot" In 2020 Innovations in Intelligent Systems and Applications Conference (ASYU).
- Sicim, E.S., Aydın, O., Ay, F. and Kosku Perkgöz, N., 2023, "Investigation of CVD Growth of 2D MoS2 on MXene Structures with Photoluminescence Mapping and Fluorescence Lifetime Imaging Microscopy", Phys. Status Solidi B 2300242.